ISSN: 2161-4717 Volume 8, Number 3, September 2018

Scientific Research Publishing

International Journal of Astronomy and Astrophysics

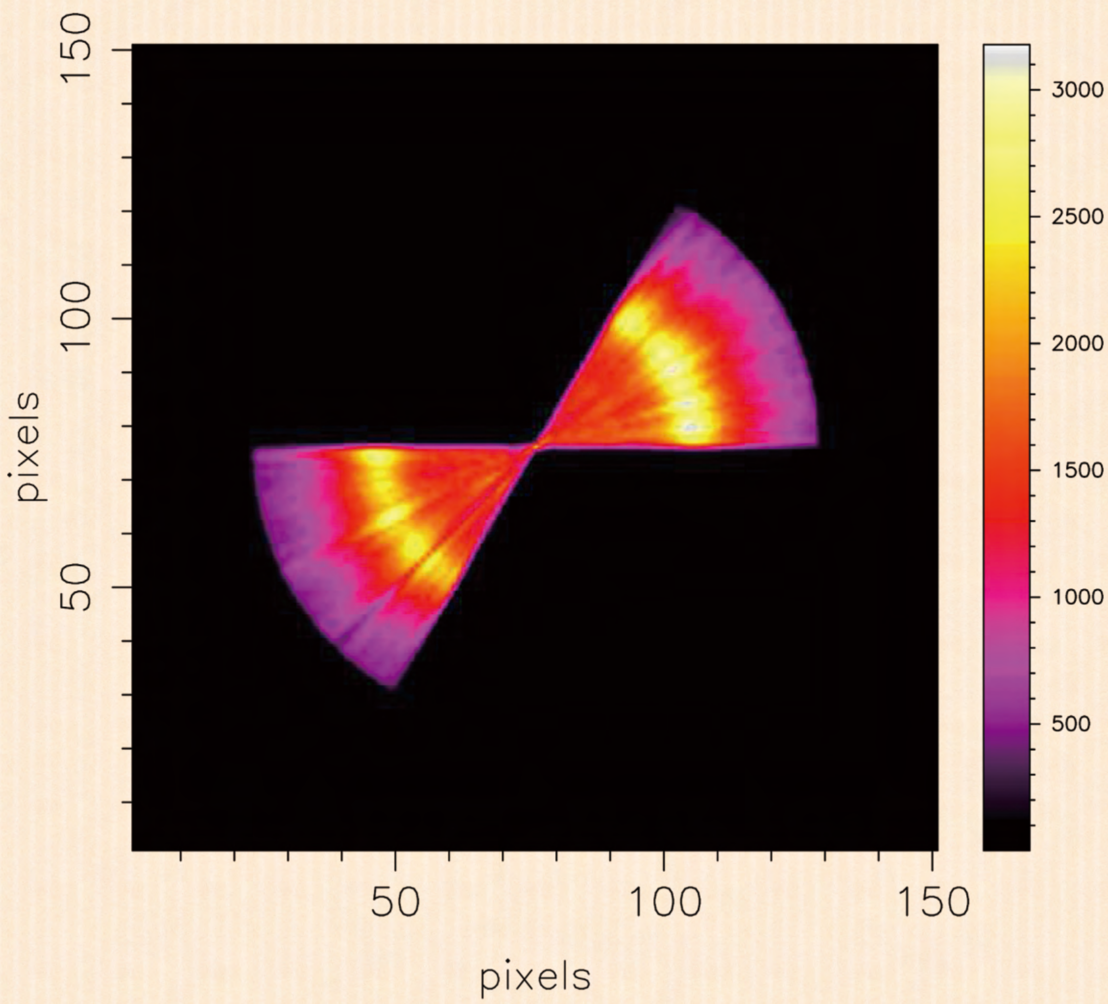

ISSN: 2161-4717
9 772161 471005 03

www.scirp.org/journal/ijaa

Journal Editorial Board

ISSN 2161-4717 (Print) ISSN 2161-4725 (Online)
http://www.scirp.org/journal/ijaa

International Journal of Astronomy and Astrophysics, 2018, 8, 219-298
http://www.scirp.org/journal/ijaa
ISSN Online: 2161-4725
ISSN Print: 2161-4717

Table of Contents

Volume 8 Number 3 September 2018

The figure on the front cover is from the article published in International Journal of Astronomy and Astrophysics, 2018, Vol. 8, No. 3, pp. 258-266 by Lorenzo Zaninetti.

International Journal of Astronomy and Astrophysics (IJAA)
Journal Information

SUBSCRIPTIONS

The *International Journal of Astronomy and Astrophysics* (Online at Scientific Research Publishing, www.SciRP.org) is published quarterly by Scientific Research Publishing, Inc., USA.

Subscription rates:
Print: $79 per issue.
To subscribe, please contact Journals Subscriptions Department, E-mail: sub@scirp.org

SERVICES

Advertisements
Advertisement Sales Department, E-mail: service@scirp.org

Reprints (minimum quantity 100 copies)
Reprints Co-ordinator, Scientific Research Publishing, Inc., USA.
E-mail: sub@scirp.org

COPYRIGHT

PRODUCTION INFORMATION

For manuscripts that have been accepted for publication, please contact:
E-mail: ijaa@scirp.org

International Journal of Astronomy and Astrophysics, 2018, 8, 219-229
http://www.scirp.org/journal/ijaa
ISSN Online: 2161-4725
ISSN Print: 2161-4717

Static and Dynamic Components of the Redshift

Rajendra P. Gupta[1,2]

[1]Macronix Research Corporation, Ottawa, Canada
[2]National Research Council, Ottawa, Canada (Retired)
Email: sonice810@gmail.com

How to cite this paper: Gupta, R.P. (2018) Static and Dynamic Components of the Redshift. *International Journal of Astronomy and Astrophysics*, **8**, 219-229.
https://doi.org/10.4236/ijaa.2018.83016

Received: April 18, 2018
Accepted: July 16, 2018
Published: August 8, 2018

Abstract

We analyse the possibility that the observed cosmological redshift may be cumulatively due to the expansion of the universe and the tired light phenomenon. Since the source of both the redshifts is the same, they both independently relate to the same proper distance of the light source. Using this approach we have developed a hybrid model combining the Einstein de Sitter model and the tired light model that yields a slightly better fit to Supernovae Ia redshift data using one parameter than the standard ΛCDM model with two parameters. We have shown that the ratio of tired light component to the Einstein de Sitter component of redshift has evolved from 2.5 in the past, corresponding to redshift 1000, to its present value of 1.5. The hybrid model yields Hubble constant $H_0 = 69.11(\pm 0.53)\,\text{km}\cdot\text{s}^{-1}\cdot\text{Mpc}^{-1}$ and the deceleration parameter $q_0 = -0.4$. The component of Hubble constant responsible for expansion of the universe is 40% of H_0 and for the tired light is 60% of H_0. Consequently, the critical density is only 16% of its currently accepted value; a lot less dark matter is needed to make up the critical density. In addition, the best data fit yields the cosmological constant density parameter $\Omega_\Lambda = 0$. The tired light effect may thus be considered equivalent to the cosmological constant in the hybrid model.

Keywords

Galaxies: Distances and Redshifts, Cosmological Parameters, Cosmic Background Radiation, Distance Scale, Cosmology Theory

1. Introduction

Until the discovery of cosmic microwave background radiation by Penzias and Wilson in 1964 [1], there was a debate about the cause of the redshift of light from extragalactic objects. Since then expansion of the universe by the Big-Bang theory became more and more favoured explanation of the cause of the redshift rather than the tired light and steady state theories. Ironically, it is the close analysis of the cosmic microwave background that has put into question the cause of the redshift due to the discrepancy in the Hubble constant derived from the spectral data and the microwave background data [2] [3].

The Hubble constant that relates the redshift to the distance of the source of light has shown steady decline in its value from about 500 km·s^{-1}·Mpc^{-1} to the currently accepted value of about 69 km·s^{-1}·Mpc^{-1} with improvements in measuring techniques and availability of redshift-distance data for high redshift sources. However, many cosmological models seek even lower value of the Hubble constant. Since the value of the Hubble constant determines plethora of cosmological parameters, including age, size and critical density of the universe, it is important to re-examine the potential causes of the redshift, or perhaps the composition of the redshift.

The status of the expanding universe and steady state theories has been recently reviewed by López-Corredoira [4] and Orlov and Raikov [5]. They concluded that based on the currently available observational data it is not possible to unambiguously identify the preferred approach to cosmology.

In a recent paper it was shown phenomenologically that Mach effect may be the cause of tired light redshift and may contribute dominantly to the cosmological redshift [6]. While the paper's assumption that observed redshift may be the hybrid of the expansion of the universe and tired light effect may be sound, it incorrectly divided the distance modulus between the two components rather than keeping the proper distance the same and dividing the redshift.

Using Poisson's work on the motion of point particles in curved spacetime [7], Fischer [8] has shown analytically that gravitational back reaction may be responsible for the tired light phenomenon and could account for some or most of the observed redshift. His finding may also be related to Mach effect.

Tired light, hereafter Mach effect, redshift approach defines the distance d of the light emitting source, whose redshift is z, by the equation:

$$d = R_0 \ln(1+z), \tag{1}$$

where $R_0 = c/H_0$ with c as the speed of light and H_0 as the Hubble constant. The same distance in the standard ΛCDM model is defined as [9]:

$$d = R_0 \int_0^z \left[\mathrm{d}u \Big/ \sqrt{\left(\Omega_{m,0}(1+u)^3 + \Omega_{\Lambda,0}\right)} \right], \tag{2}$$

where $\Omega_{m,0}$ is the matter energy density relative to the critical energy density, $\Omega_{\Lambda,0}$ is the relative energy density corresponding to the Einstein cosmological constant, and $\Omega_{m,0} + \Omega_{\Lambda,0} = 1$.

Distance d is determined from the measurement of the bolometric flux f of the light emitting source and comparing it with the standard for that type of source with known luminosity L. The luminosity distance d_L is defined as:

$$d_L = \sqrt{L/4\pi f}\ . \tag{3}$$

while the flux could normally be related to the luminosity L with an inverse square law $f = L/(4\pi d^2)$ in a flat universe, it needs to be modified to include the effects of the redshift, the expansion of the universe, and any other unknown phenomenon, in order to determine the distance d of the source correctly.

2. Theory

If we assume the observed redshift to be due to two effects, we need to find out that in what proportion two effects contribute to the observed redshift. Let z_X be the redshift due to expansion of the universe and z_M be the redshift due to the Mach effect—we will use subscript X for expansion of the universe and M for Mach effect. The expansion will cause the emission wavelength λ_e to stretch to wavelength λ_X such that $\lambda_X = (1+z_X)\lambda_e$. This wavelength will be further increased due to the Mach effect before it is observed as wavelength $\lambda_0 = (1+z_M)\lambda_X = (1+z_M)(1+z_X)\lambda_e$. But we can also write $\lambda_0 = (1+z)\lambda_e$. We may thus write:

$$1+z = (1+z_X)(1+z_M). \tag{4}$$

Considering now the scale factor $a(t)$ relating the proper distance d to the comoving distance r between the galaxies, it can only depend on the component of the redshift that is due to the expansion of the universe rather than the whole redshift; *i.e.* $a_X(t) = 1/(1+z_X)$ should be used as the scale factor.

Let us estimate the loss of the flux of light in the measurement of the luminosity of an object due to:

1) Expansion of the universe:

a) Stretching of the wavelength $\propto 1/(1+z_X)$, and

b) Increase in time between photon detection $\propto a_X(t) = 1/(1+z_X)$.

Thus the flux is reduced to $f_X = f/(1+z_X)^2$.

2) Mach effect: It is only due to the increase in wavelength $\propto 1/(1+z_M)$.

And the flux is reduced to $f_M = f_X/(1+z_M)$.

3) Unknown factor: We found that there is an additional flux loss $\propto 1/\sqrt{1+z}$.

The measured bolometric flux may thus be written as:

$$f_B = L/\left[4\pi d^2 (1+z_X)^2 (1+z_M)\sqrt{1+z}\right]. \tag{5}$$

The luminosity distance may now be written as:

$$\begin{aligned} d_L &= d(1+z_X)(1+z_M)^{\frac{1}{2}}(1+z)^{\frac{1}{4}} \\ &= d(1+z_X)^{\frac{1}{2}}(1+z)^{\frac{1}{2}}(1+z)^{\frac{1}{4}} \end{aligned} \tag{6}$$

Since the proper distance d, often written as $d_P(t)$, determined using either of the above models must be the same, equating them can give relationship between z_X and z_M, and also determine the deceleration parameter q_0 in the limit of $z \ll 1$. We may rewrite Equation (1) for Mach effect as:

$$d_M = R_M \ln(1+z_M). \tag{7}$$

Here $R_M = c/H_M$ with H_M being the Hubble constant corresponding to the Mach effect. Regarding Equation (2) for the expansion model, we will be exploring how the density parameters, taken usually as $\Omega_{m,0} = 0.3$ and $\Omega_{\Lambda,0} = 0.7$, are impacted with the inclusion of Mach effect. We will start with $\Omega_{m,0} = 1$, which corresponds to the Einstein de Sitter model. It can be expressed as:

$$d_X = 2R_X\left(1 - \frac{1}{\sqrt{1+z_X}}\right). \tag{8}$$

Here $R_X = c/H_X$ with H_X being the Hubble constant corresponding to the expansion model considered. We can use the limit $z = z_X = z_M \Rightarrow 0$ as the boundary condition for Equation (7) and Equation (8); they both should reduce to the Hubble's law $d = R_0 z$. Expanding the two equations in the limit yields:

$$d_M(t_0) = R_M z_M\left(1 - \frac{1}{2}z_M + \cdots\right), \text{ and} \tag{9}$$

$$d_X(t_0) = R_X z_X\left(1 - \frac{3}{4}z_X - \cdots\right). \tag{10}$$

This yields $R_0 z = R_M z_M = R_X z_X$. In the limit, we may write Equation (4) as $z = z_X + z_M$, or $z = (1-w)z + wz$ where w is the weight factor of Mach effect component and $1-w$ is the weight factor for the expansion component. Comparing these equations with the text book expression for proper distance to a galaxy with redshift z [10] and deceleration parameter q_0 in the limit $z \Rightarrow 0$:

$$d_P(t_0) = R_0 z\left[1 - \frac{1}{2}(1+q_0)z\right], \tag{11}$$

we get for the case of Mach effect $(1+q_0)z/2 = z_M/2 = wz/2$, or $q_0 = w-1$. And for the case of Einstein de Sitter model $(1+q_0)z/2 = 3z_X/4 = 3(1-w)z/4$, or $q_0 = (1-3w)/2$. Equating the two q_0, we get $w = 0.6$ and $q_0 = -0.4$. The same exercise can be done with Equation (2) with $\Omega_{m,0} \equiv b$ and $\Omega_{\Lambda,0} \equiv 1-b$. The equation near $u = 0$ may be written as:

$$\begin{aligned} d_X(t_0) &= R_X\int_0^{z_X}\left[du\left(1 - \frac{3}{2}bu + \frac{3}{8}b(9b-4)u^2 - \cdots\right)\right] \\ &= \frac{R_X}{8}z_X(8 - 6bz_X + \cdots) \\ &= R_0 z\left(1 - \frac{3}{4}b(1-w)z + \cdots\right) \end{aligned} \tag{12}$$

Thus, $1+q_0 = 3b(1-w)/2$ for this model. Equating it with $1+q_0 = w$ for Mach effect, we get $w = 1\Big/\left(1+\dfrac{2}{3b}\right)$ and $q_0 = -1\Big/\left(1+\dfrac{3}{2}b\right)$. Noting that for Einstein de Sitter model $b = 1$, we get $w = 0.6$ and $q_0 = -0.4$, the same as above. For standard ΛCDM as expansion model, taking $b = 0.3$, we get $w = 0.31$ and $q_0 = -0.69$.

The above analysis yields contribution to Hubble constant by the expansion of the universe $H_X = 0.4H_0$ and by Mach effect $H_M = 0.6H_0$ when using Einstein de Sitter model for the expansion of the universe, and $H_X = 0.69H_0$ and

$H_M = 0.31H_0$ when using ΛCDM as the expansion model. The data analysis presented in the next section will determine the best parameters.

Let us now see how z_X, z_M and z are related for all values of z, rather than in the limit of $z \ll 0$. Equating d_M and d_X —Equation (7) and Equation (8)—and using Equation (4) we get:

$$R_M \ln\left(1+z_M\right) = 2R_X\left(1-\frac{1}{\sqrt{1+z_X}}\right), \text{ or}$$

$$\frac{R_0 z}{z_M}\ln\left[\frac{1+z}{1+z_X}\right] = \frac{2R_0 z}{z_X}\left(1-\frac{1}{\sqrt{1+z_X}}\right), \text{ or}$$

$$\ln\left(\frac{y}{x}\right) = \frac{2\left(y-x\right)}{x\left(x-1\right)}\left(1-\frac{1}{\sqrt{x}}\right), \tag{13}$$

where for brevity we have substituted $y=1+z$ and $x=1+z_X$. This can be numerically solved to determine x for any y, and thus z_X for any z and also z_M for any z since $1+z_M = \left(1+z\right)/\left(1+z_X\right)$. Equation (6), Equation (8), and Equation (13), may now be combined to relate the luminosity distance d_L with the observed redshift z. As the measured quantity is the distance modulus μ, not the luminosity distance d_L, we will use the relation:

$$\mu = 5\log\left(d_L\right)+25, \text{ or}$$

$$\mu = 5\log\left(\frac{2R_0\left(y-1\right)}{x-1}\left(1-\frac{1}{\sqrt{x}}\right)\sqrt{xy}\right)+1.25\log\left(y\right)+25. \tag{14}$$

We have used Equation (8) for proper distance in Equation (6). However, we could also use Equation (7) in Equation (6) without any change in the result since Equation (13) has already established equality of the two expressions determining the proper distance.

We could also use Equation (2) for the proper distance in the expanding universe model, equate it to the Mach effect proper distance:

$$R_M \ln\left(1+z_M\right) = R_X\int_0^{z_X}\left[\mathrm{d}u\Big/\sqrt{\left(\Omega_{m,0}\left(1+u\right)^3+1-\Omega_{m,0}\right)}\right], \tag{15}$$

follow the same exercise as for Equation (13) to relate z_X, z_M and z, and then write the distance modulus relation:

$$\mu = 5\log\left(\frac{R_0\left(y-1\right)}{x-1}\int_0^{x-1}\left[\mathrm{d}u\Big/\sqrt{\left(\Omega_{m,0}\left(1+u\right)^3+1-\Omega_{m,0}\right)}\right]\sqrt{xy}\right) \\ +1.25\log\left(y\right)+25 \tag{16}$$

3. Analysis Using Observational μ, z Database

The database used in this study is for 580 SNe Ia data points with redshifts $0.015 \le z \le 1.414$ as compiled in the Union2 μ, z database [11] updated to 2017.

We used Matlab curve fitting tool to fit the data using non-linear least square regression. To minimize the impact of large scatter of data points, we applied the "Robust Bi-square" method. This tool fits data by minimizing the summed square of the residuals, and reduces the weight of outliers using bisquare weights. The Goodness of Fit is given by parameters SSE (sum of squares due to errors), R-Square and RMSE (root mean square error).

Our objective is to see how well the composite model fits the observational data as compared to the standalone Mach effect model and the expansion models. The results are presented graphically in **Figure 1**, and numerically in **Table 1**; the table has one extra entry that is discussed below.

The first case is the standard ΛCDM model with two parameter fit, H_0 and Ω_m. The values determined for the parameters are as expected. It provides a good two-parameter fit. This model has the legend "ΛCDM" in **Figure 1**.

In the second case, we have created a composite model by including Mach effect in the first case. The data fit is obtained using Equation (16). The Goodness of Fit numbers have slightly deteriorated compared to the first case. There is a slight decrease in the value of H_0. However, the matter energy density has become almost 1, the same as for the Einstein de Sitter ("EdeS") model. One could therefore infer that Mach effect is equivalent to cosmological constant!

The third case is for the Einstein de Sitter model. The Goodness of Fit is not good. Also, the Hubble constant value is significantly lower than the previous cases. This model has the legend "EdeS" in **Figure 1**.

The fourth case is the composite model consisting of the Einstein de Sitter model and the Mach effect. Now the worst case has become the best overall fit case. Hubble constant is slightly lower than for ΛCDM models. This model has the legend "EdeS + Mach" in **Figure 1**.

The last case considered here is for Mach effect. It presents a not-so-good (OK) one-parameter fit. The Hubble constant value is the highest ($H_0 = 70.52$) of all the cases included here. This model has the legend "Mach" in **Figure 1**.

It may thus be concluded that the *one-parameter* (H_0) Einstein de Sitter-Mach ("EDSM") composite model is slightly better than the *two-parameter*

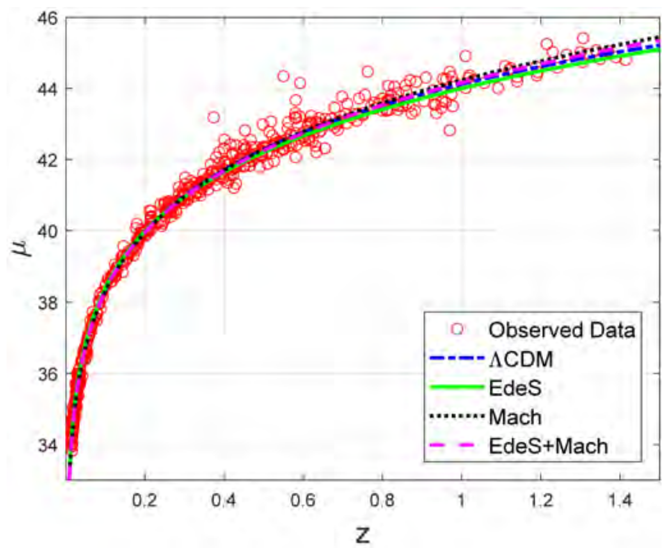

Figure 1. Fitted data curves for four models in **Table 1**.

Table 1. Parameters and "Goodness of Fit" for the analysed models, including those whose plots are shown in **Figure 1**.

Model	Parameter	95% Confidence		Parameter	95% Confidence		Goodness of Fit			
	H_0	H_0 Low	H_0 High	Ω_m	Ω_m Low	Ω_m High	SSE	R-Square	RMSE	Comment
ΛCDM	**69.85**	70.71	69.01	**0.2877**	0.2489	0.3266	24.35	0.9959	0.2053	Best 2 parameter fit
ΛCDM + Mach	**69.14**	70.00	68.20	**0.9949**	0.8082	1.182	24.46	0.9959	0.2057	Good 2 parameter fit
EdeS	**66.30**	66.82	65.72	**1**	Fixed	Fixed	28.68	0.9951	0.2226	Bad 1 parameter fit
EdeS + Mach	**69.11**	69.61	68.54	**1**	Fixed	Fixed	24.32	0.9951	0.2049	Best fit - 1 parameter
Mach	**70.52**	71.04	69.93	**NA**	NA	NA	25.54	0.9957	0.2100	OK 1 parameter fit

(H_0, Ω_m) ΛCDM model for fitting the redshift data while yielding a 1% lower value of the Hubble constant.

We have shown the z (and hence the time) dependence of the new scale factor a_X and other relevant parameter calculated in the EDSM model in **Table 2** using Equation (13). It does not involve any fitting of the data, just the model. The conventional scale factor is $1/(1+z)$. We see that while the two scale factors are the same at $z = 0$ and about the same at the lowest non-zero value in the table, a_X decreases much more slowly than $1/(1+z)$ with increasing z. This is expected as only a portion z_X of z is due to the expansion of the universe, the remaining z_M being due to the Mach effect. **Figure 2** shows on a log-log grid how the new scale factor a_X compares with the conventional scale factor $1/(1+z)$. The fit to the calculated values is reasonably well represented by $a_X(z) = (1+z)^{-0.42}$, especially al lower values of z, say up to $z = 10$. This may be easier to use in some calculations than numerically solving Equation (13).

The ratio z_M/z_X is also shown in the table. It increases from the present value of 1.5 to 2.5 for the redshift going from 0 to about 1000, meaning that Mach effect was contributing 71% to the redshift then compared to 60% now.

One question naturally arises: How is the cosmological constant of the ΛCDM model related to the Mach effect of the EDSM model? The question is best answered by analysing the Friedmann equation. The simplest Friedmann equation containing the cosmological constant Λ is for the spatially flat universe [10]:

$$H(t)^2 \equiv \left(\frac{\dot{a}}{a}\right)^2 = \frac{8\pi G}{3c^2}\varepsilon + \frac{\Lambda}{3}. \tag{17}$$

Here a is the cosmological scale factor, $\dot{a}$ is the time derivative of the scale factor, G is the gravitational constant, and ε is the energy density. Equation (17) is based on the assumption that all the redshift relates to the velocity of the expansion of the universe: $cz \equiv v(t) = H(t)d(t)$. In the EDSM model, $cz_X \equiv v(t) = H_X(t)d(t)$, and hence the scale factor that represents the expansion of the universe is really $a_X\left[\equiv 1/(1+z_X)\right]$ with no Λ. So, we may write the Friedmann equation for the spatially flat universe as:

$$H_X(t)^2 \equiv \left(\frac{\dot{a}_X}{a_X}\right)^2 = \frac{8\pi G}{3c^2}\varepsilon \tag{18}$$

Table 2. Parameters based on the numerical solution of Equation (13). The conventional scale factor $a(t)$ is normally taken as $1/(1+z)$. Here we designate the scale factor as $a_X(z)$ since the expansion of the universe is determined by a fraction of the redshift.

z	z_X	z_M	$1/(1+z)$	$a_x(z)$	z_M/z_X
0.0000	0.0000	0.0000	1.0000	1.0000	1.5000
0.014959	0.00595	0.008956	0.985261	0.994085	1.5052
0.522439	0.1847	0.285084	0.656841	0.844096	1.543497
1.283658	0.3986	0.632817	0.437894	0.715001	1.5876
2.425487	0.6549	1.069906	0.291929	0.604266	1.633694
4.138231	0.9621	1.618741	0.19462	0.509658	1.682508
6.707347	1.3308	2.306739	0.129746	0.429037	1.733347
10.56102	1.7735	3.168386	0.086498	0.360555	1.786516
16.34153	2.3055	4.246265	0.057665	0.302526	1.841798
25.01229	2.9451	5.59357	0.038443	0.253479	1.89928
38.01844	3.7145	7.276263	0.025629	0.212112	1.958881
57.52766	4.6405	9.376325	0.017086	0.177289	2.020542
86.7915	5.7555	11.99556	0.011391	0.148028	2.084191
130.6872	7.0986	15.26049	0.007594	0.123478	2.149789
196.5309	8.717	19.32838	0.005063	0.102912	2.21732
295.2963	10.6679	24.39414	0.003375	0.085705	2.286686
443.4444	13.0203	30.70007	0.00225	0.071325	2.357862
665.6667	15.8578	38.54648	0.0015	0.05932	2.430758
999	19.2814	48.30626	0.001	0.049306	2.50533

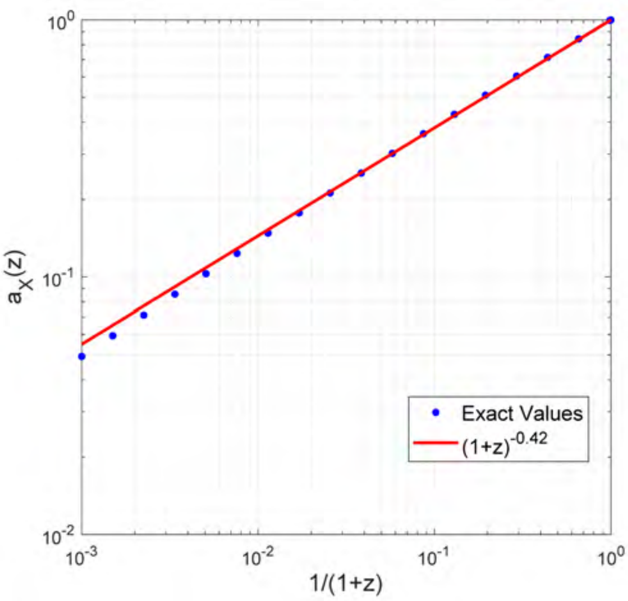

Figure 2. Variation of the new scale factor a_X with the conventional scale factor $1/(1+z)$ plotted on a log-log grid. Calculated values using Equation (13) are shown as blue dots. Also is shown a power fit curve in red.

Subtracting Equation (18) from Equation (17):

$$\frac{\Lambda}{3} = H(t)^2 - H_X(t)^2. \tag{19}$$

The right hand side of Equation (19) represents the Mach effect. At $t = t_0$:

$$\Lambda = 3H_0^2\left(1-0.4^2\right) = 2.52H_0^2 = 1.22\times10^{-35}\ \text{s}^{-2}. \tag{20}$$

We have assumed $H_0 = 68\ \text{km}\cdot\text{s}^{-1}\cdot\text{Mpc}^{-1} = 2.2\times10^{-18}\ \text{s}^{-1}$. Dividing by c^2, $\Lambda = 1.36\times10^{-52}\ \text{m}^{-2}$. In terms of the density parameter, the Mach effect contribution is therefore equivalent to $\Omega_\Lambda = 0.84$. However, unlike the true cosmological constant, this one is not constant and has time dependence expressed by Equation (19). One could infer that the dark energy is replaced by Mach effect.

Since Equation (18) represents the expansion of the universe, it also determines the critical density rather than Equation (17). It can be easily seen that the new critical density is only 16% of the generally accepted critical density since $H_X = 0.4H_0$. And since all the density parameters are expressed relative to the critical density, one could easily see that the baryon density parameter would get a boost by a factor of 6.25. Consequently, the dark matter requirement is drastically reduced.

Another concern: Can the EDSM model explain the time-dilation in type Ia Supernovae and gamma-ray bursts (GRB)? Blondin *et al.* [12] have shown that the time dilation in Supernovae Ia is proportional to the $(1+z)^{-1}$. This finding is considered by many cosmologist, including López-Corredoira [4] and Orlov and Raikov [5], as inconsistent with other findings, and by Crawford [13], as flawed. Hawkins [14] did not find any time dilation in 878 quasars. Chang [15] studied time dilation in GRB with measured redshift and did not get any conclusive evidence of time dilation. It would be interesting to explore if EDSM model can reconcile such discrepancies as it could explain time dilation proportional to $(1+z_X)^{-1}$, which is significantly less than the time dilation proportional to $(1+z)^{-1}$ of ΛCDM model; the smaller time dilation of EDSM model fits well within the error bars in the paper of Blondin *et al.* [12].

At this early stage of the development of EDSM model, we have not attempted to explain other cosmological phenomena, such as baryonic acoustic oscillations and nucleosynthesis. However, since the EDSM model involves both the Mach effect and the expansion of the universe, the latter due presumably to the big-bang, these phenomena should be possible to account for using the EDSM model albeit with different parameters than the ΛCDM model.

Advantages of the EDSM model over ΛCDM model:

1) EDSM model needs only one adjustable parameter to fit the data, the Hubble constant, whereas ΛCDM model needs two adjustable parameters; it does not require the cosmological constant.

2) EDSM model keeps the expansion model which is essential for explaining the cosmic microwave background.

3) EDSM model predicts a negative deceleration parameter in compliance

with observations, albeit a different value than the ΛCDM model.

4) EDSM's Mach effect contribution to the redshift may be deemed equivalent to the cosmological constant in ΛCDM model; there is no need for a controversial constant density parameter that leads to the continuous creation of energy from nothing as universe expands.

5) EDSM model may be considered a simpler model from the viewpoint of Occam's razor having dispensed with ad-hoc assumptions, and dependent only on one verifiable adjustable parameter, the Hubble constant; it does not have conceptual problems associated with the ΛCDM model.

6) EDSM model has the potential to explain time dilation claimed to be present in Supernova Ia and some GRB measurements albeit differently than the ΛCDM model.

4. Conclusions

The extragalactic redshift results not only from the expansion of the universe but also from light losing energy in traveling vast distances from source to observer. By combining the two, through the fact that both the contributions to the redshift measure the same proper distance of the source, we have come up with a one parameter model that fits the redshift SNe Ia data with the same Goodness of Fit as the standard ΛCDM model that requires an additional adjustable parameter. The new model, dubbed EDSM, yields:

1) The Hubble constant $H_0 = 69.11(\pm 0.53)$ km/s/Mpc.

2) The deceleration parameter $q_0 = -0.4$.

3) The Λ equivalent for EDSM model $= 1.2\times 10^{-35}\ \mathrm{s}^{-2}$ $\left(1.4\times 10^{-52}\ \mathrm{m}^{-2}\right)$, *i.e.* $\Omega_\Lambda = 0.84$.

4) The variation of the expansion scale factor with z that is substantially less steeper than $1/(1+z)$.

5) The Hubble constant component that results from the expansion of the universe is $0.4H_0$ and that from Mach effect is $0.6H_0$.

6) A boost to baryon density parameter by a factor of 6.25, resulting in a greatly reduced dependence on dark matter to explain cosmology.

Acknowledgements

I am thankful to Professor Ethan Vishniac and Professor James Peebles for their critical comments on a previous paper that led me to rethink and develop the new approach presented in this paper. I am also thankful to Professor Martin López-Corredoira for his review and suggestions on an early draft of this paper which among other things resulted in the inclusion of ΛCDM models in this study. I am grateful to Dr. Ernst Fischer, Dr. Laszlo Marosi and Dr. David Crawford for sharing their recent research work with me.

Conflicts of Interest

The authors declare no conflicts of interest regarding the publication of this paper.

References

[1] Penzias, A.A. and Wilson, R.W. (1965) A Measurement of Excess Antenna Temperature at 4080 Mc/s. *The Astrophysical Journal*, **142**, 419-421. https://doi.org/10.1086/148307

[2] Lineweaver, C.H. and Barbosa, D. (1998) Cosmic Microwave Background Observations: Implications for Hubble's Constant and the Spectral Parameters N and Q in Cold Dark Matter Critical Density Universes. *Astronomy & Astrophysics*, **329**, 799-808.

[3] Blanchard, A., Douspis, M., Rowan-Robinson, M. and Sarkar, S. (2003) An Alternative to the Cosmological "Concordance Model". *Astronomy & Astrophysics*, **412**, 35-44. https://doi.org/10.1051/0004-6361:20031425

[4] López-Corredoira, M. (2017) Test and Problems of the Standard Model in Cosmology. *Foundations of Physics,* **47**, 711-768. https://doi.org/10.1007/s10701-017-0073-8

[5] Orlov, V.V. and Raikov, A.A. (2016) Cosmological Tests and Evolution of Extragalactic Objects. *Astronomy Reports*, **60**, 477-485. https://doi.org/10.1134/S1063772916030112

[6] Gupta, R.P. (2018) Mass of the Universe and the Redshift. *International Journal of Astronomy and Astrophysics*, **8**, 68-78. https://doi.org/10.4236/ijaa.2018.81005

[7] Poisson, E. (2004) The Motion of Point Particles in Curved Spacetime. Living Reviews in Relativity*,* **7**, 6. https://doi.org/10.12942/lrr-2004-6

[8] Fischer, E. (2007) Redshift from Gravitational Back Reaction. arXivastro-ph/0703791

[9] Peebles, P.J.E. (1993) Principles of Physical Cosmology. Princeton, NJ.

[10] Ryden, B. (2017) Introduction to Cosmology. Cambridge, UK.

[11] Amanullah, R., *et al.* (2010) Spectra and Hubble Space Telescope Light Curves of Six Type Ia Supernovae at 0.511 < z < 1.12 and the UNION2 Compilation. *The Astrophysical Journal*, **716**, 712-738. https://doi.org/10.1088/0004-637X/716/1/712

[12] Blondin, S., *et al.* (2008) Time Dilation in Type Ia Supernova Spectra at High Redshift. *The Astrophysical Journal*, **682**, 724-736. https://doi.org/10.1086/589568

[13] Crawford, D.F. (2017) A Problem with the Analysis of Type Ia Supernovae. *Open Astronomy,* **26**, 111-119. https://doi.org/10.1515/astro-2017-0013

[14] Hawkins, M.R.S. (2010) On Time Dilation in Quasar Light Curves. *Monthly Notices of the Royal Astronomical Society,* **405**, 1940-1946. https://doi.org/10.1111/j.1365-2966.2010.16581.x

[15] Chang, H.-Y. (2001) Fourier Analysis of Gamma-Ray Burst Light Curves: Searching for a Direct Signature of Cosmological Time Dilation. *The Astrophysical Journal*, **557**, L85-L88. https://doi.org/10.1086/323331

International Journal of Astronomy and Astrophysics, 2018, 8, 230-257
http://www.scirp.org/journal/ijaa
ISSN Online: 2161-4725
ISSN Print: 2161-4717

Study of Galaxy Distributions with SDSS DR14 Data and Measurement of Neutrino Masses

B. Hoeneisen

Universidad San Francisco de Quito, Quito, Ecuador
Email: bhoeneisen@usfq.edu.ec

How to cite this paper: Hoeneisen, B. (2018) Study of Galaxy Distributions with SDSS DR14 Data and Measurement of Neutrino Masses. *International Journal of Astronomy and Astrophysics*, **8**, 230-257.
https://doi.org/10.4236/ijaa.2018.83017

Received: June 5, 2018
Accepted: August 20, 2018
Published: August 23, 2018

Abstract

We study galaxy distributions with Sloan Digital Sky Survey SDSS DR14 data and with simulations searching for variables that can constrain neutrino masses. To be specific, we consider the scenario of three active neutrino eigenstates with approximately the same mass, so $\sum m_\nu = 3m_\nu$. Fitting the predictions of the ΛCDM model to the Sachs-Wolfe effect, σ_8, the galaxy power spectrum $P_{\text{gal}}(k)$, fluctuations of galaxy counts in spheres of radii ranging from $16/h$ to $128/h$ Mpc, Baryon Acoustic Oscillation (BAO) measurements, and $h = 0.678 \pm 0.009$, in various combinations, *with free spectral index n*, and free galaxy bias *and galaxy bias slope*, we obtain consistent measurements of $\sum m_\nu$. The results depend on *h*, so we have presented confidence contours in the $\left(\sum m_\nu, h\right)$ plane. A global fit with $h = 0.678 \pm 0.009$ obtains $\sum m_\nu = 0.719 \pm 0.312(\text{stat})^{+0.055}_{-0.028}(\text{syst})$ eV, and the amplitude and spectral index of the power spectrum of linear density fluctuations $P(k)$: $N^2 = (2.09 \pm 0.33) \times 10^{-10}$, and $n = 1.021 \pm 0.075$. The fit also returns the galaxy bias b including its scale dependence.

Keywords

Neutrino Mass, Galaxy Power Spectrum

1. Introduction

We measure neutrino masses by comparing the predictions of the ΛCDM model with measurements of the power spectrum of linear density perturbations $P(k)$. We consider three measurements of $P(k)$: 1) the Sachs-Wolfe effect of fluctuations of the Cosmic Microwave Background (CMB) which is a direct measurement of density fluctuations [1] [2]; 2) the relative mass fluctuations σ_8

in randomly placed spheres of radius $r_s = 8/h$ Mpc with gravitational lensing and studies of rich galaxy clusters [2] [3]; and 3) measurements of $P(k)$ inferred from galaxy clustering with the Sloan Digital Sky Survey [4] [5] [6]. Baryon Acoustic Oscillations (BAO) were considered separately [7] [8] and are not included in the present study, except for the final combinations.

To be specific, we consider three active neutrino eigenstates with nearly the same mass, so $\sum m_\nu = 3m_\nu$. This is a useful scenario to consider because the current limits on m_ν^2 are much larger than the mass-squared-differences Δm^2 and Δm_{21}^2 obtained from neutrino oscillations [3].

Figures 1-4 illustrate the problem at hand. **Figures 1-3** present measurements of the "reconstructed" galaxy power spectrum $P_{gal}(k)$ obtained from the SDSS-III BOSS survey [4], while **Figure 4** presents the corresponding "standard" $P_{gal}(k)$. The "reconstructed" $P_{gal}(k)$ is obtained from the directly measured "standard" $P_{gal}(k)$ by subtracting peculiar motions to obtain the power spectrum prior to non-linear clustering. Also shown are various fits to this data (with floating normalization), and to measurements of the Sachs-Wolfe effect, and σ_8. The Sachs-Wolfe effect normalizes $P(k)$, within its uncertainty, in the approximate range of $\log_{10}\left(k/\left(h\,\text{Mpc}^{-1}\right)\right)$ from −3.1 to −2.7, while σ_8 is most sensitive to the range −1.3 to −0.6. Full details will be given in the main body of this article.

The fit in **Figure 1** corresponds to the function

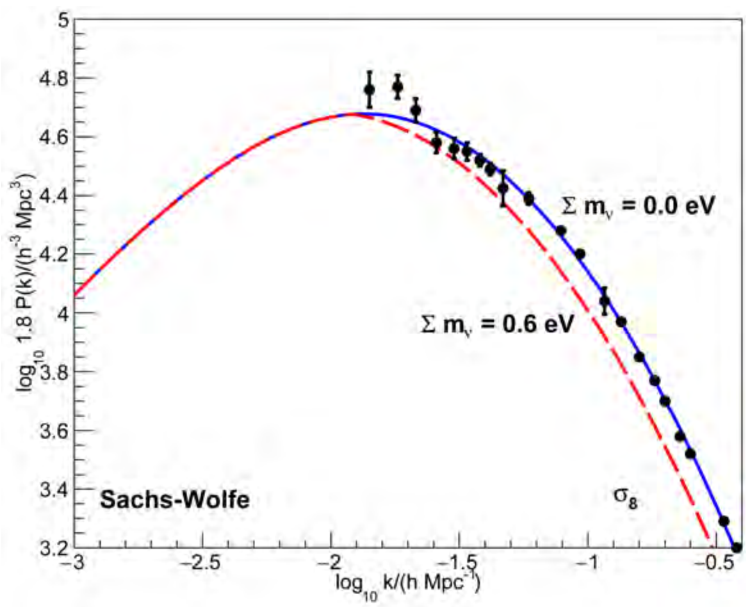

Figure 1. Comparison of $P_{gal}(k)$ obtained from the SDSS-III BOSS survey [4] ("reconstructed") with $b^2P(k)$ obtained from a fit of Equation (5) with $\sum m_\nu = 0$ eV to the Sachs-Wolfe effect, σ_8, and $P_{gal}(k)$. The fit obtains $A = 8738\ \text{Mpc}^3$, $k_{eq} = 0.068h\ \text{Mpc}^{-1}$, $\eta = 4.5$, and $b^2 = 1.8$, with $\chi^2 = 24.7$ for 19 degrees of freedom. Also shown for comparison is the curve with the same parameters, except $\sum m_\nu = 0.6$ eV.

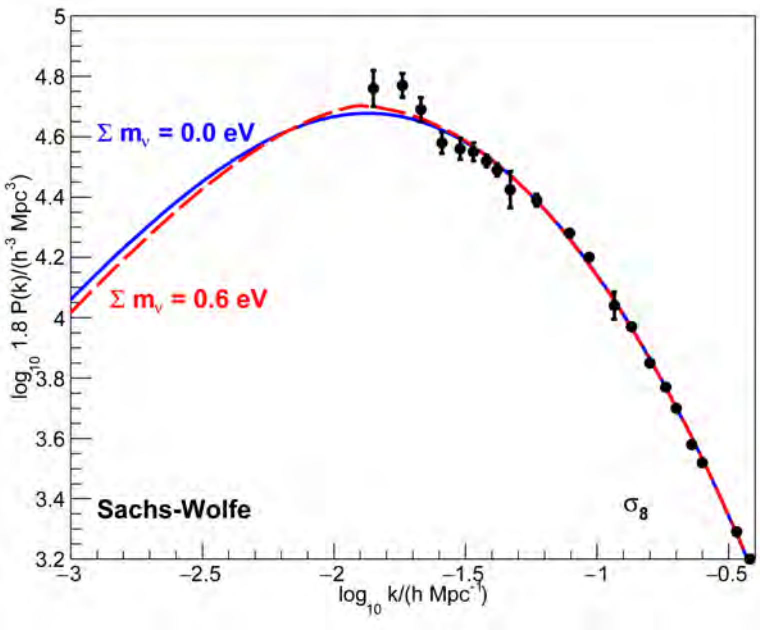

Figure 2. Same as **Figure 1**, except that the curve "$\sum m_\nu = 0.6$ eV" is fit. We obtain $A = 9312\ \text{Mpc}^3$, $k_{\text{eq}} = 0.080h\ \text{Mpc}^{-1}$, $\eta = 4.2$, and $\kappa = 1.8$, with $\chi^2 = 21.8$ for 19 degrees of freedom. Note that $\sum m_\nu$ is largely degenerate with the remaining parameters in Equation (5), unless we are able to constrain k_{eq}.

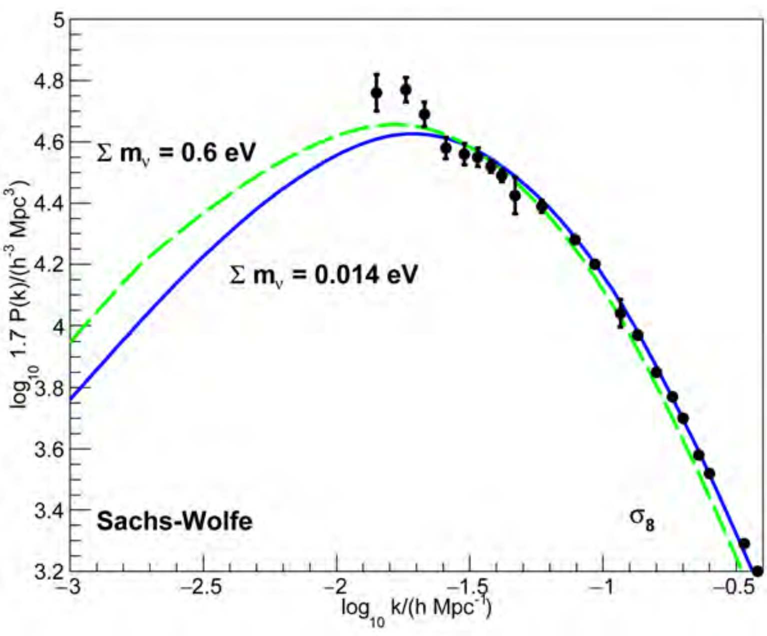

Figure 3. Comparison of $P_{\text{gal}}(k)$ obtained from the SDSS-III BOSS survey [4] ("reconstructed") with $b^2 P(k)$ obtained from a fit of Equation (6) to the Sachs-Wolfe effect, σ_8, and $P_{\text{gal}}(k)$. The fit obtains $\sum m_\nu = 0.014 \pm 0.079$ eV, $N^2 = (1.41 \pm 0.12) \times 10^{-10}$, and $b^2 = 1.7 \pm 0.1$, with $\chi^2 = 47$ for 20 degrees of freedom (so the statistical uncertainties shown need to be multiplied by $\sqrt{47/20}$). Also shown is the fit with $\sum m_\nu = 0.6$ eV fixed for comparison.

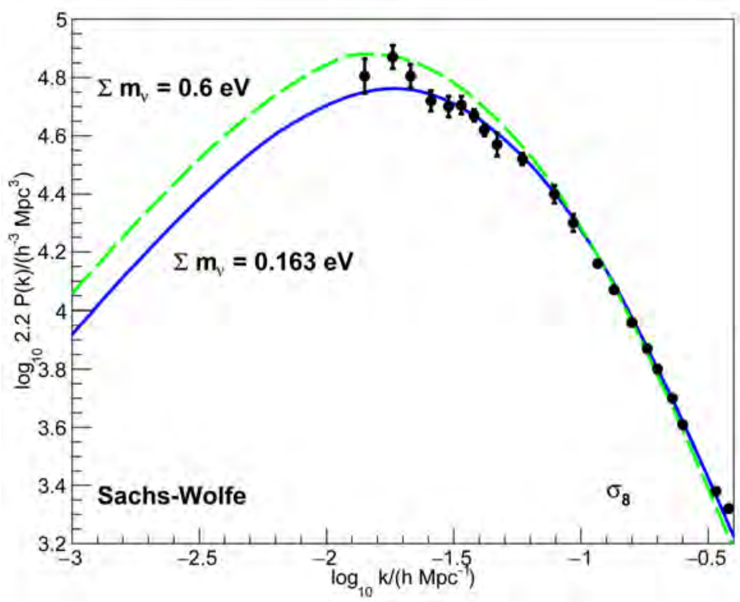

Figure 4. Comparison of $P_{gal}(k)$ obtained from the SDSS-III BOSS survey [4] ("standard") with $b^2P(k)$ obtained from a fit of Equation (6) to the Sachs-Wolfe effect, σ_8, and $P_{gal}(k)$. The fit obtains $\sum m_\nu = 0.163 \pm 0.061$ eV, $N^2 = (1.56 \pm 0.12) \times 10^{-10}$, and $b^2 = 2.2 \pm 0.2$, with $\chi^2 = 33.9$ for 20 degrees of freedom (so the statistical uncertainties shown need to be multiplied by $\sqrt{33.9/20}$). Also shown is the fit with $\sum m_\nu = 0.6$ eV fixed for comparison.

$$P'(k) \equiv \frac{(2\pi)^3 a_{20}^2 A w^n}{(1 + \eta w + w^2)^2}, \tag{1}$$

where $w \equiv k/k_{eq}$. Unless otherwise noted, we take the Harrison-Zel'dovich index $n = 1$ which is close to observations. The parameters A, η, and k_{eq}, as well as the normalization factor b^2, are free in the fit. The uncertainties of two data points that fall on BAO peaks are multiplied by three (since BAO is not included in $P'(k)$).

Also shown in **Figure 1** is the suppression of $P(k)$ for k greater than

$$k_{nr} = 0.018 \cdot \Omega_m^{1/2} \left(\frac{\sum m_\nu}{1\,\text{eV}} \right)^{1/2} h\,\text{Mpc}^{-1} \tag{2}$$

due to free-streaming of massive neutrinos that can not cluster on these small scales, and, more importantly, to the slower growth of structure with massive neutrinos [9]. The suppression factor for $k \gg k_{nr}$ for one massive neutrino, or three degenerate massive neutrinos, is

$$f\left(k, \sum m_\nu\right) \equiv \frac{P(k)^{f_\nu}}{P(k)^{f_\nu = 0}} = 1 - 8 f_\nu, \tag{3}$$

where $f_\nu = \Omega_\nu / \Omega_m$ [9]. Ω_m is the total (dark plus baryonic plus neutrino) matter density today relative to the critical density, and includes the contribution Ω_ν of neutrinos that are non-relativistic today. $\Omega_\nu = h^{-2}\sum m_\nu/93.04$ eV for three left-handed plus right-handed Majorana neutrino eigenstates, or three eigenstates of left-handed Dirac neutrinos plus three right-handed Dirac anti-neutrinos, that are non-relativistic today (right-handed Dirac neutrinos and left-handed Dirac anti-neutrinos are assumed to not have reached thermal and chemical equilibrium with the Standard Model particles). We take $f\left(k,\sum m_\nu\right)=1$ for $k<k_{\mathrm{nr}}/0.604$, and

$$f\left(k,\sum m_\nu\right)=1-0.407\frac{\sum m_\nu}{0.6\ \mathrm{eV}}\left[1-\left(\frac{k_{\mathrm{nr}}}{0.604k}\right)^{0.494}\right] \tag{4}$$

for $k>k_{\mathrm{nr}}/0.604$ and $\sum m_\nu<1.1$ eV, for galaxy formation at a redshift $z=0.5$ [9].

Figure 2 is the same as Figure 1 except that the function

$$P(k)=P'(k)\,f\left(k,\sum m_\nu\right) \tag{5}$$

with $\sum m_\nu=0.6$ eV is fit. We see that the parameter $\sum m_\nu$ is largely degenerate with the parameters A, η, and k_{eq}, so that only a weak sensitivity to $\sum m_\nu$ is obtained unless we are able to constrain k_{eq}. The power spectrum $P'(k)$ of Equation (1) neglects the growth of structure inside the horizon while radiation dominates.

The fits in Figure 3 and Figure 4 make full use of the ΛCDM theory. The fitted function is

$$P(k)=P''(k)\,f\left(k,\sum m_\nu\right), \tag{6}$$

where $P''(k)$ is given by [2]:

$$P''(k)=\frac{4(2\pi)^3N^2C^2k\tau^2\left(\sqrt{2}k/k_{\mathrm{eq}}\right)}{25\Omega_m^2H_0^4}\left(\frac{k_{\mathrm{SW}}}{k}\right)^{1-n}, \tag{7}$$

with

$$k_{\mathrm{eq}}=\frac{\sqrt{2}H_0\left(\Omega_m-\Omega_\nu\right)}{\sqrt{\Omega_r}}. \tag{8}$$

C is a function of Ω_Λ/Ω_m, and we take $C=0.767$ [2]. $\tau\left(\sqrt{2}k/k_{\mathrm{eq}}\right)$ is a function given in Reference [2]. The pivot point $k_{\mathrm{SW}}=0.001\ \mathrm{Mpc}^{-1}$ is chosen to not upset Equation (41) below. The fit depends on h, Ω_m, and the spectral index n, so we define $\delta h\equiv(h-0.678)/0.009$ [3], $\delta\Omega_m\equiv(\Omega_m-0.281)/0.003$ [7], and $\delta n\equiv(n-1)/0.038$ [3], and obtain, tentatively,

$$\begin{aligned}\sum m_\nu &= 0.014+0.162\cdot\delta h+0.807\cdot\delta n+0.142\cdot\delta\Omega_m\\ &\pm 0.079\sqrt{47/20}\,(\mathrm{stat})^{+0.005}_{-0.007}\,(\mathrm{syst})\,\mathrm{eV},\end{aligned} \tag{9}$$

by minimizing the χ^2 with respect to $\sum m_\nu$, and N^2. The statistical uncertainty has been multiplied by the square root of the χ^2 per degree of freedom. This result corresponds to the "reconstructed" data in Figure 3. The systematic uncertainties included are from the top-hat window function instead of the gaussian window function, and an alternative value of σ_8 (details will be given in Section 3). *Not included* is the systematic uncertainty due to the possible scale dependence of the galaxy bias *b*.

To obtain $P(k)$, we would like to measure the density $\rho(\boldsymbol{r}, z)$ at redshift *z*, but we only have information on the peaks of $\rho(\boldsymbol{r}, z)$ that have gone non-linear collapsing into visible galaxies. How accurate is the measurement of $P(k)$ with galaxies? The measurement of $P_{\text{gal}}(k)$ in Ref. [4] is based on a procedure described in [10] based on "the usual assumption that the galaxies form a Poisson sample [11] of the density field". In other words, the assumption is that the number density of point galaxies $n(\mathbf{x})$ is equal to its expected mean $\bar{n}$ (which depends on the position dependent galaxy selection criteria), modulated by the perturbation of the density field:

$$\frac{n(\boldsymbol{x})}{\bar{n}} = b\frac{\rho(\boldsymbol{x})}{\bar{\rho}} \equiv b\left(1+\delta_c(\boldsymbol{x})\right). \tag{10}$$

Both sides of this equation are measured or calculated at the same length scale, and at the same time. The "galaxy bias" *b* is explicitly assumed to be scale invariant. If we choose a region of space such that $\bar{n}$ is constant, then the galaxy power spectrum $P_{\text{gal}}(k)$ (derived from $n(\boldsymbol{x})/\bar{n}$) should be proportional, under the above assumption, to the power spectrum of linear density perturbations $P(k)$ (derived from $\delta_c(\boldsymbol{x})$) up to corrections:

$$P_{\text{gal}}(k) = b^2 P(k). \tag{11}$$

It is due to this bias *b* that we have freed the normalization of the measured $P_{\text{gal}}(k)$ in the fits corresponding to **Figures 1-4**.

In the following Sections we study galaxy distributions with SDSS DR14 data and with simulations, in order to understand their connection with the underlying power spectrum of linear density fluctuations $P(k)$. In the end we return to the measurement of neutrino masses.

2. The Hierarchical Formation of Galaxies

This Section allows a precise definition of $P(k)$, and an understanding of the connection between $P(k)$ and $P_{\text{gal}}(k)$. We generate galaxies as follows (see [12] for full details). The evolution of the Universe in the homogeneous approximation is described by the Friedmann equation

$$\frac{1}{H_0}\frac{1}{a_1}\frac{\mathrm{d}a_1}{\mathrm{d}t} \equiv E(a_1) = \sqrt{\frac{\Omega_r}{a_1^4} + \frac{\Omega_m}{a_1^3} + \frac{\Omega_k}{a_1^2} + \Omega_\Lambda}. \tag{12}$$

The expansion parameter $a_1(t)$ has been normalized to 1 at the present time t_0: $a_1(t_0) = 1$. H_0 has been normalized so $E(1) = 1$. Therefore H_0 is the present Hubble expansion rate. With these normalizations we have $\Omega_r + \Omega_m + \Omega_k + \Omega_\Lambda \equiv 1$. The matter density is $\rho_m(t) = \Omega_m \rho_c / a_1^3$, where $\rho_c = 3H_0^2/(8\pi G_N)$ is the critical density of the Universe. We are interested in the period after the density of matter exceeds the density of radiation. For our simulations we assume flat space, *i.e.* $\Omega_k = 0$, we neglect the radiation density

Ω_r, take $\Omega_\Lambda = 0.719$ constant [7], and the present Hubble expansion rate $H_0 = 100h\ \text{km}\cdot\text{s}^{-1}\cdot\text{Mpc}^{-1}$ with $h = 0.678$ [3]. The solution to Equation (12) with these parameters is shown by the curve "a_1" in Figure 5. The present age of the universe with these parameters is $t_0 = 14.1$ Gyr.

Setting $\Omega_\Lambda = 0$ we obtain the critical universe with expansion parameter

$$a_2 = \left[\frac{3H_0}{2}\right]^{2/3} \Omega_m^{1/3} t^{2/3}, \tag{13}$$

also shown in Figure 5. We note that $a_2(t_0) \equiv a_{20} = 0.846$. Let us now add density fluctuations to this critical universe and consider a density peak. The growing mode for this density peak is obtained by adding a negative Ω_k to the critical Universe. This prescription is exact if the density peak is spherically symmetric. An example with "expansion parameter" a_4 is presented in Figure 5. Note that a_4 grows to maximum expansion and then collapses to zero at time $t_4 = \pi\Omega_m \big/ \left[(-\Omega_k)^{3/2} H_0\right]$, and, in our model [12], a galaxy forms. In the example of Figure 5 the galaxy forms at redshift $z = 0.5$. $a_3(t)$ is the linear approximation to $a_4(t)$. In the linear approximation for growing modes the density fluctuations relative to ρ_2 grow in proportion to $a_2(t)$:

$$\delta_c \equiv \frac{\rho_3 - \rho_2}{\rho_2} = 3\frac{a_2 - a_3}{a_2} = -\frac{3\Omega_k}{5\Omega_m} a_2(t), \tag{14}$$

while $\delta_c \ll 1$. At the time t_4, when the galaxy forms, $\delta_c \equiv (\rho_3 - \rho_2)/\rho_2 = 1.69$ in the linear approximation (which has already broken down).

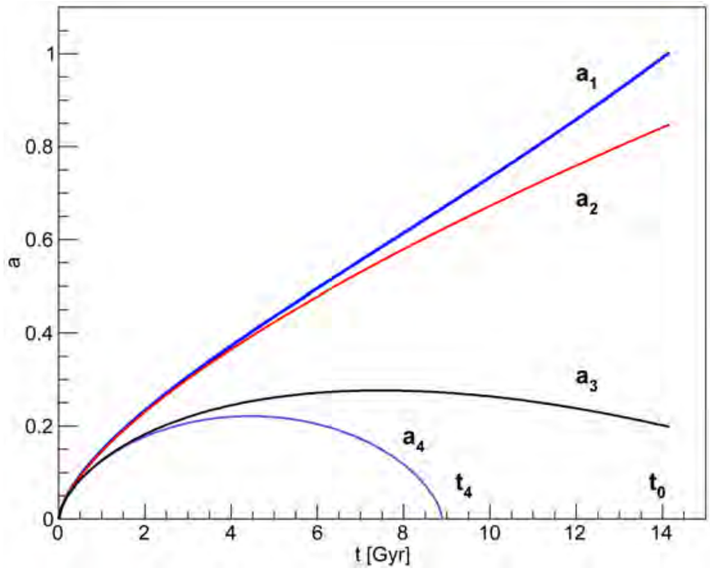

Figure 5. Expansion parameters as a function of time t of four solutions of the Friedmann equation. From top to bottom, a_1 corresponds to $(\Omega_m, \Omega_\Lambda, \Omega_k) = (0.281, 0.719, 0)$, a_2 corresponds to $(0.281, 0, 0)$, a_3 is the linear approximation to $(0.281, 0, -1.27)$, while a_4 is the exact solution to $(0.281, 0, -1.27)$. a_4 is the exact solution for the growing mode of a spherically symmetric density peak that collapses to a galaxy at t_4. In all cases $h = 0.678$.

In the linear approximation the density due to Fourier components of wave-vector $|\boldsymbol{k}| \le k_I$ is

$$\rho_{\text{lin}}(\boldsymbol{x},t,I) = \frac{\Omega_m \rho_c}{a_2^3}\left\{1+\delta_c(\boldsymbol{x},t,I)\right\}, \tag{15}$$

where

$$\delta_c(\boldsymbol{x},t,I) = \sum_{\boldsymbol{k},k\le k_I} |\delta_{\boldsymbol{k}}| a_2(t) \exp\left[i\frac{\boldsymbol{k}\cdot\boldsymbol{x}}{a_2(t)} + i\varphi_{\boldsymbol{k}}\right]. \tag{16}$$

$\varphi_{\boldsymbol{k}}$ are random phases. The sum of the Fourier series is over comoving wave-vectors that satisfy periodic boundary conditions in a rectangular box of volume $V = L_x L_y L_z$:

$$\boldsymbol{k} = 2\pi\left(\frac{n}{L_x}\hat{i} + \frac{m}{L_y}\hat{j} + \frac{l}{L_z}\hat{k}\right), \tag{17}$$

where $L_x = n_{\max} L_0$, $L_y = m_{\max} L_0$, $L_z = l_{\max} L_0$, $n,m,l = 0,\pm1,\pm2,\pm3,\cdots$, and

$$k_I = k_{\max}\frac{I}{I_{\max}} \tag{18}$$

where $k_{\max} = 2\pi/L_0$, and $I = 1,2,\cdots,I_{\max}$.

Inverting Equation (16) obtains

$$\delta_{\boldsymbol{k}} \equiv |\delta_{\boldsymbol{k}}| e^{i\varphi_{\boldsymbol{k}}} = \delta^*_{-\boldsymbol{k}} = \frac{1}{V}\int_V \frac{\delta_c(\boldsymbol{x},t)}{a_2(t)} \exp(-i\boldsymbol{k}\cdot\boldsymbol{X})\,\mathrm{d}^3\boldsymbol{X}, \tag{19}$$

where $\boldsymbol{X} \equiv \boldsymbol{x}(t)/a_2(t)$ is the comoving coordinate in the linear approximation. The power spectrum of density fluctuations

$$P(\boldsymbol{k}) \equiv V|\delta_{\boldsymbol{k}}|^2 a_{20}^2 \tag{20}$$

is defined in the linear approximation corresponding to a_3, and is approximately independent of V for large V. Averaging over $\boldsymbol{k}$ in a bin of $k \equiv |\boldsymbol{k}|$ obtains $P(k)$. Note that

$$\frac{1}{V}\sum_{\boldsymbol{k}} P(\boldsymbol{k}) = a_{20}^2 \sum_{\boldsymbol{k}} |\delta_{\boldsymbol{k}}|^2 = \frac{1}{V}\int_V \delta_c^2(\boldsymbol{x},t_0)\,\mathrm{d}^3\boldsymbol{X}. \tag{21}$$

Each term in this equation is approximately independent of V. The Fourier transform of the power spectrum is the correlation function:

$$\sum_{\boldsymbol{k}} P(\boldsymbol{k}) e^{i\boldsymbol{k}\cdot\boldsymbol{X}} = \int_V \delta_c(\boldsymbol{x}',t_0)\,\delta_c(\boldsymbol{x}'+\boldsymbol{x},t_0)\,\mathrm{d}^3\boldsymbol{X}'. \tag{22}$$

The generation of galaxies at time t proceeds as follows. We start with $I = 2$, calculate $\delta_c(\boldsymbol{x},t,I)$, and search for local maximums of $\delta_c(\boldsymbol{x},t,I)$ inside a comoving volume $L_x L_y L_z$. If a maximum exceeds 1.69 we generate a galaxy of radius

$$R(I) \approx \frac{\pi a_2}{k_I}, \tag{23}$$

and dark plus baryonic plus neutrino mass

$$M(I) \approx 2.69 \frac{4\pi R(I)^3}{3} \frac{\Omega_m \rho_c}{a_2^3} \tag{24}$$

if it "fits", *i.e.* if it does not overlap previously generated galaxies. I is increased by 1 unit to generate galaxies of a smaller generation, until $I = I_{\max}$ is reached. See **Figure 6**.

The peculiar velocity of the generated galaxies is

$$\boldsymbol{v}_{\text{pec}}(\boldsymbol{x},t) = \sum_{\boldsymbol{k},k<k_{I-1}} \frac{2i\boldsymbol{k}a_2^2|\delta_{\boldsymbol{k}}|}{3k^2 t} \exp\left[i\frac{\boldsymbol{k}\cdot\boldsymbol{x}}{a_2} + i\varphi_{\boldsymbol{k}}\right], \tag{25}$$

and their peculiar displacement is

$$\boldsymbol{x}_{\text{pec}} = \frac{3}{2}\boldsymbol{v}_{\text{pec}} t. \tag{26}$$

$\boldsymbol{x} + \boldsymbol{x}_{\text{pec}}$ is the proper coordinate of a galaxy at the time t of its generation, and $a_2 \equiv a_2(t)$. The comoving coordinate of this galaxy, *i.e.* its position extrapolated to the present time, is the corresponding $(\boldsymbol{x} + \boldsymbol{x}_{\text{pec}})/a_1(t)$. $\boldsymbol{x}_{\text{pec}}$ causes the difference between the data points $P_{\text{gal}}(k)$ in **Figure 3** and **Figure 4** at large k.

Note in **Figure 6** that the formation of galaxies is hierarchical: small galaxies form first, and, as time goes on, density perturbations grow, and groups of galaxies coalesce into larger galaxies in an ongoing process until dark energy dominates and the hierarchical formation of galaxies comes to an end. The distribution of galaxies of generation I depend only on $P(k)$ for $k < k_I$. Also,

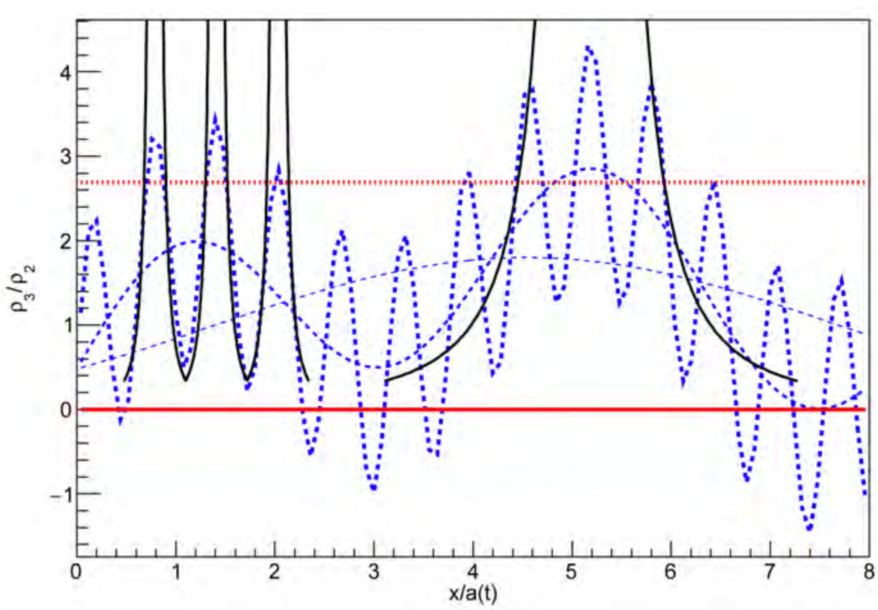

Figure 6. The hierarchical formation of galaxies [12]. Three Fourier components of the density in the linear approximation are shown. Note that in the linear approximation $\delta_c \equiv (\rho_3 - \rho_2)/\rho_2 \propto a(t)$. When δ_c reaches 1.69 in the linear approximation the exact solution diverges and a galaxy forms. As time goes on, density perturbations grow, and groups of galaxies of one generation coalesce into larger galaxies of a new generation as shown on the right.

luminous galaxies occupy a total volume (luminous plus dark) less than 1/2.69 of space.

Neutrinos with $0 < m_\nu < 1.17$ eV become non-relativistic after the densities of radiation and matter become equal, as illustrated in Figure 7.

3. Fluctuation Amplitude σ_8

σ_8 is the root-mean-square fluctuation of total mass relative to the mean in randomly placed volumes of radius $r_s = 8h^{-1}$ Mpc. We use a "gaussian window function"

$$W(r) = \frac{1}{V_W}\exp\left(-\frac{r^2}{2r_W^2}\right), \tag{27}$$

which smoothly defines a volume

$$V_W \equiv \frac{4}{3}\pi r_s^3 = (2\pi)^{3/2} r_W^3. \tag{28}$$

Note that

$$\int_0^\infty W(r) 4\pi r^2 \mathrm{d}r = 1. \tag{29}$$

The Fourier transform of $W(r)$ is

$$W(k) \equiv \int W(r) \mathrm{e}^{-i\boldsymbol{k}\cdot\boldsymbol{r}} \mathrm{d}^3 r = \exp\left(-k^2 r_W^2/2\right). \tag{30}$$

Then

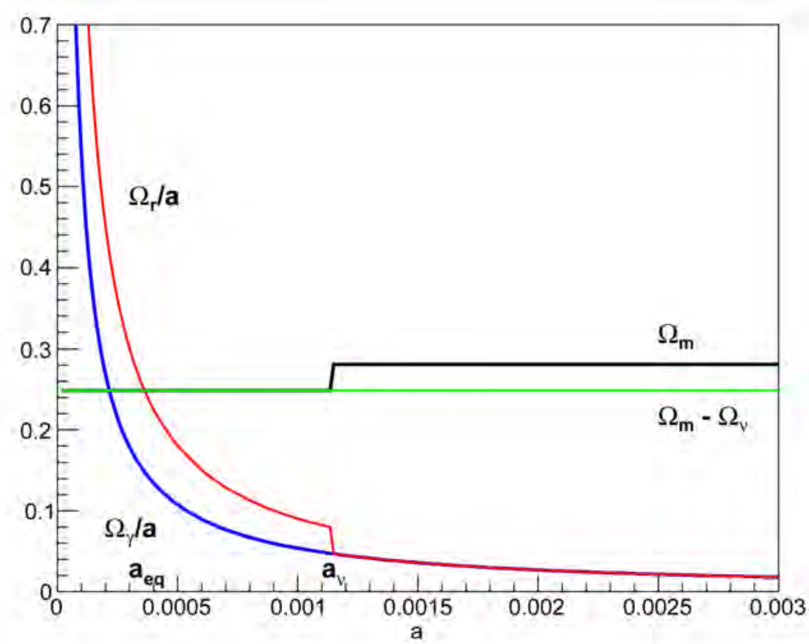

Figure 7. Example with $m_\nu = 0.46$ eV for each of 3 active neutrino eigenstates. Neutrinos become non-relativistic at $a_\nu \approx 0.00115$. The matter density relative to the critical density is $\Omega_m - \Omega_\nu$ for $a < a_\nu$, and Ω_m for $a > a_\nu$. The densities of matter and radiation become equal at $a_{\mathrm{eq}} = 0.00036$.

$$\sigma_8^2 = \frac{1}{(2\pi)^3}\int_0^\infty 4\pi k^2 \mathrm{d}k P(k)\exp\left(-k^2 r_W^2\right). \quad (31)$$

An alternative window function is the "top hat" function $f(r) = 3/\left(4\pi r_s^3\right)$ for $r < r_s$, and $f(r) = 0$ for $r > r_s$. Then

$$f(k) = \frac{3}{(kr_s)^3}\left(\sin(kr_s) - kr_s\cos(kr_s)\right). \quad (32)$$

Direct measurements obtain [3]

$$\sigma_8 = \left[0.813 \pm 0.013(\mathrm{stat}) \pm 0.024(\mathrm{syst})\right]\left(\Omega_m/0.25\right)^{-0.47}. \quad (33)$$

80% of σ_8^2 is due to k/h in the range 0.05 to 0.25 Mpc^{-1}. For comparison, from the 6-parameter ΛCDM fit [3], $\sigma_8 = 0.815 \pm 0.009$.

4. The Sachs-Wolfe Effect

The spherical harmonic expansion of the CMB temperature fluctuation is

$$\Delta T(\theta,\phi) \equiv T(\theta,\phi) - T_0 = \sum_{lm} a_{lm} Y_{lm}(\theta,\phi). \quad (34)$$

Averaging over m obtains $C_l \equiv \left\langle |a_{lm}|^2 \right\rangle$. The variable that is measured is [2]

$$\left\langle \Delta T(\hat{n}_1)\Delta T(\hat{n}_2)\right\rangle = \sum_l C_l \frac{2l+1}{4\pi} P_l(\hat{n}_1\cdot\hat{n}_2). \quad (35)$$

For $7 < l < 20$ the dominant contribution to C_l is from the Sachs-Wolfe effect [1] [2] [3]. This range corresponds to $0.0007\ \mathrm{Mpc}^{-1} < k/h < 0.002\ \mathrm{Mpc}^{-1}$. The Sachs-Wolfe effect relates temperature fluctuations of the CMB to perturbations of the gravitational potential ϕ [2]:

$$\left(\frac{\Delta T(\hat{n})}{T_0}\right)_{\mathrm{SW}} = \frac{1}{3}\delta\phi(\hat{n}). \quad (36)$$

When expressed as a function of comoving coordinates, $\delta\phi(\boldsymbol{X})$ is independent of time when matter dominates. The primordial power spectrum of gravitational potential fluctuations is assumed to have the form [2]

$$P_\phi(k) = N_\phi^2 k^{n-4}. \quad (37)$$

The relation between N_ϕ^2 and N^2 is $N_\phi^2 = 9N^2/25$ [2]. In the present analysis, unless otherwise stated, we assume the Harrison-Zel'dovich power spectrum with $n = 1$, which is close to observations [3]. For $7 \lesssim l \lesssim 20$, [2]

$$C_l = \frac{24\pi Q^2}{5l(l+1)}, \quad (38)$$

where the "quadrupole moment" Q is measured to be

$$Q = 18.0 \pm 1.4\ \mu\mathrm{K} \quad (39)$$

from the 1996 COBE results (see list of references in [2]). Then, for $P'(k)$,

$$\frac{A}{k_{\mathrm{eq}}} = \frac{1}{\Omega_m^2}\left(\frac{c}{H_0}\right)^4 \frac{12Q^2}{5\pi T_0^2} = (16 \pm 3)\times 10^4\ \mathrm{Mpc}^4, \quad (40)$$

and for $P''(k)$,

$$N^2 = \frac{15}{\pi}\frac{Q^2}{T_0^2} = (2.08 \pm 0.33) \times 10^{-10}, \tag{41}$$

independently of $\sum m_\nu$. Detailed integration obtains results within 10% for $5 < l < 18$.

5. Data and Simulations

The data are obtained from the publicly available SDSS DR14 catalog [5] [6], see acknowledgement. We consider objects classified as GALAXY, with redshift z in the range 0.4 to 0.6, with redshift error $\text{zErr} < 0.002$, passing quality selection flags. We further select galaxies in the northern galactic cap, in a "rectangular" volume with $L_x = 400$ Mpc along the line of sight (corresponding to redshift $z \approx 0.5 \pm 0.046$), $L_y = 3800$ Mpc (corresponding to an angle 86^0 across the sky), and $L_z = 1400$ Mpc (corresponding to an angle 32^0). In total 222470 galaxies pass these selections. The distributions of these galaxies are shown in Figure 8.

Unless otherwise specified, the simulations have $L_x = L_y = L_z = 700$ Mpc, $I_{\max} = 59$, $h = 0.678$, $\Omega_\Lambda = 0.719$, $\Omega_m = 0.281$, $\Omega_k = 0$, and the input power spectrum of density fluctuations is (5) with $A = 9200$ Mpc^3, $k_{eq}/h = 0.067$ Mpc^{-1}, $\eta = 4.7$, and $\sum m_\nu = 0$ eV. We generate galaxies at redshift $z = a_1^{-1} - 1 = 0.5$, corresponding to $t = 8.9$ Gyr, and $a_2(t) = 0.62$. This reference simulation has 34,444 galaxies, which is near the limit we can generate with available computing resources.

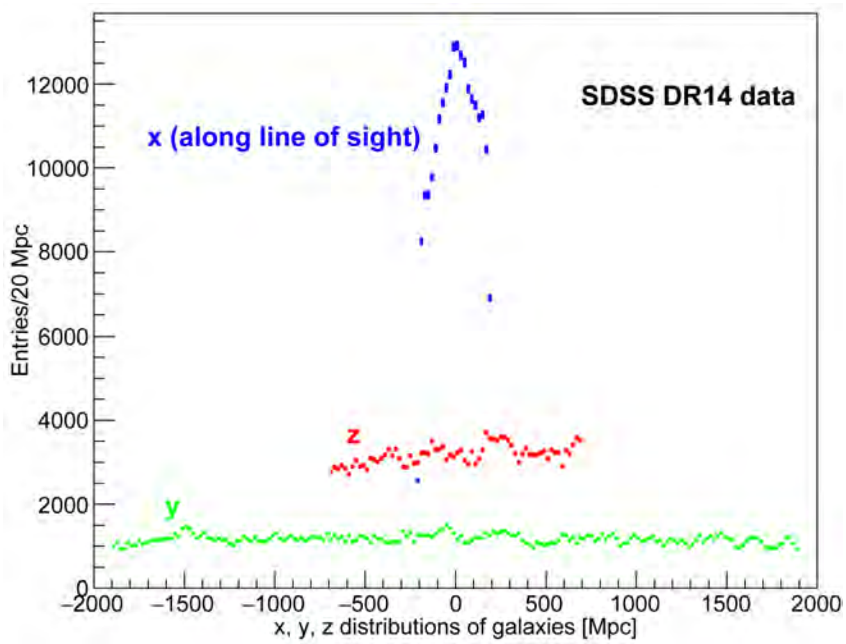

Figure 8. Distributions of 222470 SDSS DR14 galaxies in a "rectangular" box of dimensions $L_x = 400$ Mpc along the line of sight (corresponding to redshift $z = 0.5 \pm 0.046$), $L_y = 3800$ Mpc (corresponding to an angle 86^0 across the sky), and $L_z = 1400$ Mpc (corresponding to an angle 32^0).

Some definitions are in order. For data we define the absolute red magnitude of a galaxy MAGr at redshift z as the SDSS DR14 variable -modelMag_r corrected to the reference redshift 0.35. Similarly, we define the absolute green magnitude of a galaxy MAGg at redshift z as the SDSS DR14 variable -modelMag_g corrected to the reference redshift 0.35. For a simulated galaxy we define the absolute magnitude MAG $\equiv -19 + 2.5\log_{10}\left(M/10^{16} M_{\odot}\right)$, where M is defined by Equation (24). Note that MAGr and MAGg are derived from observed luminosities, while MAG is derived from the total (baryonic plus dark plus neutrino) mass of the simulation. These quantities can only be compared if the luminosity-to-mass ratio is known.

The number of galaxies per unit volume depends on the limiting magnitude of the survey, or on $I_{\max}$ of the simulation.

6. Distributions of Galaxies in SDSS DR14 Data and in Simulation

We would like to obtain $P(k)$ from Equation (19) and Equation (20). Unfortunately we do not have access to the relative density fluctuation $\delta_c(\boldsymbol{x}, t)$. Instead we have access to the positions of galaxies and their luminosities. The relation between luminosity and mass of galaxies depends on many variables and is largely unknown, so we focus on the information contained in the positions of galaxies.

Let

$$n(\boldsymbol{X}) = \bar{n}\left(1 + \sum_{\boldsymbol{k}'} \Delta_{\boldsymbol{k}'} \mathrm{e}^{i\boldsymbol{k}'\cdot\boldsymbol{X}}\right) \tag{42}$$

be the number density of point galaxies at redshift z as a function of the comoving coordinate $\boldsymbol{X} \equiv \boldsymbol{x}(t)/a(t)$. We have applied periodic boundary conditions in a comoving volume $V = L_x L_y L_z$, so $\boldsymbol{k}'$ has the discrete values of Equation (17). $n(\boldsymbol{X})$ is real, so $\Delta_{-\boldsymbol{k}'} = \Delta^*_{\boldsymbol{k}'}$. The number of galaxies in V is $N_{\text{gal}} = \bar{n}V$. To invert Equation (42), we multiply it by $\exp(-i\boldsymbol{k}\cdot\boldsymbol{X})$, integrate over V, and obtain a sum over galaxies j:

$$\sum_j e^{-i\boldsymbol{k}\cdot\boldsymbol{X}_j} = N_{gal}\Delta_{\boldsymbol{k}} + N_{gal}^{1/2} e^{i\varphi}. \tag{43}$$

The first term on the right hand side of Equation (43) is the result of a coherent sum of $N_{\boldsymbol{k}} \equiv N_{\text{gal}}\Delta_{\boldsymbol{k}}$ terms corresponding to mode $\boldsymbol{k}$. The second term is the result of an incoherent sum which we have approximated to $N_{\text{gal}}^{1/2}\mathrm{e}^{i\phi}$, where the phase ϕ is arbitrary. We define the "galaxy power spectrum"

$$P_{\text{gal}}(\boldsymbol{k}) \equiv V\left|\Delta_{\boldsymbol{k}}\right|^2, \tag{44}$$

and obtain

$$P_{\text{gal}}(\boldsymbol{k}) = V\left|\frac{1}{N_{\text{gal}}}\sum_j \mathrm{e}^{-i\boldsymbol{k}\cdot\boldsymbol{X}_j}\right|^2 - \frac{V}{N_{\text{gal}}} \pm \sqrt{\frac{2V}{N_{\text{gal}}}} P_{\text{gal}}(k). \tag{45}$$

The transition between signal and noise occurs at

$\log_{10}\left(P_{\text{gal}}(k)/h^{-3}\,\text{Mpc}^3\right) \approx 3.47$ for our data sample, and ≈3.49 for our reference simulation. To test these ideas we can select a narrow range of MAGr, MAGg, or MAG to shift the noise upwards, compare Figures 9-11 (which plot the first term on the right hand side of Equation (45) and include the noise at large *k*).

Averaging over $\boldsymbol{k}$ in a bin of $k \equiv |\boldsymbol{k}|$ obtains $P_{\text{gal}}(k)$. The factor *V* is inserted so that $P_{\text{gal}}(k)$ becomes independent of the arbitrary choice of *V* for large *V*. The function $P_{\text{gal}}(k)$ defines statistically the distribution of galaxies. The variables $\boldsymbol{k}$ in Equation (16) and Equation (45) should not be confused: there is not necessarily a one-to-one relation between them.

Results for data are presented in Figures 9-11. We note that the galaxy bias *b* depends on MAGr and MAGg. Even tho $N_{\text{gal}} \gg N_{\boldsymbol{k}}$, $N_{\boldsymbol{k}} > N_{\text{gal}}^{1/2}$ at small *k*. For this reason $P_{\text{gal}}(k)$ in Figure 9 extends to higher *k* than in Figure 10 and Figure 11 before saturating with noise. Figure 12 presents the noise subtracted galaxy power spectrum $P_{\text{gal}}(k)$, obtained from Figure 9, compared with $P(k)$ calculated with the indicated parameters. Their ratio is the bias b^2.

Results for the simulations are presented in Figures 13-15. In Figure 15 we compare the reference simulation with $P'(k)$, with simulations with $P'(k)\cdot\left(-\log_{10}\left(k/h\,\text{Mpc}^{-1}\right)\right)$ ("steeper slope"), or $P'(k)/\left(-\log_{10}\left(k/h\,\text{Mpc}^{-1}\right)\right)$ ("less slope"). Note that the function $-\log_{10}\left(k/h\,\text{Mpc}^{-1}\right)$ varies between ≈1.3 to ≈0.5 in the region of interest. We observe, qualitatively, that the slope of $P(k)$ has a larger effect on $P_{\text{gal}}(k)$ than the amplitude *A*. A comparison of the

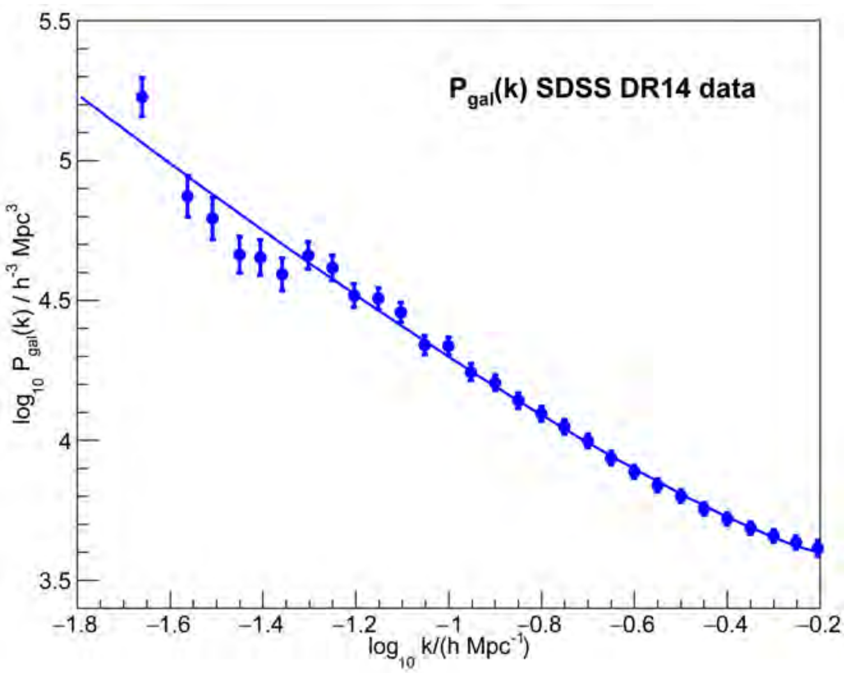

Figure 9. Galaxy power spectrum (plus noise visible at large *k*) from SDSS DR14 data in a volume $V = 400\times3800\times1400\ \text{Mpc}^3$, at redshift $z = 0.5\pm0.0457$. The fit is $y = 3.60 + 0.92\cdot(0.2 - x)^{1.23}$ with $\chi^2 = 26.8$ for 29 degrees of freedom, where *x* and *y* are the axis in this figure.

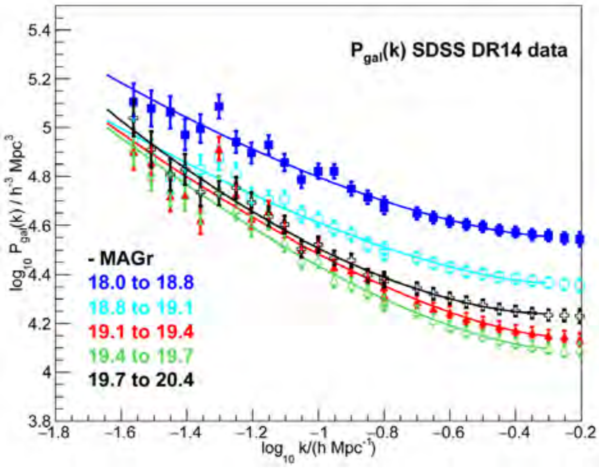

Figure 10. Galaxy power spectrum (plus noise visible at large *k*) in bins of MAGr from SDSS DR14 galaxies with redshift $z = 0.5 \pm 0.0457$.

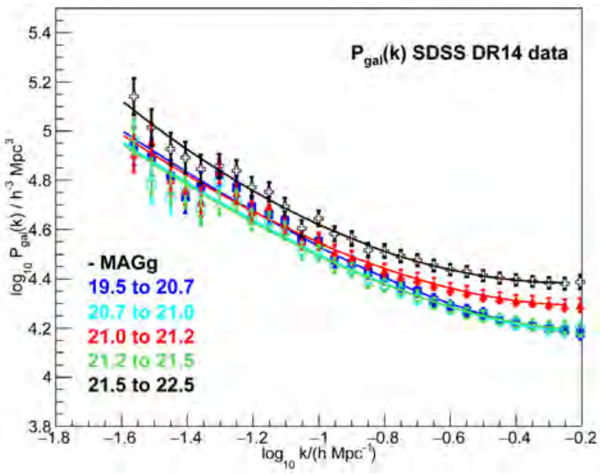

Figure 11. Galaxy power spectrum (plus noise visible at large *k*) in bins of MAGg from SDSS DR14 galaxies with redshift $z = 0.5 \pm 0.0457$.

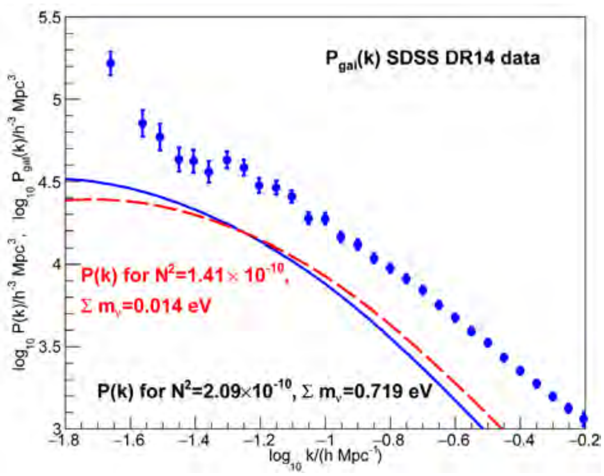

Figure 12. Noise subtracted galaxy power spectrum $P_{gal}(k)$, obtained from **Figure 9**, compared with $P(k)$ calculated with the indicated parameters. Their ratio is b^2.

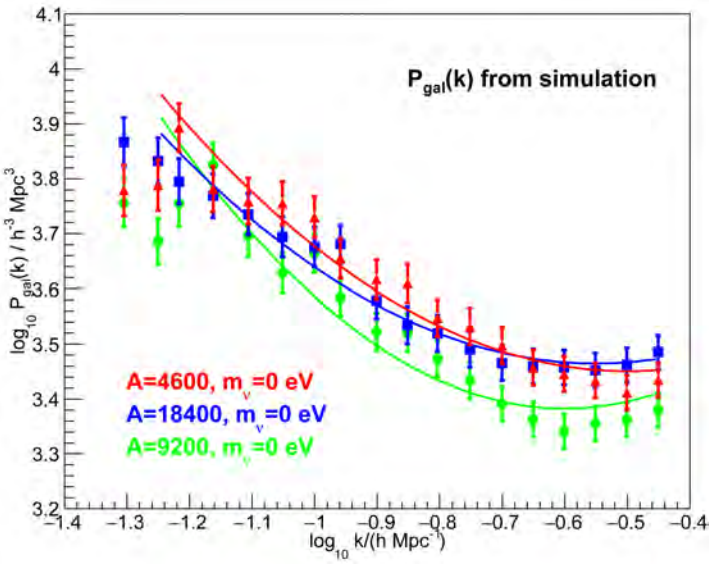

Figure 13. Galaxy power spectrum (plus noise visible at large k) from simulations with three amplitudes A. All other parameters of the simulation are given in Section 5.

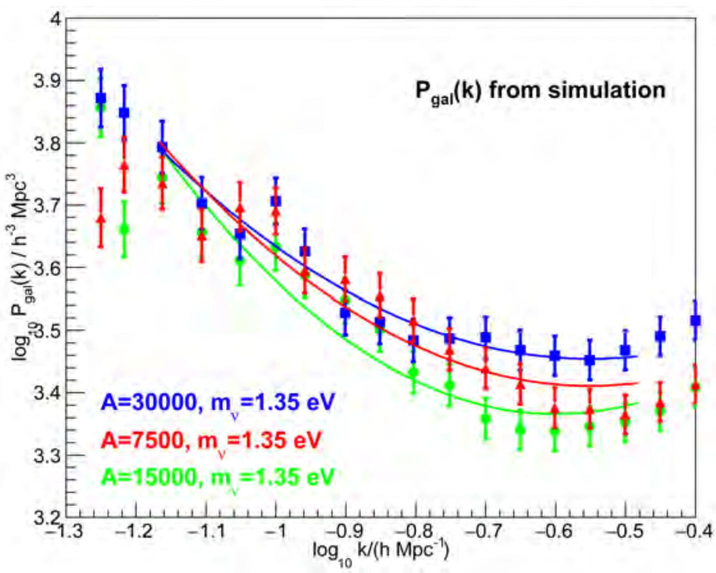

Figure 14. Galaxy power spectrum (plus noise visible at large k) from simulations with $\sum m_\nu = 1.35$ eV, with three amplitudes A. Other parameters are $\eta = 4.4$, and $k_{eq}/h = 0.14\ \text{Mpc}^{-1}$.

simulations in Figure 15 with $P_{gal}(k)$ from data in Figure 9 favors a power spectrum $P(k)$ "steeper" than in the reference simulation. The reference simulation has parameters of $P(k)$ similar to the ones obtained from the fit in Figure 1 which assumes scale invariant b, and $\sum m_\nu = 0$ eV. The reference simulation is also similar to the fit "$\sum m_\nu = 0.014$ eV" in Figure 12 (taken from Figure 3 which assumes scale invariant b). A steeper $P(k)$ implies $\sum m_\nu > 0$ as shown in Figure 12 by the curve "$\sum m_\nu = 0.719$ eV", and corresponds to a bias b with positive slope as in Equation (55) below.

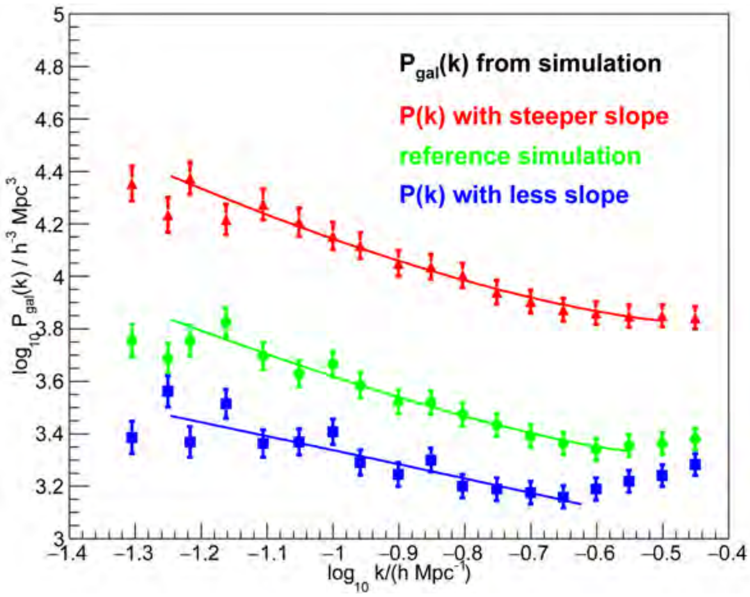

Figure 15. Galaxy power spectrum (plus noise visible at large k) of the reference simulation, a simulation with $P(k)$ with steeper slope ($P(k)$ of Equation (1) is multiplied by $-\log_{10} k/(h\ \text{Mpc}^{-1})$), and a simulation with less slope ($P(k)$ of Equation (1) is divided by $-\log_{10} k/(h\ \text{Mpc}^{-1})$).

7. Luminosity and Mass Distributions of Galaxies

Distributions of MAGr and MAGg from data, and MAG from several simulations are presented in Figure 16 and Figure 17. From these figures it is possible to obtain the "mean" luminosity-to-mass ratios. We note that these figures do not show useful sensitivity to $\sum m_\nu$.

8. Test of Scale Invariance of the Galaxy Bias *b*

In this Section we test the scale invariance of the bias b defined in Equation (11). To do so, we count galaxies in an array of $N_s = N_x \times N_y$ spheres of radii r_s, and obtain their mean $\bar{N}$, and their root-mean-square (rms). All spheres have their center at redshift $z = 0.5$ to ensure the homogeneity of the galaxy selections. The results for $r_s = 8/h, 16/h, 32/h, 64/h, 128/h$, and $256/h$ Mpc are presented in Table 1. The (rms)^2 has a contribution σ^2 from $P(k)$, and a contribution $\bar{N}$ from statistical fluctuations:

$$\sigma^2 = \text{rms}^2 - \bar{N} \pm 2\sigma\sqrt{\frac{\bar{N}}{N_s}}. \tag{46}$$

We compare $\sigma/\bar{N}$ obtained from galaxy counts, with the relative mass fluctuations σ_{hr_s} obtained from Equation (6) and Equation (31). The ratio of these two quantities divided by a correction factor

$$C\left(\Omega_\Lambda \big/ \left(\Omega_m (1+z)^3\right)\right) \Big/ \left(C(\Omega_\Lambda/\Omega_m)(1+z)\right) = 0.779$$

[2] is the bias b.

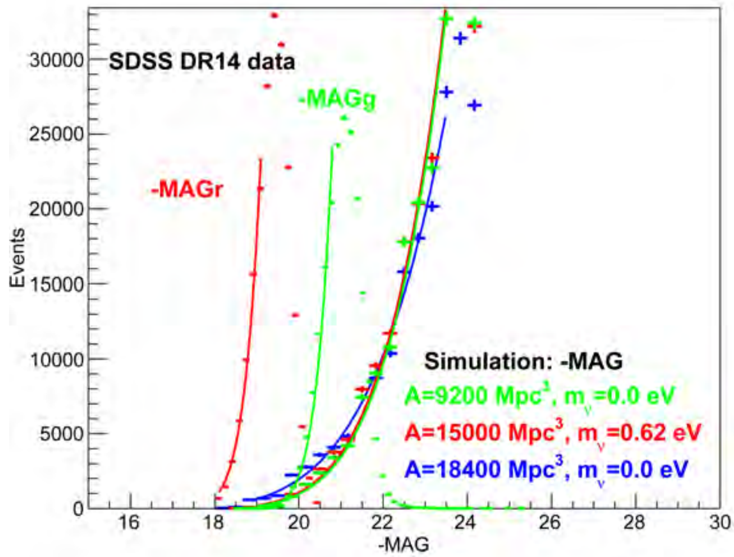

Figure 16. Distributions of MAGr and MAGg of SDSS DR14 data, and distributions of MAG of several simulations (see definitions in Section 5). The difference between the MAGr or MAGg of data and MAG of simulations determines the "mean" galaxy L/M ratio.

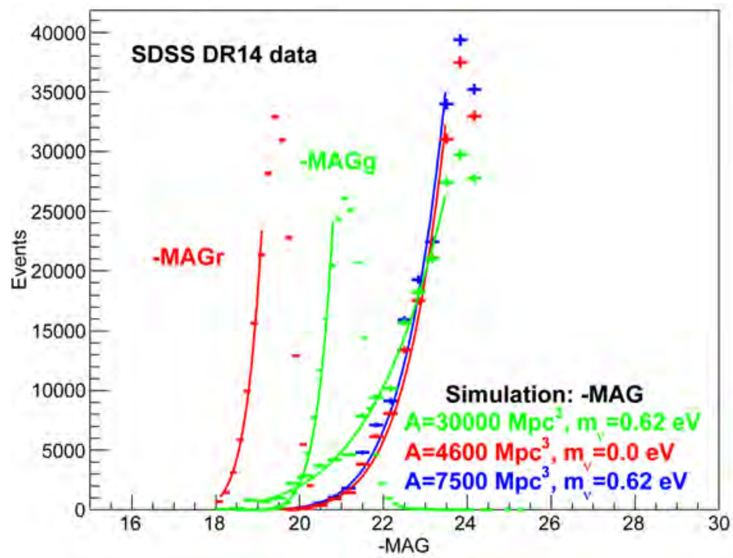

Figure 17. Same as **Figure 16** with additional simulations.

The measured bias b is a function of r_s, $\sum m_\nu$, h and the spectral index n. Results for $h = 0.678$ and $n = 1$ are presented in **Table 1**. The last column is the χ^2 of the five b's of spheres with $\bar{N} > 1$, assuming these b's are scale invariant with respect to their weighted average. Additional measurements of χ^2 are presented in **Figure 18**. Assuming that b is scale invariant we obtain

$$\sum m_\nu = 0.939 + 0.035 \cdot \delta h + 0.089 \cdot \delta n \pm 0.008 \text{ eV}, \tag{47}$$

with minimum $\chi^2 = 3.2$ for four degrees of freedom. We have defined $\delta h \equiv (h - 0.678)/0.009$, and $\delta n \equiv (n-1)/0.038$.

Table 1. Mean galaxy counts $\bar{N}$ in spheres of radius r_s. All spheres have their center at redshift $z = 0.5$. The number of spheres is $N_s = N_y \times N_z$. Note that the observed root-mean-square (rms) fluctuation relative to the mean $\bar{N}$ is larger than the corresponding statistical fluctuation, *i.e.* $\text{rms}/\bar{N} > 1/\sqrt{\bar{N}}$. σ_{hr_s} is calculated with Equation (6) and Equation (31) with N^2 chosen so $\sigma_8 = 0.770$ to set the scale for b (e.g. $N^2 = 0.8472 \times 10^{-10}$ for $\sum m_\nu = 0$ eV, or $N^2 = 1.3575 \times 10^{-10}$ for $\sum m_\nu = 0.6$ eV). Both the galaxy counts and σ_{hr_s} are obtained with the top-hat window function. The true standard deviation is obtained from $\sigma^2 = \text{rms}^2 - \bar{N} \pm 2\sigma\sqrt{\bar{N}/N_s}$. The measured "bias" is defined as $b \equiv (\sigma/\bar{N})/(0.779 \cdot \sigma_{hr_s})$. The last column is the χ^2 of the five b's of spheres with $\bar{N} > 1$, assuming these b's are scale invariant. $h = 0.678$, $n = 1.0$, and $\Omega_m = 0.281$.

hr_s [Mpc]	8	16	32	64	128	256	
r_s [Mpc]	11.80	23.60	47.20	94.40	188.79	377.58	
$N_y \times N_z$	151×55	75×27	37×13	19×7	9×3	4×1	
$\bar{N}$	0.836	6.781	52.279	410.74	3092.3	21810.0	
$1/\sqrt{\bar{N}}$	1.0935	0.3840	0.1383	0.0493	0.0180	0.0068	
$\text{rms}/\bar{N}$	1.798	0.873	0.443	0.210	0.0870	0.0346	
$\sigma/\bar{N}$	1.427 ± 0.012	0.784 ± 0.009	0.421 ± 0.006	0.204 ± 0.004	0.085 ± 0.003	0.034 ± 0.003	
$\sigma_{hr_s}, \sum m_\nu = 0.0$ eV	0.7700	0.4457	0.2255	0.0987	0.0374	0.0124	χ^2
$b, \sum m_\nu = 0.0$ eV	2.380 ± 0.020	2.257 ± 0.025	2.398 ± 0.036	2.650 ± 0.056	2.925 ± 0.119	3.503 ± 0.349	79.2
$\sigma_{hr_s}, \sum m_\nu = 0.3$ eV	0.7700	0.4514	0.2321	0.1036	0.0402	0.0136	
$b, \sum m_\nu = 0.3$ eV	2.380 ± 0.020	2.228 ± 0.024	2.329 ± 0.035	2.523 ± 0.053	2.722 ± 0.111	3.193 ± 0.318	49.5
$\sigma_{hr_s}, \sum m_\nu = 0.6$ eV	0.7700	0.4603	0.2425	0.1113	0.0443	0.0152	
$b, \sum m_\nu = 0.6$ eV	2.380 ± 0.020	2.185 ± 0.024	2.230 ± 0.033	2.350 ± 0.049	2.468 ± 0.100	2.862 ± 0.285	20.0
$\sigma_{hr_s}, \sum m_\nu = 0.7$ eV	0.7700	0.4640	0.2468	0.1144	0.0460	0.0158	
$b, \sum m_\nu = 0.7$ eV	2.380 ± 0.020	2.168 ± 0.024	2.191 ± 0.033	2.285 ± 0.048	2.379 ± 0.097	2.755 ± 0.275	12.6
$\sigma_{hr_s}, \sum m_\nu = 0.8$ eV	0.7700	0.4682	0.2516	0.1179	0.0478	0.0165	
$b, \sum m_\nu = 0.8$ eV	2.380 ± 0.020	2.148 ± 0.023	2.149 ± 0.032	2.218 ± 0.047	2.289 ± 0.093	2.648 ± 0.264	7.1
$\sigma_{hr_s}, \sum m_\nu = 0.9$ eV	0.7700	0.4729	0.2570	0.1218	0.0497	0.0171	
$b, \sum m_\nu = 0.9$ eV	2.380 ± 0.020	2.127 ± 0.023	2.104 ± 0.032	2.147 ± 0.045	2.198 ± 0.089	2.541 ± 0.253	4.0
$\sigma_{hr_s}, \sum m_\nu = 1.0$ eV	0.7700	0.4782	0.2630	0.1261	0.0519	0.0179	
$b, \sum m_\nu = 1.0$ eV	2.380 ± 0.020	2.103 ± 0.023	2.056 ± 0.031	2.073 ± 0.044	2.107 ± 0.086	2.434 ± 0.243	3.8
$\sigma_{hr_s}, \sum m_\nu = 1.2$ eV	0.7700	0.4911	0.2775	0.1363	0.0568	0.0196	
$b, \sum m_\nu = 1.2$ eV	2.380 ± 0.020	2.048 ± 0.022	1.948 ± 0.029	1.919 ± 0.040	1.923 ± 0.078	2.220 ± 0.221	13.7

In conclusion, the galaxy bias b is scale invariant within the statistical uncertainties of b presented in Table 1, provided $\sum m_\nu$ satisfies Equation (47), else scale invariance is broken. Note in Table 1 that the variation of b with scale depends on $\sum m_\nu$.

9. Measurement of Neutrino Masses with the Sachs-Wolfe Effect and σ_8

We return to the measurement of neutrino masses. Since the galaxy bias b may be scale dependent, in this Section we exclude measurements of $P_{\text{gal}}(k)$ with galaxies.

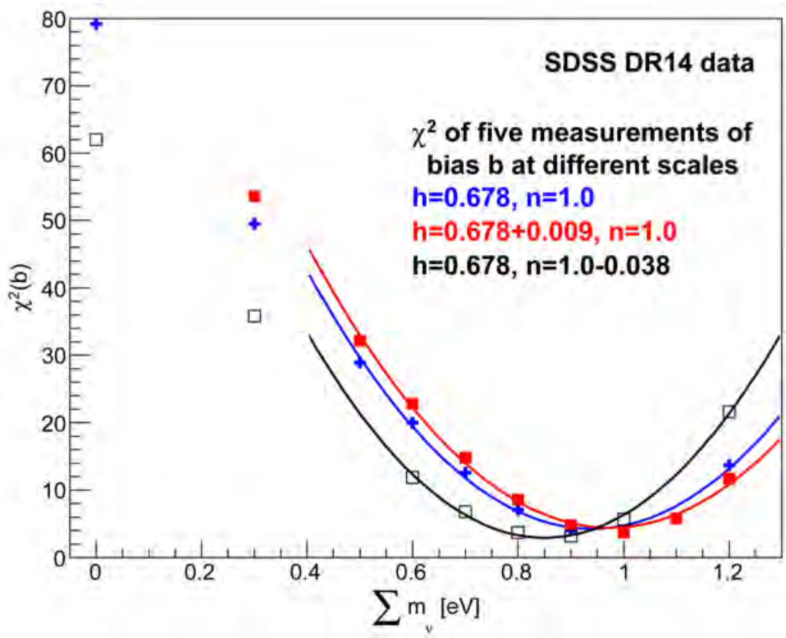

Figure 18. χ^2 of five measurements of bias b assumed to be scale invariant with respect to their weighted mean as a function of $\sum m_\nu$, for several values of the Hubble parameter h, and the spectral index n. The five measurements of b correspond to scales $r_s = 16/h, 32/h, 64/h, 128/h$, and $256/h$ Mpc.

The ΛCDM model is described by Equation (6) that has three free parameters: N^2, n, and $\sum m_\nu$. We keep n fixed. We vary the two parameters N^2 and $\sum m_\nu$ to minimize a χ^2 with two terms corresponding to two observables: the Sachs-Wolfe effect (N^2 from Equation (41)), and σ_8 given by Equation (33). We therefore have zero degrees of freedom. The result is a function of h, Ω_m, and the spectral index n, so we define $\delta h \equiv (h - 0.678)/0.009$ [3], $\delta\Omega_m \equiv (\Omega_m - 0.281)/0.003$ [7], and $\delta n \equiv (n-1)/0.038$ [3], and obtain

$$\sum m_\nu = 0.595 + 0.047 \cdot \delta h + 0.226 \cdot \delta n + 0.022 \cdot \delta\Omega_m \pm 0.225(\text{stat})^{+0.484}_{-0.152}(\text{syst})\,\text{eV}. \quad (48)$$

Note that in the "6 parameter ΛCDM fit" [3], which assumes $\sum m_\nu = 0.06$ eV, $n = 0.968 \pm 0.006$. Here, and below, the systematic uncertainties are obtained by repeating the fits with the top-hat window function instead of the gaussian window function for σ_8 (and for $\sigma/\bar{N}$ if applicable), and also with $\sigma_8 = 0.815 \pm 0.009$ obtained with the "6 parameter ΛCDM fit" [3], instead of σ_8 from direct measurements, Equation (33).

The fit of Equation (48) is compared with measurements of $P_{\text{gal}}(k)$ obtained from the SDSS-III BOSS survey [4] in **Figure 19**. It is interesting to note that the discrepancy, *i.e.* the drop of $P(k)$ in the range $-1.6 < \log_{10}(k/h\,\text{Mpc}) < -1.3$, is also observed in **Figure 12**.

For comparison, reference [8] obtains $\Omega_m = 0.282 \pm 0.003$ and

$$\sum m_\nu = 0.711 - 0.335 \cdot \delta h + 0.050 \cdot \delta b \pm 0.063\,\text{eV}, \quad (49)$$

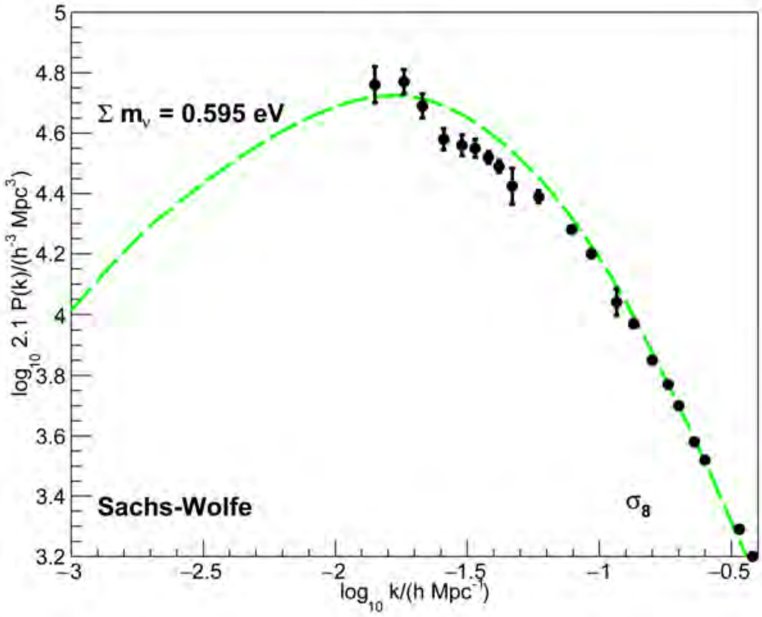

Figure 19. Comparison of $P_{gal}(k)$ obtained from the SDSS-III BOSS survey [4] ("reconstructed") with $b^2P(k)$ obtained from a fit of Equation (6) to the Sachs-Wolfe effect and σ_8 only. The fit obtains $\sum m_\nu = 0.595 \pm 0.225$ eV with zero degrees of freedom. $h = 0.678$ and $n = 1.0$ are fixed.

where $\delta b \equiv \left(\Omega_b h^2 - 0.02226\right)/0.00023$, from a study of BAO with SDSS DR13 galaxies. We allow $\Omega_b h^2$ to vary by one standard deviation, *i.e.* $\delta b = 0 \pm 1$ [7]. To combine the independent measurements (48) and (49) we add one more term to the χ^2 corresponding to the measurement (49), so we now have one degree of freedom. We obtain

$$\sum m_\nu = 0.696 - 0.281 \cdot \delta h + 0.032 \cdot \delta n + 0.003 \cdot \delta\Omega_m \\ \pm 0.075(\text{stat})^{+0.055}_{-0.029}(\text{syst})\,\text{eV}, \tag{50}$$

with $\chi^2 = 0.25$ for one degree of freedom, so the two independent measurements of $\sum m_\nu$, Equation (48) and Equation (49), are consistent. Note that the uncertainty of h dominates the uncertainty of $\sum m_\nu$ in Equation (50).

We now free h and add one term to the χ^2 corresponding to $h = 0.0678 \pm 0.009$ [3], and obtain

$$\sum m_\nu = 0.633 \pm 0.168(\text{stat})^{+0.064}_{-0.043}(\text{syst})\,\text{eV}, \tag{51}$$

$$h = 0.680 \pm 0.005(\text{stat}), \tag{52}$$

with $\chi^2 = 0.07$ for one degree of freedom. The systematic uncertainties in Equation (51) now include δn. The 1σ, 2σ, and 3σ contours are presented in **Figure 20**.

If instead we set $h = 0.72 \pm 0.03$ from the direct measurement of the Hubble expansion rate [3], we obtain

$$\sum m_\nu = 0.563 \pm 0.207(\text{stat})^{+0.064}_{-0.043}(\text{syst})\,\text{eV}, \tag{53}$$

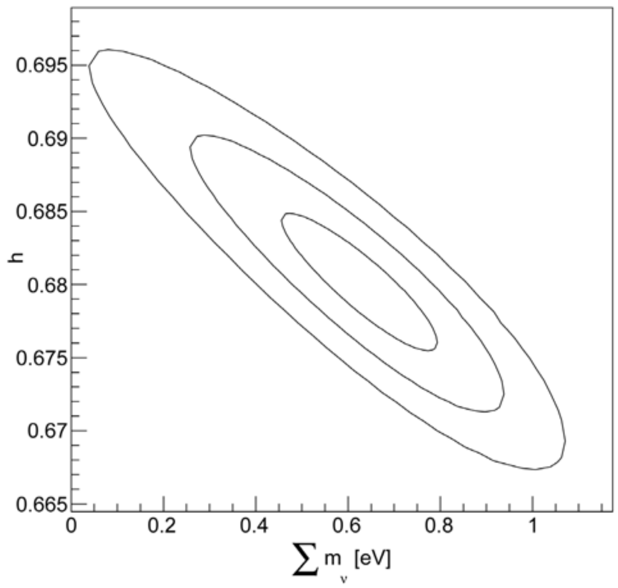

Figure 20. Contours corresponding to 1, 2, and 3 standard deviations in the $\left(\sum m_\nu, h\right)$ plane, from Sachs-Wolfe, σ_8, $h = 0.678 \pm 0.009$, and BAO measurements. Points on the contours have $\chi^2 - \chi^2_{\min} = 1, 4$, and 9, respectively, where χ^2 has been minimized with respect to N^2. The total uncertainty of $\sum m_\nu$ is dominated by the uncertainty of h. In this figure $n = 1$, and the systematic uncertainties, presented in Equation (51), are not included.

$$h = 0.682 \pm 0.006(\text{stat}), \tag{54}$$

with $\chi^2 = 1.7$ for 1 degree of freedom. The corresponding 1σ, 2σ, and 3σ contours are presented in Figure 21. Note that the fitted h does not change significantly.

10. Measurement of Neutrino Masses with the Sachs-Wolfe Effect, σ_8, and $P_{\text{gal}}(k)$

We repeat the fit of Figure 3, which includes the "reconstructed" SDSS-III BOSS $P_{\text{gal}}(k)$ measurements [4], but this time we allow the galaxy bias b to depend on scale: $b \equiv b_0 + b_1 \log_{10}\left(k/h\ \text{Mpc}^{-1}\right)$. Minimizing the χ^2 with respect to $\sum m_\nu$, N^2, n, $h = 0.678 \pm 0.009$, b_0, and b_1, we obtain

$$\begin{gathered}\sum m_\nu = 0.80 \pm 0.23\ \text{eV}, \\ N^2 = (1.88 \pm 0.39) \times 10^{-10}, \\ n = 1.064 \pm 0.068, \\ h = 0.676 \pm 0.011, \\ b_0 = 2.35 \pm 0.36, \\ b_1 = 0.229 \pm 0.094,\end{gathered} \tag{55}$$

with $\chi^2 = 27.8$ for 18 degrees of freedom. The uncertainties have been multiplied by $\sqrt{27.8/18}$. Confidence contours are presented in Figure 22. Fixing

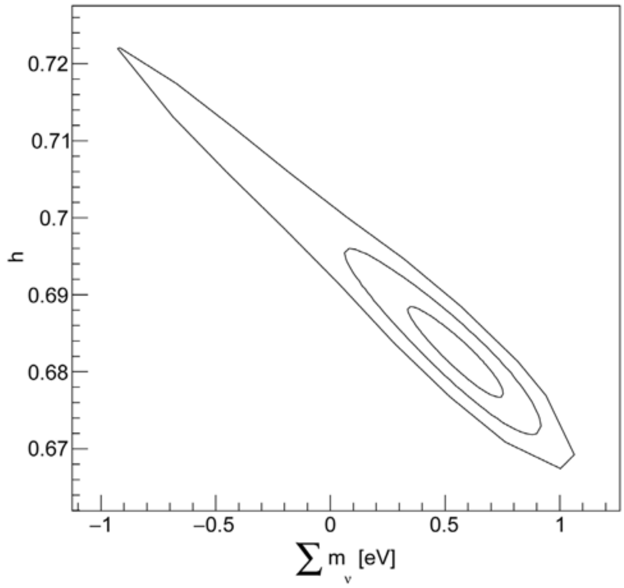

Figure 21. Same as **Figure 20** but $h = 0.72 \pm 0.03$.

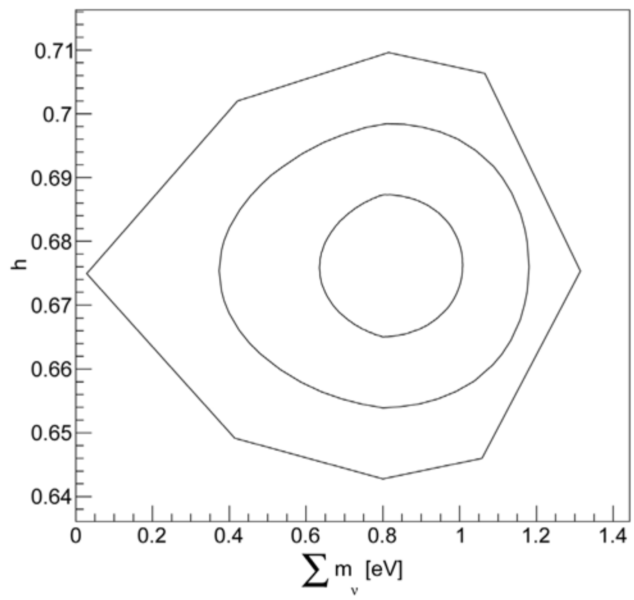

Figure 22. Contours corresponding to 1, 2, and 3 standard deviations in the $\left(\sum m_\nu, h\right)$ plane, from Sachs-Wolfe, σ_8, $h = 0.678 \pm 0.009$, and $P_{gal}(k)$ measurements. Points on the contours have $\chi^2 - \chi^2_{min} = 1, 4$, and 9, respectively, where χ^2 has been minimized with respect to N^2, n, b_0, and b_1.

$b_1 = 0$ obtains $\chi^2 = 36.3$, so including the scale dependence of b is necessary.

11. Measurement of Neutrino Masses with the Sachs-Wolfe Effect, σ_8, and Galaxy Fluctuations

We repeat the measurements of $\sum m_\nu$ of Section 9 but add 4 more experimental constraints: $\sigma / \bar{N}$ of galaxy counts in spheres of radius

$r_s = 16/h, 32/h, 64/h$, and $128/h$ Mpc, which are listed in **Table 1**. Spheres of radius $8/h$ Mpc were not considered because they have $\bar{N} < 1$. Spheres of radius $256/h$ Mpc were excluded because there are only 4 spheres of this radius, and the difference between the rms for the top-hat and gaussian window functions turns out to be large (while consistent results are obtained for the other radii). We add two more parameters to be fit: b_0 and b_s which define the bias $b = b_0 - i_s b_s$, with $i_s = 0,1,2,3$ for $r_s = 16/h, 32/h, 64/h$, and $128/h$ Mpc, respectively. Note that we do not obtain a good fit with fixed bias $b = b_0$, and so have introduced a "bias slope" b_s.

From the Sachs-Wolfe effect, σ_8, and the $4\ \sigma/\bar{N}$ measurements we obtain

$$\begin{aligned}\sum m_\nu &= 0.618 + 0.042 \cdot \delta h + 0.206 \cdot \delta n + 0.019 \cdot \delta\Omega_m \\ &\pm 0.209(\text{stat})^{+0.420}_{-0.139}(\text{syst})\,\text{eV},\end{aligned} \tag{56}$$

with $\chi^2 = 1.10$ for 2 degrees of freedom. The variables that minimize the χ^2 are $\sum m_\nu$, N^2, b_0, and b_s. This result may be compared with (48).

Freeing $h = 0.678 \pm 0.009$, and keeping $n = 1.0$ fixed, we obtain

$$\begin{aligned}\sum m_\nu &= 0.618 \pm 0.214\,\text{eV}, \\ N^2 &= (2.11 \pm 0.31) \times 10^{-10}, \\ h &= 0.678 \pm 0.009, \\ b_0 &= 1.756 \pm 0.057, \\ b_s &= -0.062 \pm 0.042,\end{aligned} \tag{57}$$

with $\chi^2 = 1.10$ for 2 degrees of freedom.

Combining with the BAO measurement (49) we obtain

$$\begin{aligned}\sum m_\nu &= 0.697 - 0.276 \cdot \delta h + 0.032 \cdot \delta n + 0.003 \cdot \delta\Omega_m \\ &\pm 0.075(\text{stat})^{+0.055}_{-0.028}(\text{syst})\,\text{eV},\end{aligned} \tag{58}$$

with $\chi^2 = 1.29$ for 3 degrees of freedom. The variables that minimize the χ^2 are $\sum m_\nu$, N^2, b_0, and b_s. Freeing $h = 0.678 \pm 0.009$, and keeping $n = 1.0$ fixed, we obtain

$$\begin{aligned}\sum m_\nu &= 0.644 \pm 0.162\,\text{eV}, \\ N^2 &= (2.13 \pm 0.28) \times 10^{-10}, \\ h &= 0.680 \pm 0.005, \\ b_0 &= 1.756 \pm 0.057, \\ b_s &= -0.058 \pm 0.036,\end{aligned} \tag{59}$$

with $\chi^2 = 1.14$ for 3 degrees of freedom.

Finally, freeing n, and minimizing the χ^2 with respect to $\sum m_\nu$, N^2, n, $h = 0.678 \pm 0.009$, b_0, and b_s, we obtain

$$\sum m_\nu = 0.719 \pm 0.312(\text{stat})^{+0.055}_{-0.028}(\text{syst})\,\text{eV},$$

$$N^2 = (2.09 \pm 0.33) \times 10^{-10},$$
$$n = 1.021 \pm 0.075,$$
$$h = 0.678 \pm 0.008,$$
$$b_0 = 1.751 \pm 0.060,$$
$$b_s = -0.053 \pm 0.041, \tag{60}$$

with $\chi^2 = 1.1$ for 2 degrees of freedom. The parameter correlation coefficients, defined in [3], are

	$\sum m_\nu$	N^2	n	h	b_0	b_s
$\sum m_\nu$	1.000	−0.019	0.856	−0.966	−0.226	0.779
N^2	−0.019	1.000	−0.491	0.018	−0.155	0.428
n	0.856	−0.491	1.000	−0.834	−0.303	0.427
h	−0.966	0.018	−0.834	1.000	0.219	−0.755
b_0	−0.226	−0.155	−0.303	0.219	1.000	−0.037
b_s	0.779	0.428	0.427	−0.755	−0.037	1.000

Note that we have measured the amplitude N^2 and spectral index n of $P(k)$, and the bias b_0 including its slope b_s for the SDSS DR14 galaxy selections at redshift $z = 0.5$. 1, 2, 3, and 4 standard deviation contours are presented in **Figure 23**.

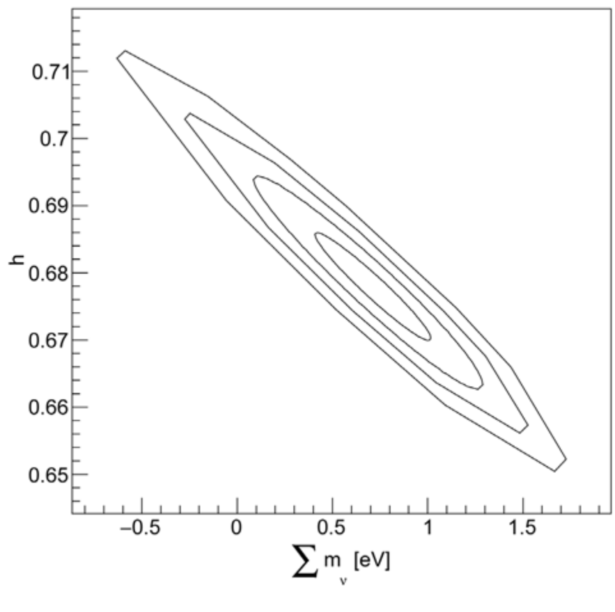

Figure 23. Contours corresponding to 1, 2, 3, and 4 standard deviations in the $(\sum m_\nu, h)$ plane, from Sachs-Wolfe, σ_8, $4\ \sigma/\bar{N}$, BAO, and $h = 0.678 \pm 0.009$ measurements. Points on the contours have $\chi^2 - \chi^2_{\min} = 1, 4, 9$, and 16, respectively, where χ^2 has been minimized with respect to N^2, n, b_0, and b_s. The total uncertainty of $\sum m_\nu$ is dominated by the uncertainty of h. In this figure the systematic uncertainties, presented in Equation (60), are not included.

Figure 23 and Equation (60) are our final results.

12. Conclusions

We have studied galaxy distributions with Sloan Digital Sky Survey SDSS DR14 data and with simulations searching for variables that can constrain neutrino masses. Fitting the predictions of the ΛCDM model to the Sachs-Wolfe effect, σ_8, $P_{\text{gal}}(k)$, fluctuations of galaxy counts in spheres of radii ranging from $16/h$ to $128/h$ Mpc, BAO measurements, and $h = 0.678 \pm 0.009$, in various combinations, *with free spectral index n*, and free galaxy bias *and galaxy bias slope*, we obtain consistent measurements of $\sum m_\nu$. The uncertainty of $\sum m_\nu$ is dominated by the uncertainty of *h*, so we have presented confidence contours in the $\left(\sum m_\nu, h\right)$ plane.

Fitting the predictions of the ΛCDM model to the Sachs-Wolfe effect and σ_8 we obtain (48). Fitting the predictions of the ΛCDM model to the Sachs-Wolfe effect, σ_8, and galaxy number fluctuations $\sigma/\bar{N}$ in spheres of radius $r_s = 16/h, 32/h, 64/h$, and $128/h$, we obtain (56). These results are consistent with the measurement (49) with BAO. Combining these last two independent measurements we obtain

$$\begin{aligned}\sum m_\nu &= 0.697 - 0.276 \cdot \delta h + 0.032 \cdot \delta n + 0.003 \cdot \delta\Omega_m \\ &\pm 0.075(\text{stat})^{+0.055}_{-0.028}(\text{syst})\,\text{eV}.\end{aligned} \tag{61}$$

Note that the uncertainty of $\sum m_\nu$ is dominated by the uncertainty of *h*. A global fit with $h = 0.678 \pm 0.009$ obtains $\sum m_\nu = 0.719 \pm 0.312(\text{stat})^{+0.055}_{-0.028}(\text{syst})$ eV, $h = 0.678 \pm 0.008$, and the amplitude and spectral index of $P(k)$: $N^2 = (2.09 \pm 0.33) \times 10^{-10}$, and $n = 1.021 \pm 0.075$. The fit also returns the galaxy bias *b* including its scale dependence.

Figure 23 and Equation (60) are our final results. These results follow from the data analyzed and the assumptions of the validity of the ΛCDM model and $h = 0.678 \pm 0.009$. The measured $\sum m_\nu$ is anticorrelated with *h*. All steps in this analysis have been fully described.

Note added in proof: Let us comment on Equations (49) and (56). Equation (49) is mainly determined by the precise measurement of the sound horizon angle θ_{MC} by the Planck experiment, and by the assumption that the BAO wave stalls at redshift $z = z_* = 1089.9 \pm 0.4$. Equation (49) tells us that $\left(\sum m_\nu, h\right)$ lies on the diagonal shown in Figure 23 (with some uncertainty from $\Omega_b h^2$). Equation (56) is a constraint mainly between $\sum m_\nu$ and *n* with large uncertainties. To determine $\sum m_\nu$ we need as input a value for *h* (or a value for *n*). In this article we have taken $h = 0.678 \pm 0.009$ from [3]. If $h = 0.678 \pm 0.009$ we obtain $\sum m_\nu = 0.719 \pm 0.312$ eV, and $n = 1.021 \pm 0.075$. If however $h = 0.688 \pm 0.009$ we obtain $\sum m_\nu = 0.412 \pm 0.328$ eV, and $n = 0.960 \pm 0.073$. And if $h \approx 0.697$, we obtain $\sum m_\nu \approx 0$ eV. Alternatively, if we fix $n = 1.0$, then $h = 0.681 \pm 0.005$ and $\sum m_\nu = 0.619 \pm 0.182$ eV. Or if we fix $n = 0.968$ [3], then $h = 0.684 \pm 0.005$ and $\sum m_\nu = 0.486 \pm 0.183$ eV. At the Guadeloupe 2018

Conference, Adam Riess, representing the SH_0ES Team, presented the latest direct measurement of the expansion parameter: $h = 0.7353 \pm 0.0162$, which corresponds to negative $\sum m_\nu$! The solution may come from an unexpected direction: gravitational waves from merging black holes are a "standard siren". The single black hole merger GW170817 already obtains $h = 0.70^{+0.12}_{-0.08}$, see the talk by Archil Kobakhidze!

Acknowledgements

Funding for the Sloan Digital Sky Survey (SDSS) has been provided by the Alfred P. Sloan Foundation, the Participating Institutions, the National Aeronautics and Space Administration, the National Science Foundation, the U.S. Department of Energy, the Japanese Monbukagakusho, and the Max Planck Society. The SDSS Web site is http://www.sdss.org/.

The SDSS is managed by the Astrophysical Research Consortium (ARC) for the Participating Institutions. The Participating Institutions are The University of Chicago, Fermilab, the Institute for Advanced Study, the Japan Participation Group, The Johns Hopkins University, Los Alamos National Laboratory, the Max-Planck-Institute for Astronomy (MPIA), the Max-Planck-Institute for Astrophysics (MPA), New Mexico State University, University of Pittsburgh, Princeton University, the United States Naval Observatory, and the University of Washington.

Conflicts of Interest

The authors declare no conflicts of interest regarding the publication of this paper.

References

[1] Sachs, R.K. and Wolfe, A.M. (1967) Perturbations of a Cosmological Model and Angular Variations of the Microwave Background. *The Astrophysical Journal*, **147**, 73. https://doi.org/10.1086/148982

[2] Steven Weinberg (2008) Cosmology. Oxford University Press, New York.

[3] Patrignani, C., *et al.* (2016) Review of Particle Physics. *Chinese Physics C*, **40**, 100001. https://doi.org/10.1088/1674-1137/40/10/100001

[4] Anderson, L., *et al.* (2012) The Clustering of Galaxies in the SDSS-III Baryon Oscillation Spectroscopic Survey: Baryon Acoustic Oscillations in the Data Release 9 Spectroscopic Galaxy Sample. *MNRAS*, **427**, 3435. https://doi.org/10.1111/j.1365-2966.2012.22066.x

[5] Blanton, M.R., *et al.* (2017) Sloan Digital Sky Survey IV: Mapping the Milky Way, Nearby Galaxies, and the Distant Universe. *The Astronomical Journal*, **154**, Article ID: 28.

[6] Dawson, K.S., *et al.* (2013) The Baryon Oscillation Spectroscopic Survey of SDSS-III. *The Astronomical Journal*, **145**, Article ID: 10.

[7] Hoeneisen, B. (2017) Study of Baryon Acoustic Oscillations with SDSS DR13 Data and Measurements of Ω_k and $\Omega_{DE}(a)$. *International Journal of Astronomy and*

Astrophysics, **7**, 11-27. https://doi.org/10.4236/ijaa.2017.71002

[8] Hoeneisen, B. (2018) Constraints on Neutrino Masses from Baryon Acoustic Oscillation Measurements. *International Journal of Astronomy and Astrophysics*, **8**, 1-5. https://doi.org/10.4236/ijaa.2018.81001

[9] Lesgourgues J. and Pastor S. (2006) Massive Neutrinos and Cosmology. *Physics Reports*, **429**, 307. https://doi.org/10.1016/j.physrep.2006.04.001

[10] Feldman H.A., Kaiser N. and Peacock J.A. (1994) Power-Spectrum Analysis of Three-Dimensional Redshift Surveys. *ApJ*, **426**, 23. https://doi.org/10.1086/174036

[11] Peebles, P.J.E. (1980) The Large-Scale Structure of the Universe. Princeton University Press.

[12] Hoeneisen, B. (2000) A Simple Model of the Hierarchical Formation of Galaxies. arXiv:astro-ph/0009071

International Journal of Astronomy and Astrophysics, 2018, 8, 258-266
http://www.scirp.org/journal/ijaa
ISSN Online: 2161-4725
ISSN Print: 2161-4717

The Great Wall of SDSS Galaxies

Lorenzo Zaninetti

Physics Department, Via P. Giuria 1, Turin, Italy
Email: zaninetti@ph.unito.it

How to cite this paper: Zaninetti, L. (2018) The Great Wall of SDSS Galaxies. *International Journal of Astronomy and Astrophysics*, **8**, 258-266.
https://doi.org/10.4236/ijaa.2018.83018

Received: July 16, 2018
Accepted: September 3, 2018
Published: September 6, 2018

Abstract

An enhancement in the number of galaxies as function of the redshift is visible on the SDSS Photometric Catalogue DR 12 at z = 0.383. This over-density of galaxies is named the Great Wall. This variable number of galaxies as a function of the redshift can be explained in the framework of the luminosity function for galaxies. The differential of the luminosity distance in respect to the redshift is evaluated in the framework of the LCDM cosmology.

Keywords

Galaxy Groups, Clusters, and Superclusters, Large Scale Structure of the Universe Cosmology

1. Introduction

We review some early works on the "CfA2 Great Wall", which is the name that was introduced by [1] to classify an enhancement in the number of galaxies as a function of the redshift that is visible in the Center for Astrophysics (CfA) redshift survey [2]. The evaluation of the two point correlation function was done by [3] on the three slices of the CfA redshift survey. A careful analysis was performed on Sloan Digital Sky Survey (SDSS) DR4 galaxies by [4]: The great wall was detected in the range $0.07 < z < 0.09$. The substructures, the morphology and the galaxy contents were analyzed by [5] [6] and the luminosities and masses of galaxies were discussed in the framework of SDSS-III's Baryon Oscillation Spectroscopic Survey (BOSS) [7]. The theoretical explanations for the Great Wall include an analysis of the peculiar velocities, see [8] [9], the nonlinear fields of the Zel'dovich approximation, see [10] [11] [12], and the cosmology of the Great Attractor, see [13]. The layout of the rest of this paper is as follows. In Section 2, we introduce the LCDM cosmology and the luminosity function for galaxies. In Section 3, we introduce the adopted catalog for galaxies and the theoretical basis of the maximum for galaxies as function of the redshift.

2. Preliminaries

This section introduces an approximate luminosity distance as a function of the redshift in LCDM and derives the connected differential. The Schechter luminosity function for galaxies is reviewed.

2.1. Adopted Cosmology

Some useful formulae in ΛCDM cosmology can be expressed in terms of a Padé approximant. The basic parameters are: the Hubble constant, H_0, expressed in km s^{-1}·Mpc^{-1}, the velocity of light, *c*, expressed in km·s^{-1}, and the three numbers Ω_{M}, Ω_K, and Ω_Λ, see [14] for more details. In the case of the Union 2.1 compilation, see [15], the parameters are $H_0 = 69.81\ \mathrm{km} \cdot \mathrm{s}^{-1} \cdot \mathrm{Mpc}^{-1}$, $\Omega_{\mathrm{M}} = 0.239$ and $\Omega_\Lambda = 0.651$. To have the luminosity distance, $D_L\left(z; H_0, c, \Omega_{\mathrm{M}}, \Omega_\Lambda\right)$, as a function of the redshift only, we apply the minimax rational approximation, which is characterized by the two parameters *p* and *q*. We find a simplified expression for the luminosity distance, $D_{L,6,2}$, when $p = 6$ and $q = 2$

$$D_{L,6,2} = \frac{ND}{0.284483 + 0.153266z + 0.0681615z^2} \quad \text{for } 0.001 < z < 4, \tag{1}$$

where

$$\begin{aligned} ND = &-0.0017 + 1221.80z + 1592.35z^2 + 504.386z^3 \\ &+ 85.8574z^4 + 0.41684z^5 + 0.186189z^6, \end{aligned} \tag{2}$$

The inverse of the above function, *i.e.* the redshift $z_{6,2}$ as function of the luminosity distance, is

$$\begin{aligned} z_{6,2} = &\, 3.3754 \times 10^{-5} D_L - 0.46438 + 2.1625 \times 10^{-14} \\ &\times \sqrt{2.4363 \times 10^{18} D_L^2 + 3.9538 \times 10^{23} D_L + 4.6114 \times 10^{26}}. \end{aligned} \tag{3}$$

2.2. Luminosity Function for Galaxies

We used the Schechter function, see [16], as a luminosity function (LF) for galaxies

$$\Phi(L)\mathrm{d}L = \left(\frac{\Phi^*}{L^*}\right)\left(\frac{L}{L^*}\right)^{\alpha} \exp\left(-\frac{L}{L^*}\right)\mathrm{d}L, \tag{4}$$

here α sets the slope for low values of luminosity, L, L^* is the characteristic luminosity and Φ^* is the normalisation. The equivalent distribution in absolute magnitude is

$$\Phi(M)\mathrm{d}M = 0.921\Phi^* 10^{0.4(\alpha+1)\left(M^*-M\right)} \exp\left(-10^{0.4\left(M^*-M\right)}\right)\mathrm{d}M, \tag{5}$$

where M^* is the characteristic magnitude as derived from the data. The scaling with *h* is $M^* - 5\log_{10} h$ and $\Phi^* h^3 \left[\mathrm{Mpc}^{-3}\right]$.

3. The Photometric Maximum

This section models the Great Wall that is visible on the SDSS Photometric Catalogue DR 12. It also evaluates the theoretical number of galaxies as a function of the redshift.

3.1. The SDSS Data

We processed the SDSS Photometric Catalogue DR 12, see [17], which contains 10,450,256 galaxies (elliptical + spiral) with redshift. In the following we will use the generic term galaxies without distinction between the two types, elliptical and spiral. The number of galaxies for an area in redshift of 0.025×0.025 of the u-band is reported in **Figure 1** as a contour plot and in **Figure 2** as a cut along a line.

3.2. The Theory

The flux, f, is

$$f=\frac{L}{4\pi r^2}, \tag{6}$$

where r is the luminosity distance. The luminosity distance is

$$r=D_{L,6,2}, \tag{7}$$

and the relationship between $\mathrm{d}r$ and $\mathrm{d}z$ is

$$\mathrm{d}r=\frac{N}{D}\mathrm{d}z, \tag{8}$$

where

$$\begin{aligned}N=&\,74813.67+10.9263z^7+49.05768z^6+2642.64259z^5+16024.51314z^4\\&+54307.16663z^3+127258.486z^2+195005.8564z,\end{aligned} \tag{9}$$

and

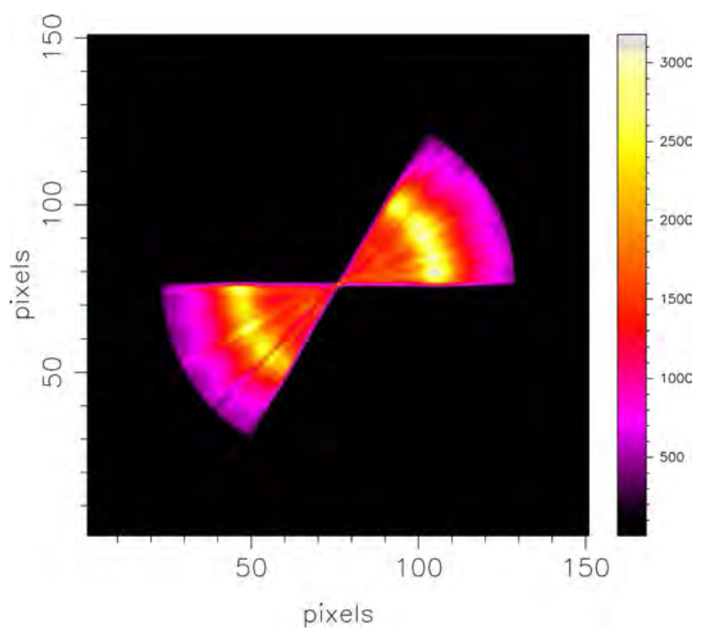

Figure 1. Contour for the number of galaxies (u-band) for areas of 0.025×0.025.

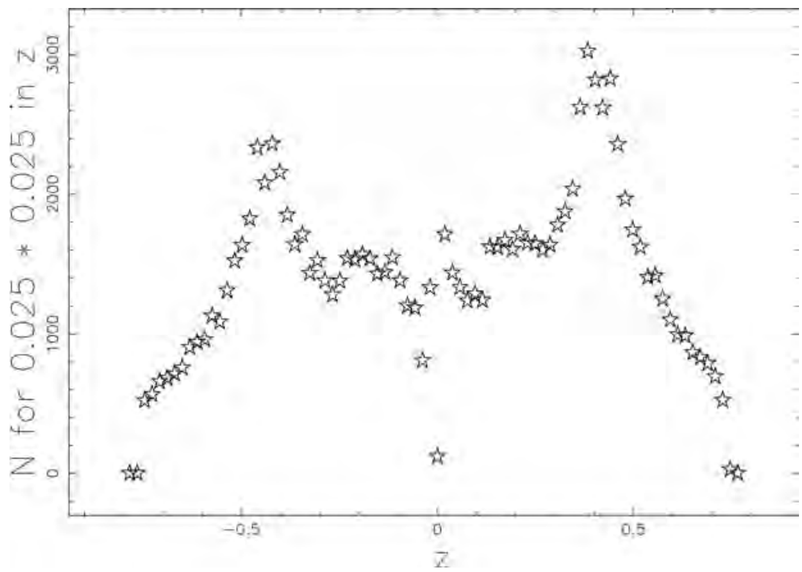

Figure 2. The number of galaxies (u-band) along a line for areas of 0.025×0.025.

$$D = \left(z^2 + 2.248575472z + 4.173664398\right)^2. \tag{10}$$

The joint distribution in z and f for the number of galaxies is

$$\frac{\mathrm{d}N}{\mathrm{d}\Omega \mathrm{d}z \mathrm{d}f} = \frac{1}{4\pi}\int_0^\infty 4\pi r^2 \mathrm{d}r \Phi\left(L; L^*, \sigma\right)\delta\left(z - \left(z_{6,2}\right)\right)\delta\left(f - \frac{L}{4\pi r^2}\right), \tag{11}$$

where δ is the Dirac delta function, $\Phi\left(L; L^*, \sigma\right)$ has been defined in Equation (4) and $z_{6,2}$ has been defined in Equation (3). The explicit version is

$$\frac{\mathrm{d}N}{\mathrm{d}\Omega \mathrm{d}z \mathrm{d}f} = \frac{NN}{DD}, \tag{12}$$

where

$$\begin{aligned} NN = {} & 644.3(z+1.058)^4 (z-0.000001412)^4 \left(z^2+4.889z+13.34\right)^4 \\ & \times \left(z^2-3.708z+464.6\right)^4 \mathrm{e}^{\frac{AA}{BB^2L^*}} \left(\frac{CC}{BB^2L^*}\right)^\alpha \Phi^*(z+0.5328) \\ & \times \left(z^2+5.047z+7.9141\right)\left(z^2+0.7z+7.011\right)\left(z^2-1.79z+231.58\right), \end{aligned} \tag{13}$$

$$\begin{aligned} CC = {} & f(z+1.058)^2 (z-0.0000014124)^2 \left(z^2+4.889z+13.343\right)^2 \\ & \times \left(z^2-3.708z+464.6\right)^2 \end{aligned} \tag{14}$$

$$DD = \left(z^2+2.248z+4.173\right)^6 L^* \tag{15}$$

$$\begin{aligned} AA = {} & -93.76 fz^{12} - 419.8 fz^{11} - 86945.4 fz^{10} - 701622.4 fz^9 \\ & - 22679411 fz^8 - 239083307 fz^7 - 1430432291 fz^6 \\ & - 4912205831 fz^5 + \left(4.540788\alpha L^* - 10191896880 f\right) z^4 \\ & + \left(20.4206\alpha L^* - 10524532830 f\right) z^3 + \left(60.862\alpha L^* - 4037704632 f\right) z^2 \\ & + \left(85.22\alpha L^* + 11406.2 f\right) z + 79.098\alpha L^* - 0.008055 f, \end{aligned} \tag{16}$$

$$BB = z^2 + 2.2485z + 4.173. \tag{17}$$

Figure 3 presents the number of galaxies that are observed in SDSS DR 12 as a function of the redshift for a given window in flux, in addition to the theoretical curve. The theoretical number of galaxies is reported in Figure 4 as a function of the flux and redshift, and is reported in Figure 5 as a function of α and redshift.

The total number of galaxies comprised between a minimum value of flux, $f_{\min}$, and a maximum value of flux $f_{\max}$, for the Schechter LF can be computed through the integral

$$\frac{\mathrm{d}N}{\mathrm{d}\Omega \mathrm{d}z} = \int_{f_{\min}}^{f_{\max}} \frac{NN}{DD} \mathrm{d}f. \tag{18}$$

This integral has a complicated analytical solution in terms of the Whittaker function $M_{\kappa,\mu}(z)$, see [18]. Figure 6 reports all of the galaxies of SDSS DR12 and also the theoretical curve.

A theoretical surface/contour of the Great Wall is displayed in Figure 7

4. Conclusions

1) ΛCDM cosmology

In this paper, we use the framework of ΛCDM cosmology with parameters $H_0 = 69.81\ \mathrm{km \cdot s^{-1} \cdot Mpc^{-1}}$, $\Omega_{\mathrm{M}} = 0.239$ and $\Omega_\Lambda = 0.651$. A relationship for

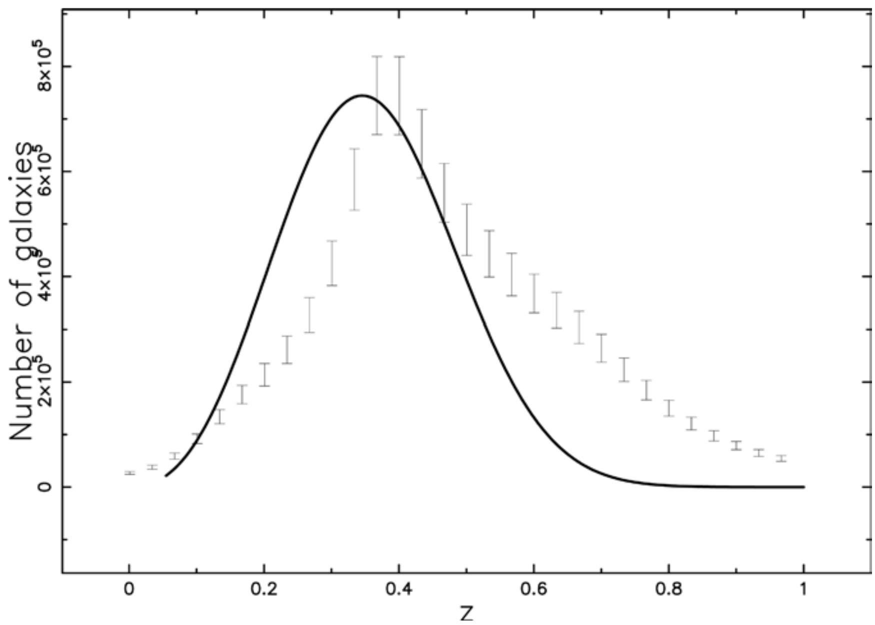

Figure 3. The galaxies of SDSS DR 12 (u-band) with $400 L_\odot/\mathrm{Mpc}^2 \le f \le 5\times10^7 L_\odot/\mathrm{Mpc}^2$ are organized by frequency versus distance (empty circles) and the error bar is given by the square root of the frequency. The maximum frequency of the observed galaxies is at $z = 0.38$. The full line is the theoretical curve that is generated by $\frac{\mathrm{d}N}{\mathrm{d}\Omega \mathrm{d}r \mathrm{d}f}$ as given by the application of the Schechter LF, which is Equation (12), and the theoretical maximum is at $z = 0.382$. The parameters are $L^* = 2.038\times10^{10} L_\odot$ and $\alpha = -0.9$.

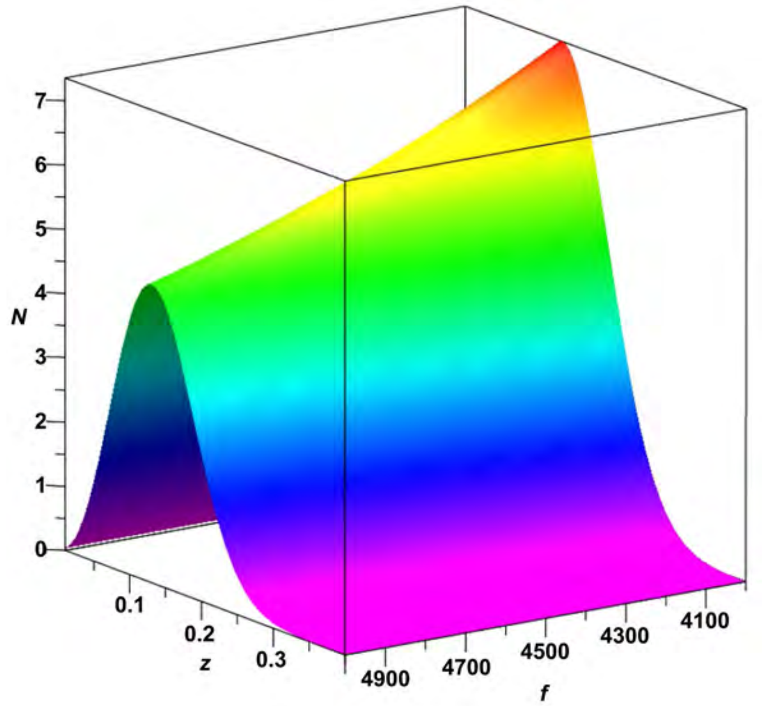

Figure 4. The theoretical number of galaxies divided by 1000 as a function of redshift and flux is expressed in $L_{\odot}/\text{Mpc}^2$. The parameters are $L^* = 2.038 \times 10^{10} L_{\odot}$, $\alpha = -0.9$ and $\frac{\Phi^*}{\text{Mpc}^{-3}} = 0.038$.

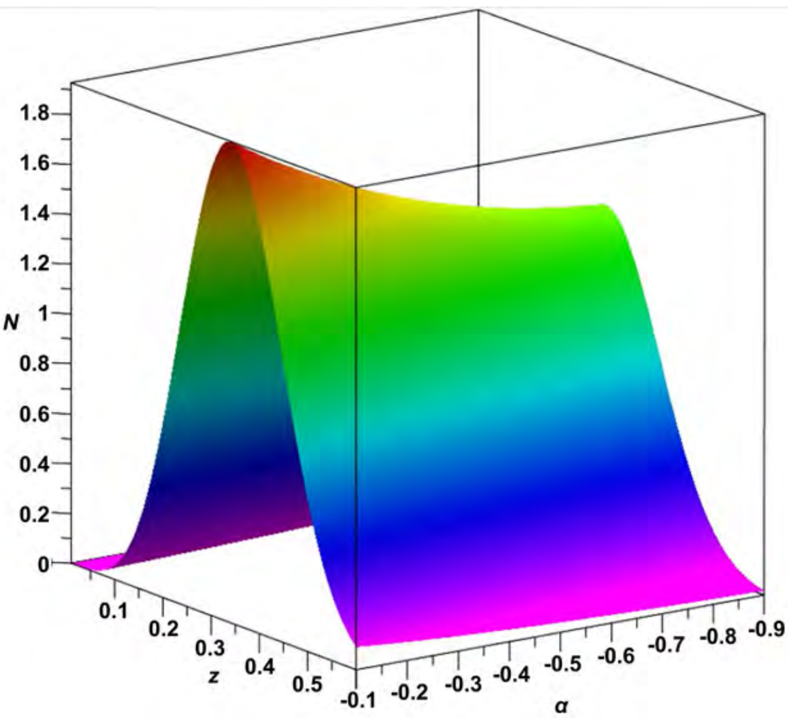

Figure 5. The theoretical number of galaxies divided by 100,000 as a function of α and redshift when $L^* = 2.038 \times 10^{10} L_{\odot}$, $f = 1000 L_{\odot}/\text{Mpc}^2$, and $\frac{\Phi^*}{\text{Mpc}^{-3}} = 0.038$.

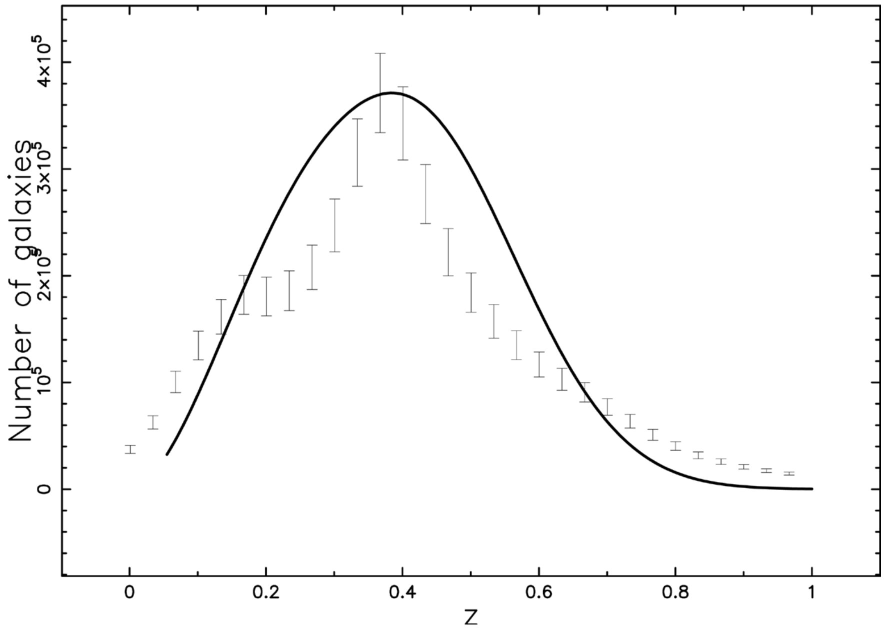

Figure 6. All of the galaxies of the SDSS DR12 catalog (u-band) are organized in frequencies versus spectroscopic redshift. The error bar is given by the square root of the frequency (Poisson distribution). The maximum frequency of all observed galaxies is at $z = 0.383$. The full line is the theoretical curve generated by $\frac{dN}{d\Omega dz}(z)$ as given by the numerical integration of Equation (18) with $L^* = 2.038\times10^{10} L_\odot$, $\alpha = -0.9$ and $\frac{\Phi^*}{\text{Mpc}^{-3}} = 0.038$.

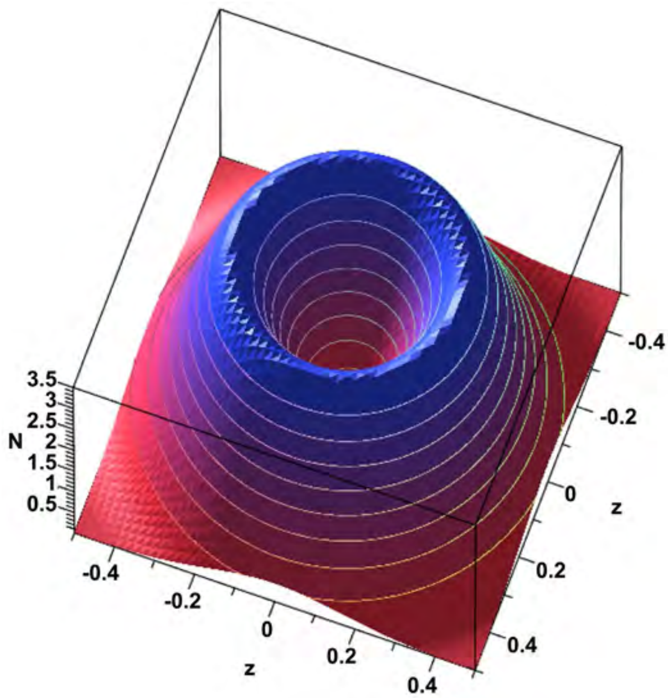

Figure 7. Theoretical surface/contour of the number of all the galaxies divided by 1,000,000 as a function of redshift. Parameters as in **Figure 6**.

the luminosity distance is derived using the method of the minimax approximation when $p = 6$ and $q = 2$, see Equation (2). The inverse relationship, the redshift as function of the luminosity function is derived in Equation (3).

2) The Great Wall

The enhancement in the number of galaxies as a function of the redshift for the SDSS Photometric Catalogue DR 12, which is at $z = 0.383$, is here modeled by the theoretical Equation (12) that is derived in the framework of the Schechter LF for galaxies and the ΛCDM cosmology. **Figure 6** reports the observed maximum in the number of galaxies and also the theoretical curve. These results are in agreement with a catalog of photometric redshift of ≈3,000,000 SDSS DR8 galaxies made by [19]: their Figure 9 bottom reports that the count of elliptical galaxies has a peak at $z \approx 0.37$ when the spirals galaxies conversely peaks at $z \approx 0.08$.

Acknowledgements

This research has made use of the VizieR catalogue access tool, CDS, Strasbourg, France.

Conflicts of Interest

The author declares no conflicts of interest regarding the publication of this paper.

References

[1] Geller, M.J. and Huchra, J.P. (1989) Mapping the Universe. *Science*, **246**, 897. https://doi.org/10.1126/science.246.4932.897

[2] de Lapparent, V., Geller, M.J. and Huchra, J.P. (1989) The Luminosity Function for the CfA Redshift Survey Slices. *Astrophysical Journal*, **343**, 1.

[3] Ramella, M., Geller, M.J. and Huchra, J.P. (1992) The Distribution of Galaxies within the "Great Wall". *Astrophysical Journal*, **384**, 396. https://doi.org/10.1086/170882

[4] Deng, X.F., He, J.Z., He, C.G., *et al.* (2007) The Sloan Great Wall from the SDSS Data Release 4. *Acta Physica Polonica B*, **38**, 219.

[5] Einasto, M., Tago, E., Saar, E., *et al.* (2010) The Sloan Great Wall. Rich Clusters. *Astronomy & Astrophysics*, **522**, A92.

[6] Einasto, M., Liivamägi, L.J., Tempel, E., *et al.* (2011) The Sloan Great Wall. Morphology and Galaxy Content. *Astrophysical Journal*, **736**, 51.

[7] Einasto, M., Lietzen, H., Gramann, M., *et al.* (2017) BOSS Great Wall: Morphology, Luminosity, and Mass. *Astronomy & Astrophysics*, **603**, A5

[8] dell'Antonio, I.P., Bothun, G.D. and Geller, M.J. (1996) Peculiar Velocities for Galaxies in the Great Wall. I. The Data. *The Astronomical Journal*, **112**, 1759.

[9] dell'Antonio, I.P., Geller, M.J. and Bothun, G.D. (1996) Peculiar Velocities for Galaxies in the Great Wall. II. Analysis. *The Astronomical Journal*, **112**, 1780.

[10] Zel'dovich, Y.B. (1970) Gravitational Instability: An Approximate Theory for Large Density Perturbations. *Astronomy & Astrophysics*, **5**, 84.

[11] Shandarin, S.F. (2009) The Origin of "Great Walls". *Journal of Cosmology and Astroparticle Physic*, **2**, 031.

[12] Shandarin, S.F. (2011) The Multi-Stream Flows and the Dynamics of the Cosmic Web. *Journal of Cosmology and Astroparticle Physic*, **5**, 015.

[13] Valkenburg, W. and Bjælde, O.E. (2012) Cosmology When Living near the Great Attractor. *Monthly Notices of the Royal Astronomical Society*, **424**, 495

[14] Zaninetti, L. (2016) Pade Approximant and Minimax Rational Approximation in Standard Cosmology. *Galaxies*, **4**, 4. http://www.mdpi.com/2075-4434/4/1/4

[15] Suzuki, N., Rubin, D., Lidman, C., Aldering, G., Amanullah, R., Barbary, K. and Barrientos, L.F. (2012) The Hubble Space Telescope Cluster Supernova Survey. V. Improving the Dark-Energy Constraints above z Greater than 1 and Building an Early-Type-Hosted Supernova Sample. *Astrophysical Journal*, **746**, 85.

[16] Schechter, P. (1976) An Analytic Expression for the Luminosity Function for Galaxies. *Astrophysical Journal*, **203**, 297. https://doi.org/10.1086/154079

[17] Alam, S., Albareti, F.D., Allende Prieto, C., *et al*. (2015) The Eleventh and Twelfth Data Releases of the Sloan Digital Sky Survey: Final Data from SDSS-III. *The Astrophysical Journal Supplement*, **219**, 12 (Preprint).

[18] Olver, F.W.J., Lozier, D.W., Boisvert, R.F. and Clark, C.W. (2010) NIST Handbook of Mathematical Functions. Cambridge University Press, Cambridge.

[19] Paul, N., Virag, N. and Shamir, L. (2018) A Catalog of Photometric Redshift and the Distribution of Broad Galaxy Morphologies. *Galaxies*, **6**.

International Journal of Astronomy and Astrophysics, 2018, 8, 267-274
http://www.scirp.org/journal/ijaa
ISSN Online: 2161-4725
ISSN Print: 2161-4717

Possibility of Classical Entanglement at LIGO

Partha Ghose[1], **A. K. Rajagopal**[2]

[1]National Academy of Sciences, India, Allahabad, India
[2]Inspire Institute Inc., Alexandria, USA
Email: partha.ghose@gmail.com, attipat.rajagopal@gmail.com

How to cite this paper: Ghose, P. and Rajagopal, A.K. (2018) Possibility of Classical Entanglement at LIGO. *International Journal of Astronomy and Astrophysics*, **8**, 267-274.
https://doi.org/10.4236/ijaa.2018.83019

Received: July 11, 2018
Accepted: September 3, 2018
Published: September 6, 2018

Abstract

It is now established that entanglement in the sense of local non-factorizability of two or more degrees of freedom of a system occurs in classical polarization optics. We extend the idea to weak gravitational waves which are strikingly similar to optical waves. It is shown that a linearized classical gravity wave can in principle get entangled in the sense mentioned with the vibrational modes of an array of test masses in a plane perpendicular to its direction of propagation. A Bell-CHSH inequality based on the requirement of noncontextuality for classical realism is derived, and it is shown that the putative nonfactorizable state violates this inequality. The idea is therefore empirically falsifiable.

Keywords

Entanglement, Classical Optics, Gravitational Waves

1. Introduction

It is fairly well established by now that entanglement in the sense of *local* non-factorizability of two or more degrees of freedom occurs in classical polarization optics [1] [2] [3] [4] [5]. Entanglement in this sense depends only on the physical existence of orthogonal Hilbert spaces, such as the polarization and propagation modes of light. Entanglement *per se* is not exclusive to quantum mechanics. In fact, the Schmidt decomposition theorem on which bipartite entanglement is based is pre-quantum mechanical [6]. This idea of entanglement can be extended to weak gravitational wave physics which has a striking similarity to classical polarization optics. In fact, the only difference is in the structure of polarization. Hence entanglement can, in principle, occur between the polarization modes of the gravitational wave and the vibrational modes of an array of masses which span orthogonal Hilbert spaces, and are therefore subject to the Schmidt theorem. The purpose of the paper is to point to such a possibility at LIGO, and propose how to test if it really occurs.

Section 2 gives a quick summary of gravitational wave physics relevant for our purpose. In Section 3 we show how the putative entanglement can occur at LIGO. In Section 4 we deduce a Bell-CHSH type inequality based on classical realism and noncontextuality, and show that the entangled state violates this inequality.

2. Introduction: Gravitational Waves and Polarization

For weak gravitational fields Einstein's equation

$$R_{\mu\nu} = -8\pi G\left(T_{\mu\nu} - \frac{1}{2}g_{\mu\nu}T_{\lambda}^{\lambda}\right) \tag{1}$$

can be linearized by writing the metric in the form

$$g_{\mu\nu}(x) = \eta_{\mu\nu} + h_{\mu\nu}(x) \tag{2}$$

where $\eta_{\mu\nu}$ is the flat Minkowski metric and $h_{\mu\nu} \ll 1$ is a small perturbation. To the lowest order in the perturbation the vacuum equation $R_{\mu\nu} = 0$ is then of the linearized form [7] [8] [9]

$$\Box h_{\mu\nu} - \partial_{\mu}\xi_{\nu} - \partial_{\nu}\xi_{\mu} = 0 \tag{3}$$

where $\Box = \eta^{\alpha\beta}\partial_{\alpha\beta} = -\partial^2/\partial t^2 + \nabla^2$ and

$$\xi_{\mu} = \partial_{\gamma}h_{\mu}^{\gamma} - \frac{1}{2}\partial_{\mu}h_{\gamma}^{\gamma}. \tag{4}$$

This equation can be written in the form

$$\Box h_{\mu\nu} = 0, \tag{5}$$

$$\partial_{\nu}h_{\mu}^{\nu}(x) - \frac{1}{2}\partial_{\mu}h_{\nu}^{\gamma} = 0, \tag{6}$$

where the first equation is the linearized Einstein equation and the second equation is the Lorentz gauge constraint, where $h_{\nu}^{\gamma} \equiv \eta^{\gamma\delta}h_{\delta\nu}$. A general solution is of the form

$$h_{\mu\nu}(x) = \alpha_{\mu\nu}\mathrm{e}^{ik_{\lambda}x^{\lambda}} + \alpha_{\mu\nu}^{*}\mathrm{e}^{-ik_{\lambda}x^{\lambda}} \tag{7}$$

with $k_{\mu}^{\mu} = 0$, $k^{\mu} = \eta^{\mu\nu}k_{\nu}$, where $\alpha_{\mu\nu}$ is the polarization tensor which is symmetric in (μ,ν) and so has ten components, but this number can be reduced to two by making use of Bianchi identities and fixing the gauge.

In the *transverse-traceless gauge* (TT gauge) the metric perturbation is made purely spatial by requiring $h_{tt} = h_{ti} = 0$ and also traceless, $h_{i}^{\ i} = 0$. Then the Lorentz gauge constraint (6) becomes

$$\partial_{i}h_{ij} = 0, \tag{8}$$

which ensures transversality. For propagation in the z direction with a fixed frequency ω and $k^{\mu} = (\omega,0,0,\omega)$, $k\cdot x = \omega(z-t)$ and $c = 1$, the general solution can be written as

$$h_{\mu\nu}(z)=\begin{pmatrix}0 & 0 & 0 & 0\\ 0 & \alpha_{11} & \alpha_{12} & 0\\ 0 & \alpha_{12} & -\alpha_{11} & 0\\ 0 & 0 & 0 & 0\end{pmatrix}e^{i\omega(z-t)} \tag{9}$$

which has two independent transverse polarization states and helicity ±2. The part proportional to $\alpha_{xx}=\alpha_{11}$ is called the *plus-polarization* state and is denoted by +, and the part proportional to $\alpha_{xy}=\alpha_{12}=\alpha_{21}$ is called the *cross-polarization* state and is denoted by ×. It is in this sense that one usually associates spin-2 with gravity.

It will be convenient for our purpose to write the above solution in the form

$$h(z)=\left[f_\times(t-z)\varepsilon_\times+f_+(t-z)\varepsilon_+\right]e^{i\omega(z-t)} \tag{10}$$

$$\equiv h_\times(z)+h_+(z) \tag{11}$$

where h and ϵ are 4×4 matrices with elements $h_{\mu\nu},\varepsilon_{\mu\nu}$ etc, and $h_\times(z),h_+(z)$ are respectively the purely cross-polarized and purely plus-polarized gravity waves along the z axis, where

$$\varepsilon_\times=\begin{pmatrix}0 & 0 & 0 & 0\\ 0 & 0 & 1 & 0\\ 0 & 1 & 0 & 0\\ 0 & 0 & 0 & 0\end{pmatrix} \tag{12}$$

$$\varepsilon_+=\begin{pmatrix}0 & 0 & 0 & 0\\ 0 & 1 & 0 & 0\\ 0 & 0 & -1 & 0\\ 0 & 0 & 0 & 0\end{pmatrix} \tag{13}$$

are the unit polarization tensors. Notice that $\epsilon_\times\epsilon_+ +\epsilon_+\epsilon_\times=0$. Hence, $h_\times(z)$ and $h_+(z)$ anti-commute. The physical implications of this property need to be investigated further.

Using the basis vectors $|+\rangle=(0,1,0,0)^{\mathrm{T}}$, $|-\rangle=(0,0,1,0)^{\mathrm{T}}$, one can construct $\varepsilon_\times=|+\rangle\otimes|-\rangle+|-\rangle\otimes|+\rangle\equiv|+-\rangle+|-+\rangle$, and $\varepsilon_+=|+\rangle\otimes|+\rangle-|-\rangle\otimes|-\rangle\equiv|++\rangle-|--\rangle$. The other two basis vectors $(1,0,0,0)^{\mathrm{T}}$ and $(0,0,0,1)^{\mathrm{T}}$ are eliminated by choosing the TT gauge which makes the metric perturbation purely spatial and transverse.

The inner product of two matrices A and B is defined by the Frobenius product

$$\langle A|B\rangle=\frac{1}{2}Tr\left(A^\dagger B\right). \tag{14}$$

Hence, we have $\langle\varepsilon_+|\varepsilon_+\rangle=\langle\varepsilon_\times|\varepsilon_\times\rangle=1,\langle\varepsilon_+|\varepsilon_\times\rangle=\langle\varepsilon_\times|\varepsilon_+\rangle=0$.

3. Entanglement and Classical Gravity

According to the Equivalence Principle the effects of gravity can be transformed away in a local enough region that tidal effects can be ignored. Therefore, the effect of gravity on a single test mass has no physical significance. But two or more test masses in different locations can be physically influenced by linearized gravity waves which can change their "proper distances". Linearized gravity waves are transverse and can therefore change the proper distances between test masses in a plane perpendicular to their propagation direction. If, therefore, a gravity wave like $h(z)$ (Equation (11)) travelling in the z direction is incident on an array of coplanar test masses at various locations in the xy plane (as, for example, in each arm of a laser interferometer like LIGO), it can be shown [7] [9] that the proper distances between the test masses will oscillate with the wave frequency $\nu = \omega/2\pi$ in two elliptical modes, one with axes parallel to the (x, y) axes corresponding to the plus-polarization wave and the other with axes rotated by $\pi/4$ relative to the (x, y) axes, corresponding to the cross-polarization wave. This $\pi/4$ rotation is because gravity is a rank-2 tensor field.

Hence, the state of the total system (test masses + gravity wave) must be of the form

$$|H\rangle = |h_+\rangle |(xy)_+\rangle + |h_\times\rangle |(xy)_\times\rangle \tag{15}$$

where $|h_+\rangle$ and $|h_\times\rangle$ denote the two orthogonal polarization states of the classical gravity wave, and $|(xy)_+\rangle$ and $|(xy)_\times\rangle$ denote the corresponding oscillation modes of the two arms of the classical interferometer in the xy plane which span an orthogonal Hilbert space. The h_+ component of the wave cannot produce $(xy)_\times$ oscillation modes and the $h_\times$ component cannot produce $(xy)_+$ oscillation modes, and therefore the states $|h_+\rangle |(xy)_\times\rangle$ and $|h_\times\rangle |(xy)_+\rangle$ cannot occur. Hence, (15) is a non-factorizable, and in that sense, "entangled" state of the two gravitational polarization modes and the corresponding oscillation modes of the classical detector. This is analogous to what happens in the quantum theory of measurement in which the apparatus gets entangled with the system to be measured. Hence the entanglement is between modes of two different systems, and differs from entanglement of two modes of the same system as in classical polarization optics.

The recent detection of gravitational waves may therefore be signalling entanglement in classical gravitational physics. We now propose a possible way of testing this hypothesis.

4. Contextuality in Classical Gravity: A Bell-CHSH Test

Let us consider a LIGO set up with the two arms of the laser interferometer in the xy plane, and a gravitational wave incident on it along the z direction. As we have seen from Equation (9), in the TT gauge there are two independent degrees of freedom and two amplitudes $\alpha_{xx} = -\alpha_{yy}$ and $\alpha_{xy} = \alpha_{yx}$. A wave with $\alpha_{xy} = 0$ produces a metric

$$\mathrm{d}s^2 = -\mathrm{d}t^2 + (1 + h_+)\mathrm{d}x^2 + (1 - h_+)\mathrm{d}y^2 + \mathrm{d}z^2 \tag{16}$$

where $h_+ = \alpha_{xx} \exp(i\omega(z - t))$. This produces opposite effects on the proper distance on the two axes, contracting one and expanding the other. On the other hand, if $\alpha_{xx} = 0$, only the off-diagonal terms $h_{xy} = h_{yx} = h_\times$ in the metric are non-zero, and that corresponds to a $\pi/4$ rotation relative to the previous case. A general wave is a linear superposition of these two, and depending on the phase relation, a circular or elliptical polarization is produced. Consequently, the proper distances between the test masses in the interferometer are stretched and compressed along the x and y directions periodically in two modes, one parallel to the (xy) axes (the plus mode) and the other rotated by $\pi/4$ relative to the (xy) axes (the cross mode). An interferometer in the (xy) plane can measure the difference in the return times of light along the two arms in the x and y directions due to these changes in the proper distances through the phase changes they produce, resulting in fringe shifts in the interference pattern. Hence, the normalized state of the gravitational wave plus the oscillatory interferometer paths can be written in the form

$$\left|\hat{H}\right\rangle = \frac{1}{\sqrt{2}}\left(\left|h_+\right\rangle\left|(xy)_+\right\rangle + \left|h_\times\right\rangle\left|(xy)_\times\right\rangle\right) \tag{17}$$

where $\left|(xy)_+\right\rangle$ and $\left|(xy)_\times\right\rangle$ denote the two oscillation modes of the arms of the interferometer.

To derive a Bell-CHSH inequality based on noncontextuality, let us first consider an arbitrary general state

$$\left|H\right\rangle = \left(\cos\alpha\left|h_+\right\rangle + \mathrm{e}^{i\beta}\sin\alpha\left|h_\times\right\rangle\right)\left(\cos\gamma\left|(xy)_+\right\rangle + \mathrm{e}^{i\delta}\sin\gamma\left|(xy)_\times\right\rangle\right) \tag{18}$$

$$\equiv \left|\psi_h\right\rangle\left|\psi_{xy}\right\rangle \tag{19}$$

where $\alpha,\beta,\gamma,\delta$ are arbitrary parameters. Next, let us define the correlation

$$E(\theta,\phi) = \left\langle H\right|\sigma_\theta \cdot \sigma_\phi\left|H\right\rangle \tag{20}$$

where $\left|H\right\rangle$ is an arbitrary normalized state of the apparatus + gravity, and

$$\sigma_\theta = \sigma_{\theta,0} - \sigma_{\theta,\pi}, \tag{21}$$

$$\sigma_\phi = \sigma_{\phi,0} - \sigma_{\phi,\pi}, \tag{22}$$

with

$$\begin{aligned}
\sigma_{\theta,0} &= \frac{1}{2}\left(\left|h_+\right\rangle + \mathrm{e}^{i\theta}\left|h_\times\right\rangle\right)\left(\left\langle h_+\right| + \mathrm{e}^{-i\theta}\left\langle h_\times\right|\right)\otimes\mathbb{I}_{xy},\\
\sigma_{\theta,\pi} &= \frac{1}{2}\left(\left|h_+\right\rangle - \mathrm{e}^{i\theta}\left|h_\times\right\rangle\right)\left(\left\langle h_+\right| - \mathrm{e}^{-i\theta}\left\langle h_\times\right|\right)\otimes\mathbb{I}_{xy},\\
\sigma_{\phi,0} &= \mathbb{I}_h\otimes\frac{1}{2}\left(\left|(xy)_+\right\rangle + \mathrm{e}^{i\phi}\left|(xy)_\times\right\rangle\right)\left(\left\langle(xy)_+\right| + e^{-i\phi}\left\langle(xy)_\times\right|\right),\\
\sigma_{\phi,\pi} &= \mathbb{I}_h\otimes\frac{1}{2}\left(\left|(xy)_+\right\rangle - \mathrm{e}^{i\phi}\left|(xy)_\times\right\rangle\right)\left(\left\langle(xy)_+\right| - \mathrm{e}^{-i\phi}\left\langle(xy)_\times\right|\right),
\end{aligned} \tag{23}$$

where θ and ϕ are phase shifts between the two polarization modes and the two path oscillation modes respectively, and $\mathbb{I}_{xy}$ and $\mathbb{I}_h$ are the identity operators in the Hilbert space $\mathcal{H}_{xy}$ spanned by the oscillating interferometer paths and the Hilbert space $\mathcal{H}_h$ spanned by the gravity wave polarizations respectively. Hence,

$$\sigma_\theta = \left(e^{-i\theta}\left|h_+\right\rangle\left\langle h_\times\right| + e^{i\theta}\left|h_\times\right\rangle\left\langle h_+\right|\right)\otimes \mathbb{I}_{xy}, \tag{24}$$

$$\sigma_\phi = \mathbb{I}_h \otimes\left(e^{-i\phi}\left|(xy)_+\right\rangle\left\langle (xy)_\times\right| + e^{i\phi}\left|(xy)_\times\right\rangle\left\langle (xy)_+\right|\right). \tag{25}$$

It should be noted that σ_θ and σ_ϕ act upon different Hilbert spaces altogether, and hence they commute with each other. This property is necessary for noncontextuality of the apparatus + gravity wave system. It has always been a tenet of classical physics that whatever exists in the physical world is independent of observations which only serve to reveal them. Put more technically, this means that the result of a measurement is predetermined and is not affected by how the value is measured, *i.e.* not affected by previous or simultaneous measurement of any other *compatible* or co-measureable observable. Hence the need for commuting observables to test noncontextuality.

For the general product state (19),

$$E(\theta,\phi) = \langle\psi_h|\sigma_\theta|\psi_h\rangle\left\langle\psi_{xy}\right|\sigma_\phi\left|\psi_{xy}\right\rangle = E_h(\theta)E_{xy}(\phi), \tag{26}$$

with

$$E_h(\theta) = \sin 2\alpha\cos(\beta-\theta), \tag{27}$$

$$E_{xy}(\phi) = \sin 2\gamma\cos(\delta-\phi). \tag{28}$$

Thus, the expectation value $E(\theta,\phi)$ is the product of the expectation values of the polarization and proper distance (or path) projections. Hence, the path and polarization measurements for product states in classical gravity are independent of one another in all contexts. This is the content of *noncontextuality*. This may, at first sight, look obvious and trivial, but on closer inspection, one finds that it implies the inequality

$$-1 \le E(\theta,\phi) \le 1 \tag{29}$$

for the correlation.

Now, define a quantity S as

$$S(\theta_1,\phi_1;\theta_2,\phi_2) = E(\theta_1,\phi_1) + E(\theta_1,\phi_2) - E(\theta_2,\phi_1) + E(\theta_2,\phi_2). \tag{30}$$

It follows from (29) that

$$|S| \le 2. \tag{31}$$

All that is required to derive this bound for product states is that *the correlations lie between* -1 *and* $+1$, which is guaranteed by the results (27) and (28).

Now consider the correlation calculated for the normalized state (17), namely

$$E(\theta,\phi) = \left\langle\hat{H}\right|\sigma_\theta\cdot\sigma_\phi\left|\hat{H}\right\rangle$$

$$= \left\langle\hat{H}\right|\left[(+)\sigma_{\theta,0} + (-)\sigma_{\theta,\pi}\right]\cdot\left[(+)\sigma_{\phi,0} + (-)\sigma_{\phi,\pi}\right]\left|\hat{H}\right\rangle \tag{32}$$

$$= \left\langle\hat{H}\right|\left[\sigma_{\theta,0}\cdot\sigma_{\phi,0} + \sigma_{\theta,\pi}\cdot\sigma_{\phi,\pi} - \sigma_{\theta,0}\cdot\sigma_{\phi,\pi} - \sigma_{\theta,\pi}\cdot\sigma_{\phi,0}\right]\left|\hat{H}\right\rangle \tag{33}$$

The intensities corresponding to the four possible orientations are given by

$$I(\theta,\phi) = \left\langle\hat{H}\right|\sigma_{\theta,0}\cdot\sigma_{\phi,0}\left|\hat{H}\right\rangle,$$

$$
\begin{aligned}
I(\theta+\pi,\phi+\pi) &= \langle \hat{H} | \sigma_{\theta,\pi} \cdot \sigma_{\phi,\pi} | \hat{H} \rangle, \\
I(\theta+\pi,\phi) &= \langle \hat{H} | \sigma_{\theta,\pi} \cdot \sigma_{\phi,0} | \hat{H} \rangle, \\
I(\theta,\phi+\pi) &= \langle \hat{H} | \sigma_{\theta,0} \cdot \sigma_{\phi,\pi} | \hat{H} \rangle,
\end{aligned} \tag{34}
$$

where clearly $I(\theta,\phi)=\frac{1}{2}\left[1+\cos(\theta+\phi)\right]$ from (17) and the definitions (23).

We can write $E(\theta,\phi)$ in terms of the normalized intensities as

$$
E(\theta,\phi)=\frac{I(\theta,\phi)+I(\theta+\pi,\phi+\pi)-I(\theta+\pi,\phi)-I(\theta,\phi+\pi)}{I(\theta,\phi)+I(\theta+\pi,\phi+\pi)+I(\theta+\pi,\phi)+I(\theta,\phi+\pi)}=\cos(\theta+\phi). \tag{35}
$$

It is clear from this that the noncontextuality bound (31) is violated by the state (17) for the set of parameters $\theta_1=0,\theta_2=\pi/2,\phi_1=\pi/4,\phi_2=-\pi/4$ for which $|S|=2\sqrt{2}$. Since the distance and polarization changes occur in the same path, there is no violation of locality in this result. It is hoped that these predictions can one day be verified at facilities like LIGO.

Since we have used purely classical physics throughout, it is clear that *entanglement* and *contextuality* which are widely regarded as exclusively quantum mechanical, occur in classical gravity too.

Acknowledgements

The authors thank the S. N. Bose National Centre for Basic Sciences, Kolkata for inviting them to the *International Symposium on New Frontiers in Quantum Correlations*, Jan 29-Feb 2, 2018, where the basic ideas were developed. PG also thanks the National Academy of Sciences, India for a grant.

Conflicts of Interest

The authors declare no conflicts of interest regarding the publication of this paper.

References

[1] Spreeuw, R.J.C. (1998) A Classical Analogy of Entanglement. *Foundations of Physics*, **28**, 361. https://doi.org/10.1023/A:1018703709245

[2] Ghose, P. and Samal, M.K. (2001) EPR Type Nonlocality in Classical Electrodynamics. arXiv [quant-ph]/0111119

[3] Ghose, P. and Mukherjee, A. (2014) Entanglement in Classical Optics. *Reviews in Theoretical Science*, **2**, 1.

[4] Ghose, P. and Mukherjee, A. (2014) Novel States of Classical Light and Noncontextuality. *Advanced Science*, *Engineering and Medicine*, **6**, 246.

[5] Eberly, J.H., *et al.* (2016) Quantum and Classical Optics—Emerging Links. *Physica Scripta*, **91**, 063003 and References Therein.

[6] Schmidt, E. (1907) Zur Theorie der linearen und nichtlinearen Integralgleichungen. *Mathematische Annalen*, **63**, 433. https://doi.org/10.1007/BF01449770

[7] Thorne, K.S. (2009) Gravitational Radiation: The Physics of Gravitational Waves and Their Generation.
https://www.lorentz.leidenuniv.nl/lorentzchair/thorne/Thorne1.pdf

[8] Schutz, B.F. and Ricci, F. (2001) Gravitational Waves, Theory and Experiment (an Overview). In: Ciufolini, I., Gorini, V., Moschella, U. and Fré, P., Eds., *Gravitational Waves,* IoP Publishing, Bristol, 15-19.

[9] Guidry, M.W. (2013) Lectures on *Theoretical Astrophysics*, Chapter 21. http://eagle:phys.utk.edu/guidry/astro616/lectures/lecture$_c$h21.pdf

International Journal of Astronomy and Astrophysics, 2018, 8, 275-298
http://www.scirp.org/journal/ijaa
ISSN Online: 2161-4725
ISSN Print: 2161-4717

Evolution of Angular Momentum and Orbital Period Changes in Close Double White Dwarf Binaries

Seblu Humne Negu*, Solomon Belay Tessema

Astronomy and Astrophysics Research Development Department, Ethiopian Space Science and Technology Institute (ESSTI)-Entoto Observatory and Research Center (EORC), Addis Ababa, Ethiopia
Email: *seblu1557@gmail.com, tessemabelay@gmail.com

How to cite this paper: Negu, S.H. and Tessema, S.B. (2018) Evolution of Angular Momentum and Orbital Period Changes in Close Double White Dwarf Binaries. *International Journal of Astronomy and Astrophysics*, **8**, 275-298.
https://doi.org/10.4236/ijaa.2018.83020

Received: July 26, 2018
Accepted: September 25, 2018
Published: September 28, 2018

Abstract

We have presented the evolution of angular momentum and orbital period changes between the component spins and the orbit in close double white dwarf binaries undergoing mass transfer through direct impact accretion over a broad range of orbital parameter space. This work improves upon similar earlier studies in a number of ways: First, we calculate self-consistently the angular momentum of the orbit at all times. This includes gravitational, tides and mass transfer effects in the orbital evolution of the component structure models, and allow the Roche lobe radius of the donor star and the rotational angular velocities of both components to vary, and account for the exchange of angular momentum between the spins of the white dwarfs and the orbit. Second, we investigate the mass transfer by modeling the ballistic motion of a point mass ejected from the center of the donor star through the inner Lagrangian point. Finally, we ensure that the angular momentum is conserved, which requires the donor star spin to vary self-consistently. With these improvements, we calculate the angular momentum and orbital period changes of the orbit and each binary component across the entire parameter space of direct impact double white dwarf binary systems. We find a significant decrease in the amount of angular momentum removed from the orbit during mass transfer, as well as cases where this process increases the angular momentum and orbital period of the orbit at the expense of the spin angular momentum of the donor and accretor. We find that our analysis yields an increase in the predicted number of stable systems compared to that in the previous studies, survive the onset of mass transfer, even if this mass transfer is initially unstable. In addition, as a consequence of the tidal coupling, systems that come into contact near the mass transfer instability boundary undergo a phase of mass transfer with their orbital period.

Keywords

Stars: DWD Binaries, Mass Transfer, Methods: Numerical

1. Introduction

Double white dwarf (DWD) binaries provide an interesting key to understand a variety of areas in astrophysics. Their birth properties provide insight into the evolution of their progenitors [1], as well as the dynamics of common envelope evolution [2]. From a population standpoint, the DWD binary systems may make up the largest fraction of the close binary stars in our Galaxy.

Following common envelope evolution, DWD binaries may emerge with a sufficiently short orbital period and rotational angular velocities, allowing gravitational radiation (GR), tides and mass transfer to drive the stars closer together on an astrophysically interesting time scale. Prior to the onset of mass transfer, their orbit will be shrink due to the effect of angular momentum via GR. Tidal forces are thought to synchronize the spin and orbital periods of the white dwarfs by the time that the white dwarfs are close enough together to begin transferring mass ([3] [4]).

As the degenerate components of a DWD binary orbit continues to shrink via GR, the less massive component will inevitably fill its Roche lobe and begin transferring matter to its companion and the system will enter into a stable semi-detached state. In the case where the mass transfer is stable, such systems may be identifiable as AM CVn ([5] [6]), which have extremely short orbital periods, but we still lack a uniform theoretical understanding of the detail nature of those binaries for all possible mass ratios, orbital parameters and origins. However, one would like our theoretical understanding to be such that given a white dwarf binary of arbitrary masses and compositions at the time that the less massive component gets into contact, one could reconstruct the previous evolutionary pathways and the subsequent evolution to merger, tidal disruption or stable mass transfer.

Mass transfer in close DWD binaries has generally been taken to be stable if the mass ratio is smaller than 0.8. However, [6] identified the interesting possibility of the mass transfer stream that directly impact the surface of the accretor during this phase. The nature of it may depend both on the structure of the donor and the mass ratio of components. Thus, a stream of matter is pulled from the donor star through the inner Lagrangian point. If the matter stream does not impact the surface of the companion star, then the mass lost from the donor is expected to settle into a disc [7] and the division between the disc accretion and direct impact has been studied before ([8] [9] [10]). Torques exerted between the discs and the component white dwarfs allow angular momentum stored in the disc to be transferred back to the orbit ([7] [11]). However, the life time of these systems is defined not by feedback of angular momentum to orbit, but by angular momentum loss from the systems due to GR. If direct impact drives the system apart, both [9] and [10] showed that a stabilizing accretion disk is likely to be created. If direct impact mass transfer increases the mass ratio and decreases the orbital period, the mass transfer rate may eventually become dynamically unstable, which can result in a merger.

As we have showed in [12] henceforth called paper I that mass transfer phase in binary stellar evolution can either decrease or increase the orbital period of the system, crucially depending on the exchange of angular momentum between the binary components, the orbit and the component spins. In order to calculate the angular momentum changes during mass transfer, both the studies of [9] and [10] utilize a numerical prescription based on [13] approximations to more accurately determine the flow of angular momentum between the component spins and the orbit. In that formulation, it is assumed that the angular momentum transferred from the orbit to the spin of the accretor is exactly equal to the angular momentum of the ballistic particle in a circular orbit around the donor at its average radius during its motion from donor to accretor[1]. The present study will building upon these studies and crucially depending on the changes in the orbital angular momentum, the period and radius of the donor stars and that of its Roche lobe in response to the mass transfer, providing direct ballistic integrations of the mass transfer stream using an approximation adopted from the [13]. This led us to extend the analytical and numerical solution of [14] for the time dependent behavior of the mass transfer by relaxing most of the assumptions made to provide the problem manipulable. Here, we retain the simplifying assumption of Roche lobe calculation, but allow all the binary parameters to vary self-consistently.

The aim of this paper is to determine the evolution of angular momentum and orbital period changes between the component spins and the orbit in close DWD binaries throughout GR, tides and mass transfer effects by providing different range of orbital parameters and stellar models in a full self-consistent manner. In particular, we examine the comparison between numerical and analytical solutions to determine these systems whether, and under what circumstances, dissipative tidal coupling of the accretor to the orbit, through direct impact, can stabilize the dynamical mass transfer. This paper is organized as follows:

In Section (2) we develop the basic differential equations which governing the evolution of orbital parameters, assuming mass transfer through some well-specified model(s) and the basic assumptions with dynamical stability of mass transfer and discuss the difference between this method and the method utilized by the previous studies. In Section (3) we find and discuss the numerical solutions of the systems. In Section (4) we illustrate the results and discussion of this paper in comparison to the previous studies. Finally our main conclusion is summarized in Section (5).

[1][9] assume that the donor remains tidally locked, while [10] does allow for variation in the spin of the donor, but does not do so in a self-consistent manner.

2. Mass Transfer and Evolution of Orbital Parameters

2.1. Basic Assumptions

In this paper, we consider a close binary system of two white dwarfs with masses M_d and M_a, volume-equivalent radii of R_a and R_d, and uniform rotational angular velocities of Ω_a and Ω_d with axes perpendicular to the orbital plane for the accretor and donor, respectively[2]. We assume that the mass of each star is distributed spherically symmetrically. The binary is assumed to be in an initially circular keplerian orbit with orbital period, P_{orb}. The radius of each object is assigned following Eggleton's zero-temperature mass radius relationship of [13]. We chose the P_{orb} of the orbit such that the volume-equivalent radius of the mass of the donor (R_d) is equal to the volume-equivalent radius of its Roche lobe (R_L) as fit by [15]. Both the M_d and M_a initially rotate synchronously with the orbit[3].

2.2. Method

In this paper, we perform a Monte Carlo integration to calculate the volume-equivalent Roche lobe radius [16] over a two dimensional grid in P_{orb} and mass ratio, q parameter space. We also apply Runge-kutta methods for numerically estimating solutions to basic differential evolution equations of obit, which will be discussed in Section (3). Hence, we determine the set of orbital parameters and their differential equations which governs the evolution of angular momentum and orbital period changes due to direct impact accretion in close DWD binaries, using the Eggleton function for the Roche lobe, $R_{L,E_{gg}}$ for calculating its size, the dynamical mass transfer rate, and the corresponding synchronization time scales for different cases, under certain restrictive approximations which determine the strength of tidal coupling. We now have all the steps in place to solve the evolution of these systems.

Our basic calculations are performed using a Monte Carlo integration method in a stationary inertial reference frame located at the initial center of mass of the binary system, which solving ordinary differential equations of orbital parameters at equivalent points. Following the above assumptions, we can investigate the outcomes for these systems with total mass, M and the orbital parameters such as P_{orb}:

$$P_{orb} = \left(\frac{4\pi^2 a^3}{GM}\right)^{1/2}, \tag{1}$$

where G and a are the universal gravitational constant and semi-major axis, respectively, and taking the donor to be the less massive star, the one that fills its Roche lobe.

2.3. Evolution of Angular Momentum

As we have investigated in [12], as the matter is being transferred between the

[2]Throughout this paper, the subscripts "a" and "d" will correspond to the accretor and donor, respectively.

[3]If the donor rotates non-synchronously, the Roche lobe radii can be calculated as given in [16].

components in the binary systems, not only the mass ratio, q, but also the P_{orb} will be changed due to angular momentum redistribution between the components of two stars. Then the total angular momentum, J_{tot}, of the binary system is given by:

$$J_{tot} = J_{orb} + \sum_{i=1}^{2}\left(J_{spin,i}\right); \quad i \in (a,d) \tag{2}$$

where J_{orb} is the orbital angular momentum, which is given by:

$$J_{orb} = M_a M_d \left(\frac{Ga}{M}\right)^{1/2}, \tag{3}$$

and the spin angular momenta of the accretor and donor are $J_{spin,a} = K_a M_a R_a^2 \Omega_a$ and $J_{spin,d} = K_d M_d R_d^2 \omega_d$, respectively, where K_a and K_d are dimensionless constants depending upon the internal structure of the accretor and donor, respectively.

Here, we express the total angular momenta in terms of the rotational rates of the accretor, f_a and donor, f_d relative to the orbital angular velocities of the stars. Thus the rotational angular velocities of the stars, Ω_i can be written in terms of the rotational rates and the angular velocity of the circular orbit, Ω_{orb} is given by

$$\Omega_i = f_i \Omega_{orb}. \tag{4}$$

Then we can rewrite the total angular momentum of the binary system as:

$$J_{tot} = M_a M_d \sqrt{\frac{Ga}{M}} + \sum_{i=1}^{2}\left(K_i M_i R_i^2 f_i\right)\Omega_{orb}. \tag{5}$$

The form of the J_{orb} term adopted above assumes the binary revolves at the Keplerian angular velocity of the circular orbit, $\Omega_{orb}^2 = GM/a^3$, which is a good approximation if the stars are centrally condensed.

Here, we introduce three effects that change the J_{orb}, P_{orb} and Ω_i over time: mass transfer (MT), tides, and GR. Assuming each effect is independent of the others, we can then write the change of the orbital angular momentum as the sum of the change due to each of the above effects:

$$\dot{J}_{orb} = \dot{J}_{orb,MT} + \dot{J}_{orb,GR} + \sum_{i=1}^{2}\left(\dot{J}_{orb,tides,i}\right), \tag{6}$$

which is known as the orbital angular momentum balance equation. To determine the total change in the angular momentum, then, we simply need to write the change due to each of the above effects. A system of two point masses orbiting around each other, in circular orbits, radiates gravitationally ([17]). Then the change in orbital angular momentum due to GR for a circular orbit is given by:

$$\dot{J}_{orb,GR} = -\left(\frac{32}{5}\frac{G^3}{c^5}\frac{M_a M_d M}{a^4}\right) J_{orb}. \tag{7}$$

Prior to the onset of mass transfer, we assume that the spins and orbit to be synchronized, the binary orbit will shrink and the P_{orb} of the system will decrease due to the effect of angular momentum via GR as seen in Equation (7). During this time, tidal coupling will act to circularize the binary as well as synchronize the spins of the stars with the orbit. As mass transfer begins, angular momentum will be exchanged between the spin of the component stars and the orbit. This will ultimately affect the dynamical stability of the mass transfer process. As in [10], we express the exchange of orbital angular momentum due to tides as:

$$\dot{J}_{orb,tides} = \sum_{i=1}^{2}\left(\frac{K_i M_i R_i^2}{\tau_i}\left(f_i - 1\right)\Omega_{orb}\right). \tag{8}$$

The term in the bracket of Equation (8) represent the torque due to dissipative coupling upon the accretor and donor. Hence, torques are parameterized in terms of the synchronization time scales ([18]) of the accretor, τ_a, donor, τ_d and are linearly proportional to the difference between the component and the orbit spin, which determines the strength of tidal coupling relative to MT and GR. We assume that the tidal synchronization time scales change because the masses and stellar radii relative to the orbital period are changing. As [10], we explore two different values for the synchronization time scale at contact: $\tau = 10^{15}$ years (very weak tidal coupling) and $\tau = 10$ years (very strong tidal coupling), which may be a better approximation for systems with short orbital periods, as we consider in our analysis.

In this work, we are only interested in direct impact mass transfer and orbital changes due to ballistic integrations where the particle impacts the surface of the accretor within one orbital period. In this case, the evolution of orbital parameters is determined by the differential equations, which will be given in Section (2.4). If the particle accretes within one orbital period, we classify this as a direct impact. If the particle does not accrete within one orbital period, it is likely that the ejection stream from the donor will self-intersect, resulting in the eventual formation of an accretion disk.

To determine $\dot{J}_{orb,MT}$, we use the ballistic mass transfer calculations of [19] to examine the instantaneous effect of mass transfer in close DWD binary systems. This method uses a fully self-consistent, conservative, ballistic model of the transferred mass to determine the orbital parameters of the system after a single mass transfer event. Then, the change in the orbital parameters per unit mass that results is directly proportional to the mass transfer rate of our evolving DWD, $\dot{M}_d$:

$$\dot{J}_{orb,MT} = \left(\frac{\Delta J_{orb,b}}{M_P}\right)\dot{M}_d, \tag{9}$$

where $\Delta J_{orb,b}$ is the change in the orbital angular momentum for a close DWD binaries as calculated by the above ballistic model for a single mass transfer event ejecting a particle of mass M_P. In this method, changes in $J_{orb,MT}$ are calculated at each time step by integrating the three-body system consisting of the two stars and the discrete particle representing the mass transfer stream. The change in the $J_{orb,MT}$ per unit mass transferred is independent of the mass of the ejected particle as long as $M_P \ll M_d, M_a$.

2.4. Differential Equations for the Evolution of Orbital Parameters

As we investigated the rate of change of orbital angular momentum in Section (2.3), we develop the equations for the evolution of orbital period and the rotational angular velocities of the stars. It follows from Equation (3) and [12] that

$$\frac{\dot{J}_{orb}}{J_{orb}} = (1-q)\left(\frac{\dot{M}_d}{M_d}\right) + \frac{1}{3}\frac{\dot{P}_{orb}}{P_{orb}} \tag{10}$$

for conservative mass transfer $(\dot{M} = 0)^4$ and $q = \frac{M_d}{M_a}$. Since $\dot{M}_a = -\dot{M}_d$.

Hence for the conditions M = constant and J_{orb} = constant it then follows that:

$$\frac{\dot{P}_{orb}}{P_{orb}} = -3\left(\frac{\dot{M}_a}{M_d}\right)(q-1) > 0. \tag{11}$$

2.4.1. Evolution of the Orbital Period

We examine the changes of the P_{orb} due to dynamical mass transfer, tides and GR. We assume that each effect is independent, and write the total change in the P_{orb} due to each of the above effects, respectively, as:

$$\dot{P}_{orb} = \dot{P}_{orb,MT} + \dot{P}_{orb,GR} + \sum_{i=1}^{2}\left(\dot{P}_{orb,tides,i}\right). \tag{12}$$

To calculate $\dot{P}_{orb,MT}$, we utilize the model for mass transfer developed in [19]. Using this models, we calculate the time rate of change of P_{orb} due to mass transfer rate as:

$$\dot{P}_{orb,MT} = \left(\frac{\Delta P_{orb,b}}{M_P}\right)\dot{M}_d. \tag{13}$$

Here, $\Delta P_{orb,b}$ is the change in the orbital period for a close DWD binaries as calculated by the above ballistic model of [19] as described in Section (2.3) for the evolution of orbital angualar momentum.

Next we calculate $\dot{P}_{orb,tides}$ and $\dot{P}_{orb,GR}$. As noted by [9] and [10], we used a different metric for changing the spin angular momentum due to tides of Equation (8). Hence we develop $\dot{P}_{orb,tides}$ from that angular momentum change. Holding the donor mass constant ($\dot{M} = 0$) for the final two terms of Equation (12) we can combine Equation (6) with Equation (11) to obtain:

$$\dot{J}_{orb,tides} + \dot{J}_{orb,GR} = \left(\frac{1}{3P_{orb}}\left(\dot{P}_{orb}\right)_{tides,GR}\right)J_{orb}, \tag{14}$$

where $\left(\dot{P}_{orb}\right)_{tides,GR}$ is the total change of the orbital period due to the combined effects of tides and GR. Assuming as before that changes to the orbital period due to tides and changes due to GR are independent we can rewrite the above as:

[4] Recall that we assume the orbit remains circular in this paper.

$$\dot{J}_{orb,tides} + \dot{J}_{orb,GR} = \left(\frac{\dot{P}_{orb,tides}}{3P_{orb}} + \frac{\dot{P}_{orb,GR}}{3P_{orb}} \right) J_{orb}. \tag{15}$$

Using Equation (3), Equation (7), and Equation (8), it follows that:

$$\dot{P}_{orb,tides} = \frac{3P_{orb}}{\mu\sqrt{GaM}} \sum_{i=1}^{2} \left(\frac{K_i M_i R_i^2}{\tau_i} \omega_i \right), \tag{16}$$

and

$$\dot{P}_{orb,GR} = -\frac{96}{5} \frac{G^3}{c^5} \frac{M_a M_d M}{a^3}. \tag{17}$$

From Equation (4) and Equation (8) we can re-write Equation (16) as

$$\dot{P}_{orb,tides} = \frac{3}{\mu \left(P_{orb} M^2 \right)^{1/3}} \left(A_a + D_d \right), \tag{18}$$

where

$$A_a = \frac{K_a M_a R_a^2}{\tau_a} \left(\frac{\Omega_a - \Omega_{orb}}{\Omega_{orb}} \right),$$

and

$$D_d = \frac{K_d M_d R_d^2}{\tau_d} \left(\frac{\Omega_d - \Omega_{orb}}{\Omega_{orb}} \right). \tag{19}$$

Finally, inserting Equation (13), Equation (17), & Equation (18) into Equation (12) leads to the equation for the dynamical evolution of the orbital period with time as:

$$\dot{P}_{orb} = \left(\frac{\Delta P_{orb,b}}{M_P} \right) \dot{M}_d + \frac{3\left(A_a + D_d \right)}{\mu \left(P_{orb} M^2 \right)^{1/3}} - \dot{P}_{orb,GR}. \tag{20}$$

2.4.2. Evolution of the Rotational Angular Velocities of the Stars

We derive the equations for the evolution of the components spins, Ω_a and Ω_d. Thus the changes in both components can be defined as:

$$\dot{\Omega}_i = \dot{\Omega}_{i,MT} + \dot{\Omega}_{i,tides} + \dot{\Omega}_{i,GR}. \tag{21}$$

Analogous to $\dot{P}_{MT}$ in Equation (13), the change in Ω_i due to mass transfer, $\dot{\Omega}_{i,MT}$ can be expressed as:

$$\dot{\Omega}_{i,MT} = \left(\frac{\Delta \Omega_{b,i}}{M_P} \right) \dot{M}_d. \tag{22}$$

Here, $\Delta\Omega_{b,i}$ is the change in the rotational angular velocities of the star i resulting from a single mass transfer as described in Section (2.3). As in Equation (4), the spin angular momentum of each component can be written as:

$$J_{spin,i} = K_i M_i R_i^2 \Omega_i, \tag{23}$$

where $\Omega_i = f_i \Omega_{orb}$. Hence, we consider that the tidal forces exist to redistribute angular momentum, working to keep the spins of the donor and accretor synchronous with the orbit ($f_i = 1$). Now we can determine $\dot{\Omega}_{i,tides}$ and $\dot{\Omega}_{i,GR}$ by differentiating Equation (22) with respect to time assuming the mass held constant:

$$\dot{J}_{spin,i} = K_i M_i R_i^2 \left(\dot{\Omega}_{i,tides} + \dot{\Omega}_{i,GR}\right) - \frac{2}{3} K_i M_i R_i^2 \frac{\Omega_i}{P_{orb}} \left(\dot{P}_{tides} + \dot{P}_{GR}\right). \tag{24}$$

The second term in Equation (24) depends only upon changes due to tides and GR. Since we do not include any GR effect on the spin angualar momentum of the components, conservation of angular momentum indicates that any changes in the spin angualar momentum of a component must be equal and opposite to the changes in the orbital angular momentum of the system due to tides acting on that component. Using Equation (4) and Equation (8), we have:

$$\dot{J}_{spin,i} = -\sum_{i=1}^{2} \frac{K_i M_i R_i^2}{\tau_i} \left(\Omega_i - \Omega_{orb}\right). \tag{25}$$

By combining Equation (24) and Equation (25) we can derive the expression for $\dot{\Omega}_{i,tides} + \dot{\Omega}_{i,GR}$ as:

$$\dot{\Omega}_{i,tides} + \dot{\Omega}_{i,GR} = -\frac{\Omega_i}{\tau_i} \frac{2}{3} \frac{\Omega_i}{P_{orb}} \left[-\beta_{GR} + \frac{3\left(A_a + D_d\right)}{\mu\left(P_{orb} M^2\right)^{1/3}} \right], \tag{26}$$

where

$$\beta_{GR} = \frac{96 G^3 M_a M_d M}{5 c^5 a^3}. \tag{27}$$

Using Equation (21), Equation (22) and Equation (26) we obtain the equations for the evolution of Ω_a and Ω_d as:

$$\dot{\Omega}_a = \left(\frac{\Delta\Omega_{b,a}}{M_P}\right) \dot{M}_d - \frac{\Omega_a}{\tau_a} + \frac{2}{3} \frac{\Omega_a}{P_{orb}} \left[-\beta_{GR} + \frac{3\left(A_a + D_d\right)}{\mu\left(P_{orb} M^2\right)^{1/3}} \right], \tag{28}$$

and

$$\dot{\Omega}_d = \left(\frac{\Delta\Omega_{b,d}}{M_P}\right) \dot{M}_d - \frac{\Omega_d}{\tau_d} + \frac{2}{3} \frac{\Omega_d}{P_{orb}} \left[-\beta_{GR} + \frac{3\left(A_a + D_d\right)}{\mu\left(P_{orb} M^2\right)^{1/3}} \right], \tag{29}$$

2.5. Mass Transfer Rate

The nature of mass transfer and its stability is very important in a close DWD binaries. It is rooted in a similar treatment of mass transfer under consequential angular momentum losses via GR [20]. Whether, once started, mass transfer will proceed in a stable or dynamically unstable manner depending on the response of the mass losing donor star and its Roche lobe to the mass transfer. For all types of donor star, the mass transfer rate is a strong function of the depth of contact, defined here as the amount by which the donor overflows its Roche lobe as:

$$\Delta = R_d - R_L, \tag{30}$$

where R_d is the radius of the donor and R_L is the radius of its Roche lobe. The mass loss rate from the donor monotonically increases with Δ. The way in which the mass transfer rate varies with Δ has been investigated in many analyses (see, for example, [21] [22] [23]). The correct way to treat this is to compute the stellar structure ([23]). In accordance with [9], we approximate the mass transfer as adiabatic ([24]). In the adiabatic response, which for a white dwarf donor gives a mass transfer rate of

$$\dot{M}_d = -f\left(M_a, M_d, a, R_d\right)\Delta^3, \tag{31}$$

for $\Delta > 0$, and zero for $\Delta < 0$. Combining results from [24] [25] and [22], the function *f* is given by:

$$f\left(M_a, M_d, a, R_d\right) = \frac{8\pi^3}{9}\left(\frac{5Gm_e}{h^2}\right)^{3/2}\frac{\left(\mu_e' m_n\right)^{5/2}}{P_{orb}}\Lambda, \tag{32}$$

where $\Lambda = \left(3\mu M_d / 5 r_L R_d\right)^{3/2}\left[a_d\left(a_d - 1\right)\right]^{-1/2}$, m_e is the mass of an electron, m_n is the mass of a nucleon, μ_e' is the mean number of nucleons per free electron in the outer layers of the donor (which we will assume to be two) and μ and a_d are parameters associated with the Roche potential

$$\mu = \frac{M_d}{M_a + M_d} \quad \text{and} \quad a_d = \frac{\mu}{X_{L1}^3} + \frac{1-\mu}{\left(1 - X_{L1}\right)^3}. \tag{33}$$

where, X_{L1} is the distance from the center of the donor to the inner Lagrangian point of the donor, in units of the semi-major axis, *a*.

2.6. Roche Model

In the case of [9], where the rotational angular velocity of the donor is fixed to the orbital velocity and the orbit is circular throughout, the shape and volume of the Roche lobe depends only upon the mass ratio and the semi-major axis of the system. For higher mass ratio, stars become more and more deformed. Thus mass transfer is dynamically unstable. In that case, we introduce the effective radius, r_L, of the Roche lobe, the most widely used approximation being from [15],

$$r_L = \frac{0.49q^{2/3}}{0.69q^{2/3} + \log\left(1 + q^{1/3}\right)}, \tag{34}$$

effectively, it is a tidal radius where mean density in lobes are equal:

$$R_L = r_L a, \tag{35}$$

for $0.1 \le q \le 1$ and so with the notation of [9], we have

$$\frac{\dot{R}_L}{R_L}=\zeta_{r_L}\frac{\dot{M}_d}{M_d}+\frac{2}{3}\frac{\dot{P}_{orb}}{P_{orb}}, \tag{36}$$

where ζ_{r_L} takes values between 0.33 and 0.48 is the logarithmic derivative of r_L with respect to M_d for both [26] and [15] small q approximation for the Roche lobe radius. In the same spirit we write the logarithmic time derivative of the donor radius, $R_d \equiv R_d(M_d,t)$ as:

$$\frac{\dot{R}_d}{R_d}=D+\zeta_{ad}\frac{\dot{M}_d}{M_d}, \tag{37}$$

where $D=\left(\partial\log(R_d)/\partial\log(\partial t)\right)_{M_d}$, represents the rate of change of the donor radius due to intrinsic processes such as thermal relaxation and nuclear evolution, whereas ζ_{ad} usually describes changes resulting from adiabatic variations of M_d [27]. If the donors are degenerate as in the white dwarf case, ζ_{ad} is simply obtained from the equilibrium mass radius relationship for the donor[5]. As ζ_{ad} and ζ_{r_L} are both monotonic functions of mass loss, it is a sufficient condition that mass transfer be stable at the onset of Roche lobe overflow in order to ensure dynamical stability of mass transfer, which depends on the tidal coupling between the accretor and the orbit undergoing direct impact accretion. The larger ζ_{ad}, the more stable the mass transfer is. To consider stability in detail, we will use the linear stability analysis following ([11] [28]).

3. Numerical Solutions

We integrate numerically the orbital evolution Equation (2), Equation (4), Equation (6), Equation (11), Equation (20), Equation (28), Equation (29), Equation (31), Equations (35)-(37) using 6th and 8th order Runge-Kutta ordinary differential equation solver [29], allowing the binary parameters to adjust self-consistently. We consider that the orbital angular momentum of the system are conserved throughout the integration over the entire parameter space. Specifically, we compute the angular momentum and orbital period changes between the component spins and orbit in close DWD binaries undergoing mass transfer through direct impact of the transfer stream, allow the binary separation to change and compute the values of ζ_{ad} as it evolve. Here, we use Eggleton's approximation of the zero-temperature mass radius relationship cited by [13] and [9], which is a good approximation for systems containing white dwarfs. Also, a ζ_{ad} significantly different from −0.33 clearly affects the stability and evolution of the systems at the onset of mass transfer, and can lead to shrinking orbits even if the mass transfer is stable with $\dot{M}_d=0$. In our subsequent analysis, where we are concerned about the long term integrations of the orbital evolution equations, we set $\left(\partial\log R_d/\partial t\right)_{M_d}=0$ and use the zero-temperature mass-radius relationship.

[5]The radius of each object is assigned following Eggleton's zero temperature mass radius relation ([13]). We assume that both the donor and accretor initially rotate synchronously with the orbit.

In our integrations, we need to either assume or determine from other assumptions how the mass and angular momentum are redistributed in a close DWD binary system during mass transfer. This depends on the mode of accretion appropriate for the binary considered: does the stream impact the accretor or is an accretion disk present; is the mass transfer sub-Eddington and conservative, or are mass and angular momentum being ejected from the system following super-Eddington mass transfer. For most of the numerical integrations that follow, we use the appropriate rate of change of orbital angular momentum due to GR, MT and tides. However, if one is interested in the relatively rapid phases of dynamical mass transfer that follow contact and onset, then the qualitative properties of our integrated evolutions depend strongly on these assumptions.

Figure 1 shows the evolution of the orbital period and angular momentum conservation with their spin angular momentum of the accretor and donor in close DWD binaries over the entire parameter space of interest for integrations that calculated using the Eggleton approximation for the Roche model. In this result, we are only interested in direct impact mass transfer where the particle impacts the surface of the accretor within the orbital periods. Compared to direct impact accretion, disc accretion is provide a basic mechanism for redistributing spin angular momentum in the accretor back into the orbit through tidal coupling in [7]. As a result, it is likely that once a system enters a phase of disc accretion it will remain in this phase or perhaps even become detached as the orbital period continues to grow and the mass ratio decreases due to continued mass transfer. Thus if a disk is formed at any point the integration stops and the system is assumed to be stable throughout its lifetime.

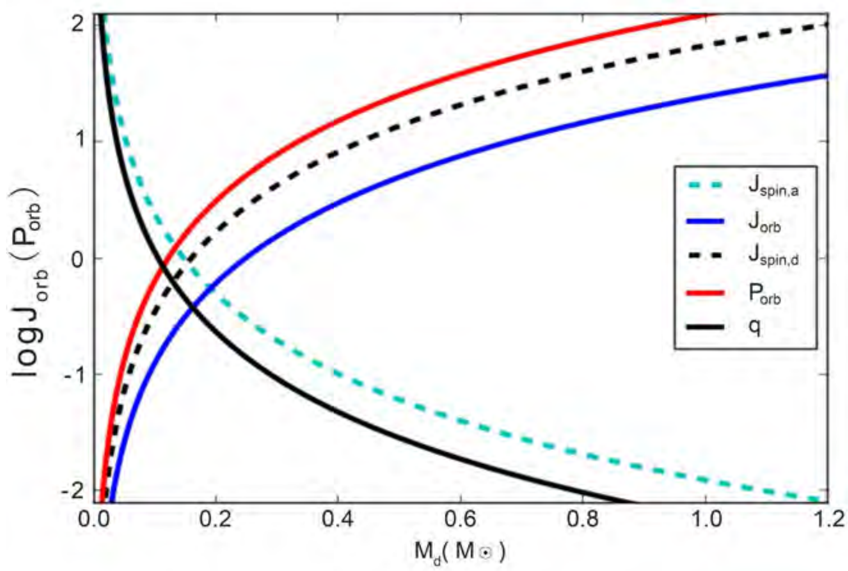

Figure 1. The evolution of orbital period and angular momentum conservation with their $J_{spin,a}$ and $J_{spin,d}$ over entire close DWD binary system, which obtained using the Eggleton approximation from Equation (5) for the calculation of the Roche lobe overflow and rapid mass transfer stream.

As a system evolves, it is possible to pass back and forth through phases of mass transfer and phases of no mass transfer as the orbital period and the two masses change. If P_{orb} increases enough for mass transfer to stop altogether, the integration proceeds (with $\dot{M}_d = 0$) until the action of GR shrinks the orbit sufficiently for mass transfer to resume rather than the analytical one. We integrate over a period of 1.25 G yr. As in [9], if $\dot{M}_d$ less than $0.1M_{\odot}\text{yr}^{-1}$ at any point during the integration, the integration continued and the system is desired as dynamically stable.

In **Figure 2** we show the approximate adiabatic mass radius exponent, ζ_{ad} from Equation (37) using the Eggleton's approximation of the zero-temperature mass radius relationship [13] for stars with initial masses from $0.12M_{\odot} - 0.78M_{\odot}$ and the corresponding mass radius relations. These were calculated by assuming a constant mass loss rate of $10^{-5}M_{\odot}\text{yr}^{-1}$. The large initial values for ζ_{ad} imply that the star has to lose very little mass to shrink significantly. This simply represents the fact that, in these systems, a large fraction of the envelope contains very little mass.

3.1. Angular Momentum and Orbital Period Changes Due to Direct Impact Accretion

In this section, we investigate the numerical integrations for the change in the evolution of orbital angular momentum per unit transferred mass, which is independent of the mass of the ejected particle as long as $M_P \ll M_d$ from Equation (9) following a single ballistic orbit as a function of the donor mass for white dwarfs undergoing direct impact mass transfer. **Figure 3** shows the evolution of orbital angular momentum change per unit transferred mass, $\dot{J}_{orb,MT}$ and period changes from Equation (9) and Equation (11), respectively, with the less massive donor and the massive accretor stars. Hence, we compared the results of

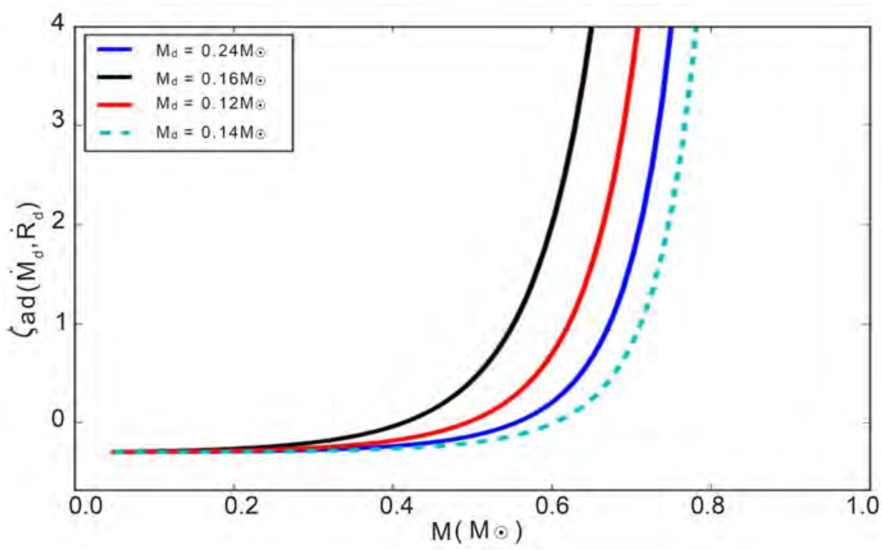

Figure 2. Results of the approximate adiabatic mass radius exponents over the total mass of the system for evolved stars of initial masses $0.12M_{\odot}$, $0.14M_{\odot}$, $0.16M_{\odot}$, $0.24M_{\odot}$.

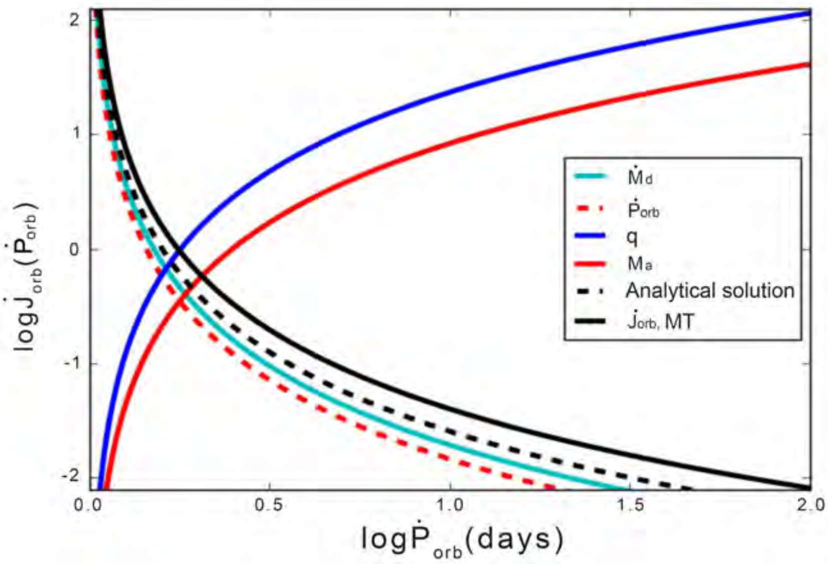

Figure 3. The $\dot{J}_{orb,MT}$ per unit transferred mass correspond to variations in the mass of accretor and mass ratios of the systems versus $\dot{P}_{orb}$. Here, in our calculation the region above the $\dot{J}_{orb,MT}$ shows the unstable mass transfer whereas the region below the $\dot{M}_d$ shows the stable mass transfer. Hence, the dashed black line represents the analytical solution between these stable and unstable systems.

the $\dot{J}_{orb,MT}$ and $\dot{M}_d$ due to direct impact accretion with the $\dot{P}_{orb}$ and M_a. As expected, our numerical results agree quite well to this analytic solution.

In Figure 4 we investigate a single ballistic integration as a function of the masses of the donor and accretor. The solid blue and dashed black lines above a solid cyan line are a region corresponds to systems that undergo direct impact and reach stable configuration, while below this solid cyan line such as solid black and dashed red lines are a region corresponds to systems that undergo deformation. The solid cyan line between these two regions shows the analytical solution to this region, which was first derived and presented by [6] [9]. Thus, the change in the orbital angular momentum appears to become more positive with increasing donor mass. Following them, we calculate this line by taking the distance of closest approach for a ballistic integration given by [30]; as analytically fit by [6] and setting it equal to the radius of the accretor (as given by Eggleton's zero temperature mass radius relationship of [13]. In calculating this line, we assume the donor (also described by the same zero temperature mass radius relationship) completely fills its Roche lobe ([15]).

Following the above consideration, we show the orbital angular momentum changes per unit transferred mass in the parameter space of close DWD binaries with a low donor mass are more likely to remain stable over long periods of time, while the majority of the parameter space is expected to be unstable. Thus, we further investigate these parameter space from deformation to direct impact where the orbital angular momentum decreases more rapidly than previous studies, which shown as in solid red line.

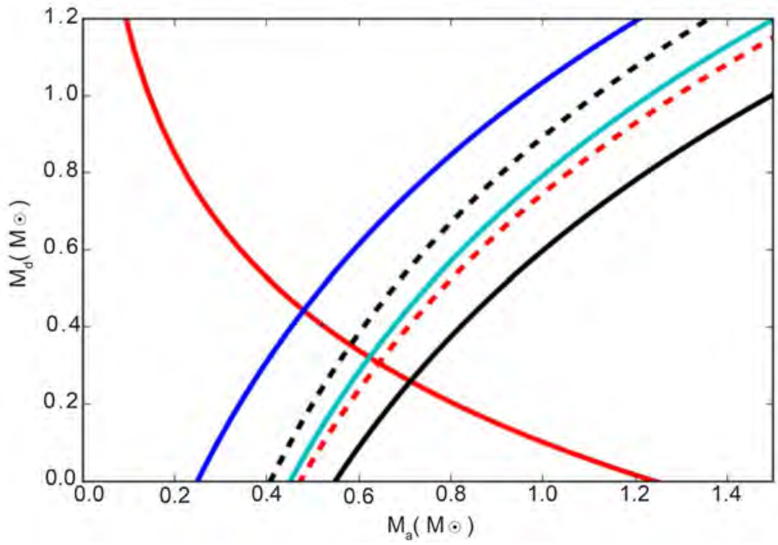

Figure 4. Result of a single ballistic integration as a function of the masses of the donor and accretor, which undergoing direct impact accretion from Equation (9).

3.2. Evolution of Systems with Strong Tidal Coupling

It is commonly assumed ([9]; but see also [10]) that the rotational angular velocity of the donor will remain synchronized with the angular velocity of the circular orbit. This is generally expected since Roche lobe overflow requires extreme tidal distortions in the donor star which act to synchronize its rotational angular velocity on short time scales. The accretor is generally not affected as strongly by tidal synchronization since, being more massive, it is not expected to be significantly tidally distorted. Some tidal coupling between the donor and the orbit is generally assumed, though it is not expected to be strong enough to keep the accretor from becoming a rapid rotator.

In Figure 5 we present the orbital parameters of the tides with initial tidal synchronization time scale of $\tau = 10\ \text{years}$: 1) the evolution of the rate of change of the spin angular momenta per unit transferred mass of the the donor ($\dot{J}_{spin,d}$, for $\Omega_d = 0.25$) and accretor ($\dot{J}_{spin,a}$, for $\Omega_a = 0.8$) from Equation (25), 2) the evolution of the rate of change of orbital angular momentum and period corresponds to the mass transfer rate from Equation (10) and Equation (31), respectively, and 3) the effective Roche lobe radius of the donor stars, which shows the end evolution of Roche lobe overflow. In general, systems with a smaller mass conserve orbital angular momentum better than systems with a higher mass. Systems where the orbital angular momentum conservation is larger tend to be systems where the numerical integration runs for many orbits, allowing systematic errors in the numerical integration to accumulate. Even so, all systems presented in this paper conserve mass and orbital angular momentum to better than 1% throughout the entire evolution.

4. Results and Discussion

As we developed and discussed the basic equations for the evolution of orbital

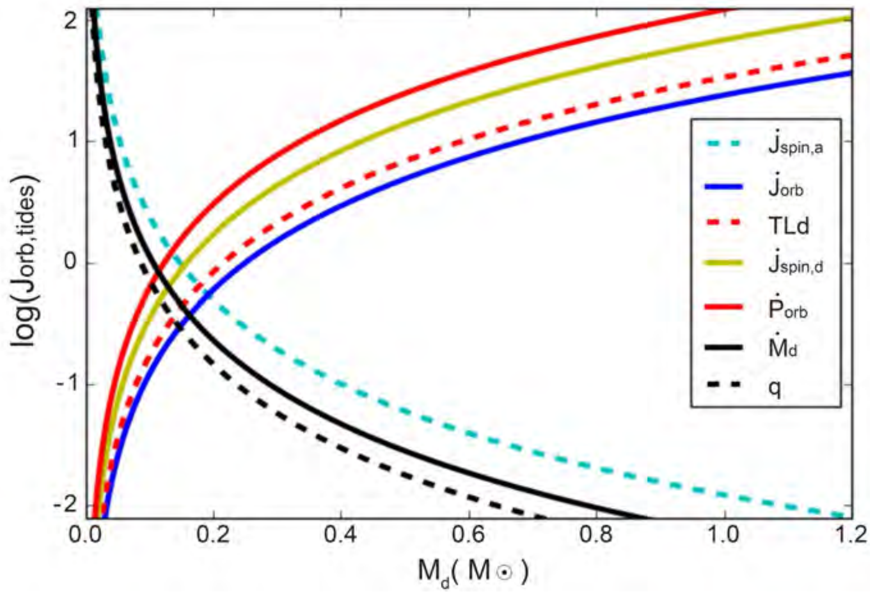

Figure 5. Results of evolution for the orbital parameters of the tides generating body with initial tidal synchronization time scale of $\tau = 10$ years using the Eggleton approximation for the Roche lobe that can be calculated from Equation (8), Equation (10), Equation (25) and Equation (31). It shows the rate of change of orbital angular momentum between the donor and the orbit, *i.e.*, the $\dot{J}_{spin,d}$, and $\dot{J}_{spin,a}$ correspond to the rotational angular velocities of the donor and accretor, respectively. Here, the rotational angular velocity of the donor's, $\Omega_d = 0.86$ remains synchronized to the rotational angular velocity of the circular orbit, $\Omega_{orb} = 1.25$. Hence, we assume the angular momentum that would be removed from the spin of the donor is immediately returned from the orbit.

parameters in Sections (2) and (3), respectively, we compute the evolution over a grid in M_d, M_a and P_{orb} parameter space for two different tidal synchronization time scales at contact: $\tau = 10^{15}$ years and $\tau = 10$ years to determine the dynamical stability of various systems. We also elaborate the comparisons between numerical and analytical solutions for the evolution of angular momentum and orbital period changes due to direct impact accretion in close DWD binaries by various stellar model approximations of mass transfer, with particular attention payed to the dynamical stability of these processes against runaway on synchronization time scales of the mass donating star.

4.1. Evolution of Systems Using Eggleton Roche Lobe

As we discussed in Section (3), Figure 5 shows the end result of systems with an initial synchronization time scale of $\tau = 10$ years using $R_{L,Egg}$. Assuming that once a disc is reached, the system will remain stable for the remainder of its evolution, therefore we stop the integration once a disc is formed. However, with the exception of dynamically unstable systems, the evolution of all systems in this plot is stopped when the system reaches a phase of disc accretion. The time it takes to reach this phase of disc accretion varies from system to system.

As noted by [10] that allowing the spin of the donor to vary and by including the resulting effects of tidal coupling between the donor's spin and the orbit, the number of stable systems increased compared to the analysis of [9]. Hence, the main difference between our analysis and that of [10] is in the treatment of the way we manage the evolution of angular momentum and orbital period changes during the direct impact accretion process. In observing the increase in the number of stable systems compared to the analysis of [10], we conclude that by utilizing a mass transfer treatment that allows the rotation rates corresponds to rotational angular velocities of both components to vary and self-consistently accounts for the exchange of angular momentum between the spins of the components and the orbit, we are able to increase the number of stable systems.

Stronger tidal coupling will allow more spin angular momentum from the accretor to be transferred back into the orbit, which correspondingly slower increase in orbital period, causing the mass transfer rate and the rate of change of orbital angular momentum to decrease. This is to be expected and in agreement with the analyses of [10] and [9]. This results in an increase the stability of the systems in general.

In **Figure 5** we have presented the dynamically stable mass transfer with increasing orbital period, but decreasing the mass ratio of the systems. However, in **Figure 6** we have presented the dynamically unstable mass transfer with rapid increase in the orbital period for $\tau = 10^{15}$ years is a direct result of the conservation of angular momentum: the angular momentum lost during the spin down and mass loss of the donor is greater than the angular momentum gained by the accretor. The net decrease in spin angular momentum corresponds to an increase in the orbital angular momentum, increasing the orbital period. The mass transfer rate increases rapidly as the mass loss from the donor causes the radius

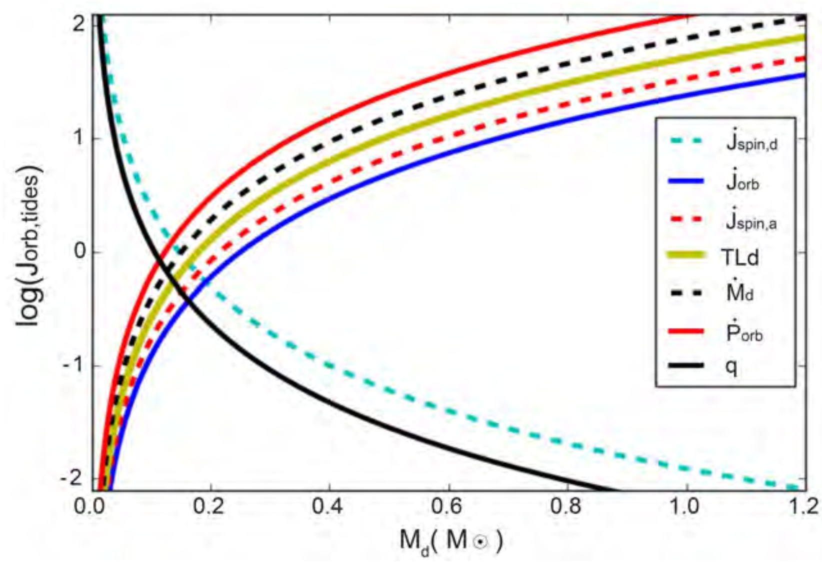

Figure 6. Same as in **Figure 5**, but with $\tau = 10^{15}$ years using $R_{L,Egg}$ for the Roche lobe calculation. In this result, we observe that the P_{orb} increases due to the effect of tides. As a result $\dot{M}_d$ increases rapidly and the accretor spin increases significantly.

to increase, even as the Roche lobe grows due to the increasing orbital period (see, e.g., Equation (30) and Equation (31)). Thus, we present the results of evolution for the orbital parameters of the tides generating body with tidal synchronization time scale of $\tau = 10^{15}$ years. Here, we acknowledge the main limitation of our result to assume that systems are stable once they reach a phase of disc accretion. Systems with the less masses of the donor stars parameter space of interest here begin the integration in a disc phase, and are therefore labeled as stable. However, it is feasible that if these high donor mass systems were allowed to evolve through the initial disc phase, they would eventually become super-Eddington and potentially dynamically unstable.

4.2. Comparison of System Evolution with analytical Solutions

We have computed different orbital parameters of close DWD binaries and their evolution with synchronization time scales using $R_{L,Egg}$. Hence, for $\tau = 10^{15}$ years, the system is dynamically unstable and for $\tau = 10$ years the system is stable, but passes through a phase of super-Eddington accretion. In this section, we compare the analytical solutions of the various orbital parameters of these systems with the numerical solution that we investigated in Sections (3) and (4).

The rotational angular velocities of the component white dwarfs remain closer to synchronize. In our work, when we apply the $R_{L,Egg}$, the mass transfer rate will continue to increase until tides have transferred sufficient angular momentum from the spin of the components to the orbit to expanded the orbit and decrease the mass transfer rate. Thus, the mass transfer rate is decreased and tides continue to redistribute angular momentum between the component spins and the orbit (see, **Figure 5**). In **Figure 7** we show the evolution of the mass radius relationship using the Eggleton approximation for the Roche lobe calculation. We also determine the evolution of the orbital period changes on a much longer time scale for the $R_{L,Egg}$ numerical solution than the analytical solution. This is due to the fact that, as mass transferred from the donor to the accretor, the mass ratio q and the mass of the donor decreases relative to the orbit and the radius and mass of the accretor increases. These were calculated by assuming the constant mass loss rate of $1.25\times10^{-5} M_{\odot}\,\mathrm{yr}^{-1}$.

In **Figure 8** we show the evolution of orbital parameters (*i.e.*, the mass of the donor as a function of mass ratio) due to direct impact accretion. Hence, the solid blue line also indicates the deformed donor star at different moments in time. The solid green line show the evolution of orbital parameters for both synchronization time scales over which the mass transfer rate changes in Equation (31) for the non-deformed donor star whereas the dotted gray line is the deformed donor star and it is analytical solution, wich shows the evolution of the Roche lobe overflow. In general, the peak of solid gray, red, green, and blue lines indicate the evolution of the Roche lobe overflow in close DWD binaries through direct impact.

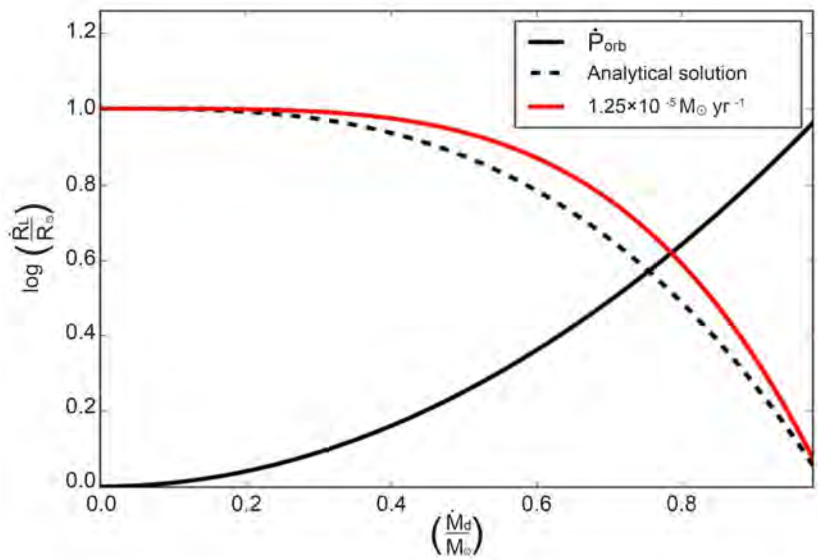

Figure 7. Result of the comparison between the numerical integrations and analytical solution for the evolution of the Roche lobe radius as a function of the mass of the donor stars for $\tau = 10$ years with initial masses of $M_d = 0.12M_\odot$ and $M_a = 0.8M_\odot$ in a close DWD binary system. Hence 10^3 years of evolution with solution obtained using $R_{L,Egg}$ for the calculation of the Roche lobe.

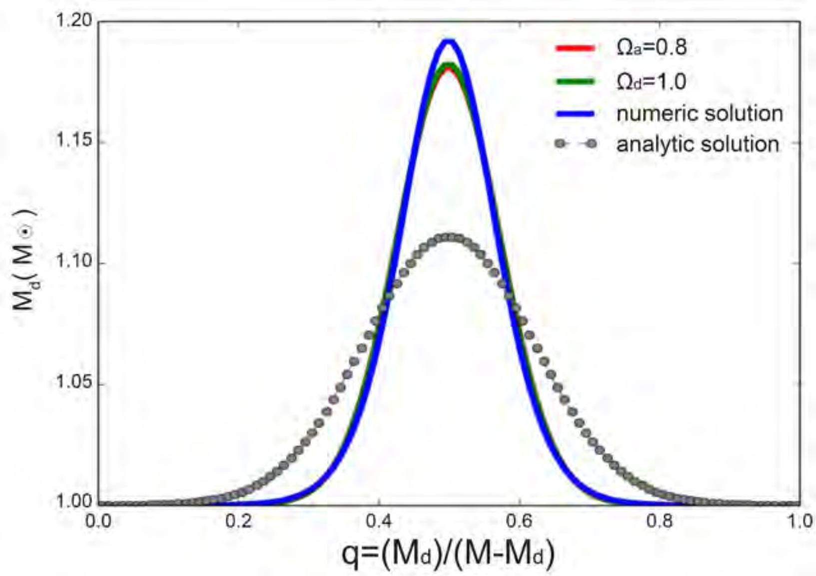

Figure 8. Results of the comparison between the numerical integrations and analytic solutions for the evolution of orbital parameters, *i.e.*, $M_d(M_\odot)$ versus the mass ratio, q with the rotational angular velocities of the donor, Ω_d and accretor, Ω_a on the Roche lobe radius in Equation (28) and Equation (29) for the second rotational angular velocity of the WD when the effect of the tides and rotation on the donors structure are ignored (solid red line) or included (green, blue and dotted gray lines).

Figure 9 shows the evolution of orbital parameters due to tidal coupling for $\tau = 10$ years from Equation (28) and Equation (29). Thus, we numerically and

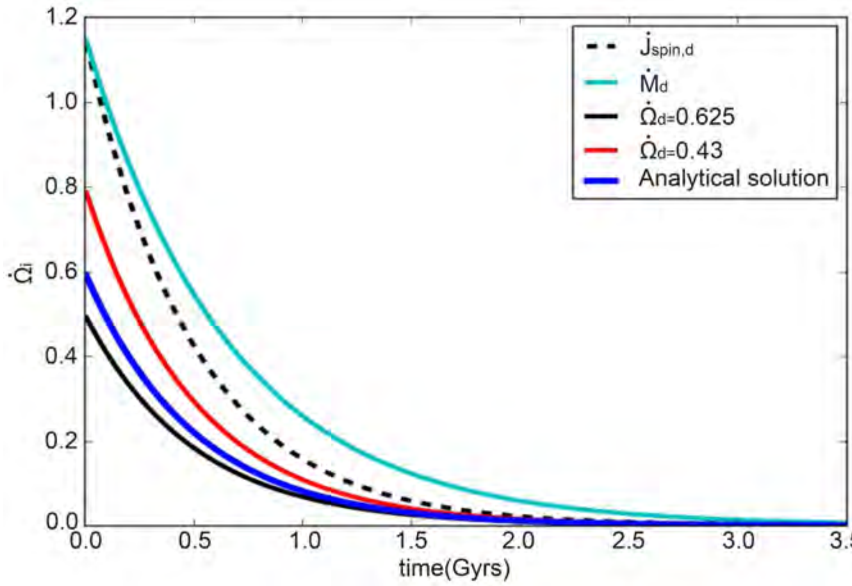

Figure 9. The comparison between the numerical and analytical solutions of orbital parameters for $\tau = 10$ years. These results obtained using the $R_{L,Egg}$ calculation of the Roche lobe. In these systems the donor decreases its mass until it finally detached from the Roche lobe and forms a $0.28M_{\odot}$ He WD and decrease the $\dot{J}_{spin,d}$.

analytically investigate the evolution of the rotational angular velocities of both donor and accretor stars in close DWD systems with initial masses of the donor, $M_d = 0.86M_{\odot}$ and accretor, $M_a = 1.2M_{\odot}$. In these systems, we provide a comparison between the numerical and analytical solution for the rate of change of the spin angular momentum for the accretor and the rate of change of the mass transfer rate corresponds to the $\dot{\Omega}_d$ and $\dot{\Omega}_a$, which shows our calculation stops when the donor reached $1.45M_{\odot}$ (disc accretion).

4.3. Comparison to Previous Results

As it was studied by [8] [9] [10] that systems with a low donor mass are more likely to remain stable over long periods of time, while the majority of the parameter space (depending on the strength of the tidal coupling) is expected to be dynamically unstable. Here, by including the additional mass transfer effects presented here in a self-consistent way, DWD direct impact mass transfer may induce a stabilizing effect over a larger area of the parameter space.

As seen in **Figures 1-5**, we discussed the evolution of angular momentum and orbital changes due to direct impact and evolution of systems with strong tidal coupling. Also, in **Figures 7-9**, we investigated the comparison between the numerical and analytical solution of the systems for the evolution of parameters for $\tau = 10$ years. However, as seen in **Figure 6**, the mass transfer rate increases initially, which causes the accretor to spin up and the donor to spin down. Hence, when we using $R_{L,Egg}$, the mass transfer rate will continue to increase until tides have transferred sufficient angular momentum from the spin of the components to the orbit to widen the orbit and decrease the mass transfer rate. Once this happens, the tides continue to redistribute angular momentum between the component spins and the orbit (see, **Figure 5**). When the system is dynamically unstable, the time scale for changes in the mass transfer rate becomes greater than the time scale at which the orbital period increases due to the effect of tides. As a result, the mass transfer rate increases rapidly and the spin of the accretor increases significantly.

5. Conclusions

We have presented the evolution of angular momentum and orbital period changes between the component spins and the orbit in close DWD binaries undergoing mass transfer through direct impact accretion, including the effects due to mass transfer, gravitational radiation, and tidal forces between the donor, accretor, and the orbit. The theoretical framework that we have outlined in this paper can be used to generate the models for the rotational angular velocities and the orbital periods of close DWD binaries in general. Thus, we implemented the ballistic mass transfer treatment developed in [19] to calculate the changes to the evolution of orbital parameters during direct impact mass transfer from the donor to the accretor, which can be described by numerical solutions. Here, the numerical solutions that we have presented are more specific than the analytical solutions of the previous studies in the sense that we allow for conservative mass transfer. By implementing this method, we found that the number of stable close DWD binaries increased for both weak and strong tidal coupling compared with the results of [9] and [10], which shown as in **Figures 1-10**.

A direct comparison of the results obtained from the numerical solutions in Section (3) with those of analytical solutions in Section (4) shows that both the numerical solution and the Eggleton approximation for the Roche lobe calculations are quite accurate.

In many cases the orbital angular momentum lost from the orbit can be significantly less than the standard assumption, making this process less destabilizing than expected. This may allow for more DWD to survive the dynamical instability of mass transfer rate and evolve into systems like AM CVn, instead of merging to create Type Ia supernovae evolving to higher separations and diminishing mass transfer rates. This result, which was not predicted by the analytical solution in [28] has important consequences for population synthesis models of these objects. Furthermore, we have seen that the near constancy of the mass transfer rate over most of the mass transfer phase seen in the results by previous studies is not a generic feature of this type of evolution but rather a consequence of a particular choice of orbital parameters.

In a few cases, we have shown that mass transfer may increase the orbital angular momentum of the orbit, thereby providing a stabilizing effect on the orbit. Hence, any stabilizing effect increases the chances of a long-lived close DWD binaries, lending acceptance to the creation of AM CVn through the DWD models.

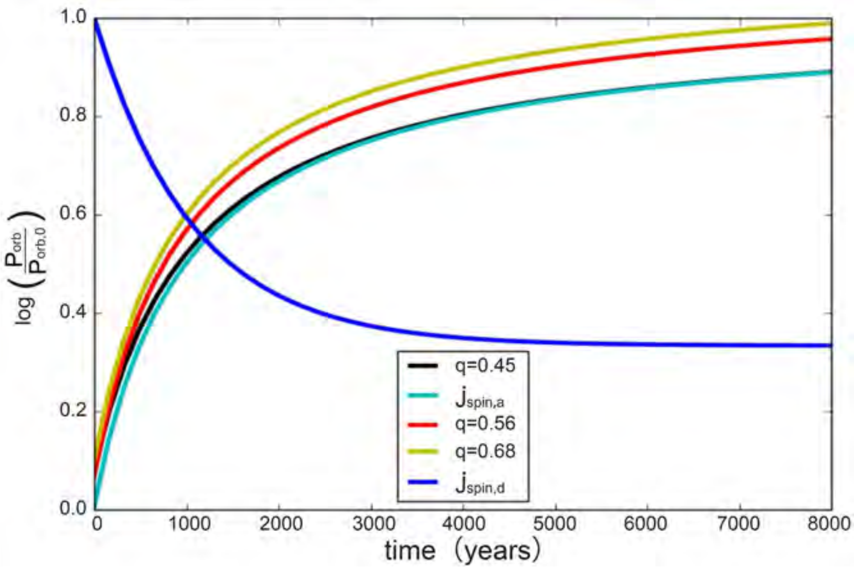

Figure 10. Evolution of the orbital period, P_{orb}, compared to its initial orbital period, $P_{orb,0}$, for three different mass ratios with synchronization time scale, $\tau = 10^{15}$. Here we observe that the P_{orb} increases due to the effect of the tides. As a result, $\dot{M}_d$ increases rapidly and the accretor spin, $\dot{J}_{spin,a}$ increases, whereas the donor spin, $\dot{J}_{spin,d}$ decreases.

We also account for the modification of the Roche lobe size due to the orbital period and ζ_{ad} of the donor stars. As a result, we found that the number of stable systems increases, particularly for the case of strong tidal coupling, as shown in Figure 1, Figure 4, Figure 5 and Figure 7. Note that all the systems that undergo direct impact systems, at least for the system orbital parameters and synchronization time scales that we have considered. Thus, when the system is dynamically unstable, the time scale for changes in the mass transfer rate becomes greater than the time scale at which the P_{orb} increases due to the effect of tides. As a result, the $\dot{M}_d$ increases rapidly the spin angular momentum of the accretor increases significantly. We conclude that the stable systems occurred when using the Eggleton approximation for the Roche lobe calculation create artificially high mass transfer rates which leads to an artificially high number of dynamically unstable systems. Hence, our finding yields a higher number of stable systems.

Finally, the large scale numerical computations presented in this paper have provided the realistic models that describing the evolution of angular momentum and orbital period changes and its stability of mass transfer in close DWD binary systems.

Acknowledgements

We thank Ethiopian Space Science and Technology Institute (ESSTI)-Entoto Observatory and Research Center (EORC), Astronomy and Astrophysics Research Development Department for giving research opportunity and facilities.

Negu S. H. thanks Jigjiga University for giving study leave. This research has made use of NASA's Astrophysical Data System.

Conflicts of Interest

The authors declare no conflicts of interest regarding the publication of this paper.

References

[1] Nelemans, G., Yungelson, L.R. and Portegies Zwart, S.F. (2001) The Gravitational Wave Signal from the Galactic Disk Population of Binaries Containing Two Compact Objects. *Astronomy & Astrophysics*, **375**, 890-898.

[2] Toonen, S., Nelemans, G. and Portegies Zwart, S. (2012) Supernova Type Ia Progenitors from Merging Double White Dwarfs. Using a New Population Synthesis Model. *Astronomy & Astrophysics*, **546**, A70.

[3] Fuller, J. and Lai, D. (2012) Dynamical Tides in Compact White Dwarf Binaries: Tidal Synchronization and Dissipation. *Monthly Notices of the Royal Astronomical Society*, **421**, 426.

[4] Burkart, J., Quataert, E., Arras, P. and Weinberg, N.N. (2013) Tidal Resonance Locks in Inspiraling White Dwarf Binaries. *Monthly Notices of the Royal Astronomical Society*, **433**, 332. https://doi.org/10.1093/mnras/stt726

[5] Tutukov, A. and Yungelson, L.R. (1996) Double-Degenerate Semidetached Binaries with Helium Secondaries: Cataclysmic Variables, Supersoft X-Ray Sources, Supernovae and Accretion-Induced Collapses. *Monthly Notices of the Royal Astronomical Society*, **280**, 1035-1045. https://doi.org/10.1093/mnras/280.4.1035

[6] Nelemans, G., Portegies Zwart, S.F., Verbunt, F. and Yungelson, L.R. (2001) Population Synthesis for Double White Dwarfs. II. Semi-Detached Systems: AM CVn Stars. *Astronomy & Astrophysics*, **368**, 939-949.

[7] Frank, J., King, A. and Raine, D. (2002) Accretion Power in Astrophysics. Cambridge University Press, Cambridge. https://doi.org/10.1017/CBO9781139164245

[8] Sepinsky, J. and Kalogera, V. (2014) Angular Momentum Exchange in White Dwarf Binaries Accreting Through Direct Impact. *The Astrophysical Journal*, **785**, 157 (8 p).

[9] Marsh, T.R., Nelemans, G. and Steeghs, D. (2004) Mass Transfer Between Double White Dwarfs. *Monthly Notices of the Royal Astronomical Society*, **350**, 113-128. https://doi.org/10.1111/j.1365-2966.2004.07564.x

[10] Gokhale, V., Peng, X.M. and Frank, J. (2007) Evolution of Close White Dwarf Binaries. *The Astrophysical Journal*, **655**, 1010-1024. https://doi.org/10.1086/510119

[11] Soberman, G.E., Phinney, E.S. and van den Heuvel, E.P.J. (1997) Stability Criteria for Mass Transfer in Binary Stellar Evolution. *Astronomy & Astrophysics*, **327**, 620-635.

[12] Negu, S.H. and Tessema, S.B. (2015) Mass Transfer in Binary Stellar Evolution and Its Stabilty. *International Journal of Astronomy and Astrophysics*, **5**, 222-241. https://doi.org/10.4236/ijaa.2015.53026

[13] Verbunt, F. and Rappaport, S. (1988) Mass Transfer Instabilities Due to Angular Momentum Flows in Close Binaries. *The Astrophysical Journal*, **332**, 193-198. https://doi.org/10.1086/166645

[14] Webbink, R.F. and Iben Jr., I. (1987) Tidal Interaction and Coalescence of Close

Binary White Dwarfs. *Proceedings of the* 2*nd Conference on Faint Blue Stars*, 445.

[15] Eggleton, P.P. (1983) Approximations to the Radii of Roche Lobes. *The Astrophysical Journal*, **268**, 368-369. https://doi.org/10.1086/160960

[16] Sepinsky, J., Willems, B. and Kalogera, V. (2007) Equipotential Surfaces and Lagrangian Points in Nonsynchronous, Eccentric Binary and Planetary Systems. *The Astrophysical Journal*, **660**, 1624-1635. https://doi.org/10.1086/513736

[17] Landau, L.D. and Lifshitz, E.M. (1975) The Classical Theory of Fields. Pergamon Press, Oxford.

[18] Campbell, C.G. (1984) Tidal Effects in Twin-Degenerate Binaries. *MNRAS*, **207**, 433-443. https://doi.org/10.1093/mnras/207.3.433

[19] Sepinsky, J., Willems, B., Kalogera, V. and Rasio, A.F. (2010) Interacting Binaries with Eccentric Orbits. III. Orbital Evolution Due to Direct Impact and Self-Accretion. *The Astrophysical Journal*, **724**, 546-558. https://doi.org/10.1088/0004-637X/724/1/546

[20] King, A.R. and Kolb, U. (1995) Consequential Angular Momentum Loss and the Period Gap of Cataclysmic Variables. *The Astrophysical Journal*, **439**, 330-336. https://doi.org/10.1086/175176

[21] Paczynski, B. and Sienkiewicz, R. (1972) Evolution of Close Binaries VIII. Mass Exchange on the Dynamical Time Scale. *Acta Astronautica*, **22**, 73-91.

[22] Webbink, R.F. (1977) The Evolution of Low Mass Close Binary Systems. III-1.50 + 0.50 Solar Masses: Unsteady Mass Loss and Shrinking Secondaries. *The Astrophysical Journal*, **211**, 486-498. https://doi.org/10.1086/154956

[23] Savonije, G.J. (1978) Roche-Lobe Overflow in X-Ray Binaries. *Astronomy & Astrophysics*, **62**, 317-338.

[24] Webbink, R.F. (1984) Double White Dwarfs as Progenitors of R Coronae Borealis Stars and Type I Supernovae. *The Astrophysical Journal*, **277**, 355-360. https://doi.org/10.1086/161701

[25] Chandrasekhar, S. (1967) An Introduction to the Study of Stellar Structure. Dover, New York.

[26] Paczynski, B. (1971) Evolutionary Processes in Close Binary Systems. *Annual Review of Astronomy and Astrophysics*, **9**, 183. https://doi.org/10.1146/annurev.aa.09.090171.001151

[27] D'Antona, F., Ventura, P., Burderi, L. and Teodorescu, A. (2006) Modeling the Closest Double Degenerate System RX J0806.3+1527 and Its Decreasing Period. *The Astrophysical Journal*, **653**, 1429. https://doi.org/10.1086/507408

[28] Hjellming, M.S. and Webbink, R.F. (1987) Thresholds for Rapid Mass Transfer in Binary Systems. *The Astrophysical Journal*, **318**, 794-808. https://doi.org/10.1086/165412

[29] Galassi, M.J.D., Theiler, J., Gough, B., Jungman, G., Booth, M. and Rossi, F. (2006) GNU Scientific Library Reference Manual. 2nd Edition, Network Theory Ltd.

[30] Lubow, S.H. and Shu, F.H. (1975) Gas Dynamics of Semidetached Binaries. *The Astrophysical Journal*, **198**, 383-405. https://doi.org/10.1086/153614

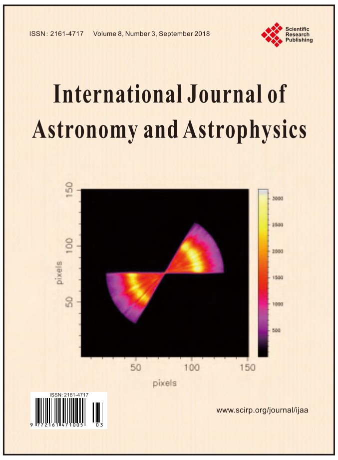

Call for Papers

International Journal of Astronomy and Astrophysics (IJAA)

ISSN 2161-4717 (Print) ISSN 2161-4725 (Online)
http://www.scirp.org/journal/ijaa

International Journal of Astronomy and Astrophysics **(IJAA)** is an international scientific journal dedicated to the publication and public discussion of high quality original research in all the fields of astrophysics and space sciences and related technology. All the manuscripts must be prepared in English, and are subject to a rigorous and fair peer-review process. Accepted papers will immediately appear online followed by printed hard copies.

Subject Coverage

The journal publishes original papers including but not limited to the following fields:

- Astrogeodynamics
- Astrophysics
- Cosmic Rays and Gamma Astronomy
- Dynamics of Celestial Bodies in the Solar System and Artificial Bodies
- Extrasolar Planets
- Formation and Evolution of Galaxies and Their Clusters
- Formation and Evolution of Stars
- Heliospheric Physics
- High-Energy and Cataclysmic Processes in Astrophysics
- Interstellar Matter
- Interstellar Medium: Star Formation Regions
- Kinematics and Structure of the Galaxy
- Large-Scale Structure of Universe Formation and Evolution of Galaxies
- Last Stages of Stellar Evolution and Chemical Evolution of the Galaxy
- Magnetospheric Physics
- Microquasars and High-Energy Astrophysics
- Neutron Astronomy
- New Astronomical Techniques and Methods
- Planets, Comets, Asteroids and Dust
- Pulsar Magnetospheres
- Solar and Stellar Physics
- Solar Magnetic Activity and Heliogeospace Environments
- Solar/Interstellar Terrestrial Relations
- Solar-Terrestrial Physics and Space Weather
- Space Observation and Exploration
- Supernovae and Evolution of the Universe

We are also interested in short papers (letters) that clearly address a specific problem, and short survey or position papers that sketch the results or problems on a specific topic. Authors of selected short papers would be invited to write a regular paper on the same topic for future issues of the IJAA.

Notes for Intending Authors

Submitted papers should not have been previously published nor be currently under consideration for publication elsewhere. Paper submission will be handled electronically through the website. All papers are refereed through a peer review process. For more details about the submissions, please access the website.

http://www.scirp.org/journal/ijaa **E-mail: ijaa@scirp.org**